# Organic-inorganic hybrids based on P3HT and mesoporous silicon for thermoelectric applications

Univ. Diss.
zur Erlangung des akademischen Grades
*doctor rerum naturalium*
(Dr. rer. nat.)
in der Wissenschaftsdisziplin ***Physik***

eingereicht von

**Natalia Gostkowska-Lekner**
Universität Potsdam & Helmholtz-Zentrum Berlin



an der
Mathematisch-Naturwisserschaftlichen Fakultät
Institut für Physik und Astronomie
der Universität Potsdam

11.12.2023

| | |
|---|---|
| Hauptbetreuer: | PD Dr. Klaus Habicht |
| Betreuer: | Prof. Dr. Patrick Huber |
| | apl. Prof. Dr. Oliver Rader |

Published online on the
Publication Server of the University of Potsdam:
https://doi.org/10.25932/publishup-62047
https://nbn-resolving.org/urn:nbn:de:kobv:517-opus4-620475

## Abstract

This thesis presents a comprehensive study on synthesis, structure and thermoelectric transport properties of organic-inorganic hybrids based on P3HT and porous silicon. The effect of embedding polymer in silicon pores on the electrical and thermal transport is studied. Morphological studies confirm successful polymer infiltration and diffusion doping with roughly 50% of the pore space occupied by conjugated polymer. Synchrotron diffraction experiments reveal no specific ordering of the polymer inside the pores. P3HT-pSi hybrids show improved electrical transport by five orders of magnitude compared to porous silicon and power factor values comparable or exceeding other P3HT-inorganic hybrids. The analysis suggests different transport mechanisms in both materials. In pSi, the transport mechanism relates to a Meyer-Neldel compansation rule. The analysis of hybrids' data using the power law in Kang-Snyder model suggests that a doped polymer mainly provides charge carriers to the pSi matrix, similar to the behavior of a doped semiconductor. Heavily suppressed thermal transport in porous silicon is treated with a modified Landauer/Lundstrom model and effective medium theories, which reveal that pSi agrees well with the Kirkpatrick model with a 68% percolation threshold. Thermal conductivities of hybrids show an increase compared to the empty pSi but the overall thermoelectric figure of merit ZT of P3HT-pSi hybrid exceeds both pSi and P3HT as well as bulk Si.

# Zusammenfassung

Diese Arbeit präsentiert eine umfassende Studie über Synthese, Struktur und thermoelektrische Transporteigenschaften von organisch-anorganischen Hybriden basierend auf P3HT und porösem Silizium. Es wird die Auswirkung der Einbettung von Polymerin Siliziumporen auf den elektrischen und thermischen Transport untersucht. Morphologische Studien bestätigen eine erfolgreiche Polymerinfiltration und Diffusionsdotierung, wobei etwa 50% des Porenraums mit konjugiertem Polymer gefüllt sind. Synchrotronexperimente zeigen keine spezifische Ordnung des Polymers innerhalb der Poren. P3HT-pSi-Hybride zeigen einen um fünf Größenordnungen verbesserten elektrischen Transport im Vergleich zu porösem Silizium und sogenannte Powerfaktoren, die mit anderen P3HT-anorganischen Hybriden vergleichbar sind oder diese übertreffen. Die Analyse lässt auf unterschiedliche Transportmechanismen in beiden Materialien schließen. In pSi bezieht sich der Transportmechanismus auf eine Meyer-Neldel-Kompensationsregel. Die Analyse der Hybriddaten unter Verwendung des Potenzgesetzes im Kang-Snyder-Modell legt nahe, dass ein dotiertes Polymer hauptsächlich Ladungsträger für die pSi-Matrix bereitstellt, ähnlich dem Verhalten eines dotierten Halbleiters. Der stark unterdrückte Wärmetransport in porösem Silizium wird mit einem modifizierten Landauer/Lundstrom-Modell und Effektivmediumtheorien behandelt, die zeigen, dass pSi mit einem Perkolationsschwellenwert von 68% gut mit dem Kirkpatrick-Modell übereinstimmt. Die Wärmeleitfähigkeiten von Hybriden zeigen einen Anstieg im Vergleich zum leeren pSi, aber der gesamte thermoelektrische Gütefaktor ZT des P3HT-pSi-Hybrids übertrifft sowohl pSi und P3HT als auch den von Bulk-Si.

# Contents

**Key Publications**

**P.1** **N. Gostkowska-Lekner**, D. Wallacher, N. Grimm, K. Habicht and T. Hofmann, "A novel electrochemical anodization cell for the synthesis of mesoporous silicon", Review of Scientific Instruments, 2022, 91, 105113

**P.2** **N. Gostkowska-Lekner**, D. Kojda, J. Hoffmann, M. May, P. Huber, K. Habicht, and T. Hofmann, "Synthesis of organic–inorganic hybrids based on the conjugated polymer P3HT and mesoporous silicon", Microporous and Mesoporous Materials, 2022, 343, 112155

**P.3** D. Kojda, T. Hofmann, **N. Gostkowska-Lekner** and K. Habicht, "Characterization and modeling of the temperature-dependent thermal conductivity in sintered porous silicon-aluminum nanomaterials", Nano Research, 022, 15, 5663–5670

# Chapter 1

# Introduction

Research presented in this doctoral thesis focuses on the application of organic-inorganic hybrids in thermoelectrics. Thermoelectric phenomena enable the conversion of heat energy into electricity and vice versa through the Seebeck [1] and Peltier [2] effects. Thermoelectric materials so far played a minor role in our energy infrastructure due to their low efficiency. But the global trends towards renewable energy and reducing the use of fossil fuels renewed the interest from scientists in these materials in order to reduce the environmental impact of energy production and minimize climate change. The European Union's long-term goal is to achieve a net-zero greenhouse gas emissions economy by 2050 [3], by moving away from nuclear and fossil fuels towards renewable energy sources. Thermoelectric materials provide a promising route to the recovery of industrial waste heat making it an attractive component in the fight against climate change. Thermoelectric materials are dominantly solid, inorganic materials that can be manipulated at the micro- and macroscopic level to improve their performance. The performance metrics are electrical conductivity $\sigma$, Seebeck coefficient $S$, thermal conductivity $\kappa$, and temperature $T$, which all define the thermoelectric figure of merit $ZT = (\sigma S^2/\kappa)T$ [4]. Efforts to improve $ZT$ include electronic doping and band structure engineering, but optimizing $\sigma$ and $S$ is not as straightforward as these values are coupled and an increase of one usually means decrease in the second one.

Manipulating the material's microstructure to influence lattice contributions to the thermal conductivity is another approach to improve $ZT$ in inorganic materials. Nanostructuring techniques affect the mean free path of the phonons by incorporating scattering centers and efficiently reducing $\kappa$, but at the same time degrading their electronic properties. A prime example of such a structure is porous silicon (pSi), which is a nanostructured but still crystalline form of silicon, one of the most important semiconductor materials. Its high porosity significantly reduces thermal conductivity, but also deteriorates the electrical transport properties.

On the other hand, an additional driving force of the recently revived interest in thermoelectrics is the emerging topic of organic semiconductors. Conductive polymers are of interest in many energy fields and have not been overlooked by thermoelectric researchers [5, 6, 7, 8]. Their attractive properties such as lightweight, flexibility and easy processability [9] attract attention in areas such as photovoltaics [10, 11] and stretchable electronics [12]. In terms of their thermoelectric performance, their adjustable electrical properties and intrinsically low thermal conductivity make them suitable for room temperature applications, a

temperature range not widely covered by conventional inorganic thermoelectrics. These properties encourage the combination of porous silicon with various organic materials to further enhance its properties in a wide range of applications. To take advantage of the inorganic scaffold structure and low thermal conductivity of pSi due to its high porosity, I propose a hybrid material based on inorganic mesoporous silicon and the organic, conductive polymer P3HT for thermoelectric applications. This thesis presents a comprehensive study of the structure and transport properties of P3HT-pSi hybrids. In general, organic-inorganic hybrids hold the promise of a material with properties that exceed those of the hybrid components.

This thesis is part of the project "Hybrid Thermoelectric Materials Based on Porous Silicon: Linking Macroscopic Transport Phenomena to Microscopic Structure and Elementary Excitations" funded by the Deutsche Forschungsgemeinschaft under the project number 402553194. The main objective of the project is to explore hybrid thermoelectric materials based on porous silicon and functionalized guest molecules. It is investigated whether it is possible to improve the intrinsically poor thermoelectric performance of silicon by porosification and embedding the conductive polymer in the pSi nanostructure.

The thesis is structured as follows. The first two chapters focus on the description of the materials and include a review of the literature on the properties and applications of porous silicon and conductive polymers. At the end of the second chapter, the concept of an organic-inorganic hybrid is introduced as the idea of combining both materials and achieving performance that ideally exceeds the average of the constituents. The following chapters discuss the thermoelectric phenomena and general transport properties in materials. Electrical and thermal transport are discussed using the Boltzmann transport equation and the Landauer approach, respectively. Chapter 4 describes in detail the characterization methods used to determine the structural and transport properties of the synthesized hybrids. In particular, methods for determining the amount of conductive polymer deposited in the pSi pore space, such as sorption isotherms and energy dispersive X-ray spectroscopy are discussed in detail. Synchrotron diffraction experiments are analyzed to investigate the polymer structure in confinement. The determination of transport coefficients is further detailed together with the band-gap determination and specific heat capacity measurements.

Chapter 5 covers the synthesis route of porous silicon by electrochemical etching in a custom-made etching cell (P.1), developed during the course of this thesis, and hybrid synthesis. Then, in Chapter 6, the structural characteristics of pSi and organic-inorganic hybrids are discussed. Finally, Chapter 7 discusses transport phenomena in porous silicon and respective hybrids. The discussion of electrical conductivity, Seebeck coefficient and thermal conductivity reveals that the thermoelectric properties of porous silicon can be improved by combining it with functionalized molecules.

# Chapter 2

# Porous silicon

Nanostructuring of silicon opens new routes to exploit the most influential semiconductor of our time. Porosification of silicon, as one of the nanostructuring techniques, dates back to 1956 when it was accidentally discovered by Ingeborg and Arthur Uhlir [13], though its full potential was recognized only 20 years later. In 1990 Canham reported visible photoluminescence from porous silicon [14, 15], which opened new routes to exploit this material and the interest in porous silicon research increased drastically. Following the increased interest in the 1980s and 1990s, porous silicon was acknowledged in both fundamental as well as applied science [16, 17, 18].
Crystalline silicon with nanometer-sized pores in the range between 1 nm and 200 nm is commonly referred to as porous silicon. Three regions can be distinguished in the classification of pSi: microporous ($< 2$ nm), mesoporous (2 nm - 50 nm) and macroporous ($> 50$ nm). Among its appealing properties are bio compatibility, tunable surface chemistry, huge pore-surface to pore-volume ratios, and controllable morphology with the source material, silicon, being an earth abundant, nontoxic, and cheap material [19, 20, 13]. It is this diversity in properties that led scientists and engineers to propose porous silicon on a technological level for micro- and nano-fluidic applications [20], novel electrodes for ion batteries [16, 21], solar cell technology [22], on-chip heat management and thermoelectric elements [23, 24], photonic and sensor applications [25, 26, 27], and to consider photoluminescence-based cancer markers [28, 29].
Porous silicon has been successfully employed in various fields with a strong focus on biomedical applications. Different forms of pSi, such as porous nanoparticles [30], porous nanowires [31], and porous thin films [32] have been used in diagnostics and advanced therapy [33]. Extensive structure and surface modifications that can be achieved in pSi unlock new possibilities such as controlling cell-pSi interfaces or therapeutic loading thanks to its high specific surface area [33]. Recently, a wireless optoelectronic system based on porous silicon-silicon heterojunctions has been presented as a promising tool to modulate peripheral nerve activity [34, 35]. Porous silicon based nanomedicine has been successfully used to deliver drugs to the inflamed synovium and degraded into bone remodeling products afterwards [36].

## 2.1 Thermoelectric applications

Next to biomedical applications, porous silicon is also considered as thermoelectric material [23, 24]. Thermoelectric materials may play a key role in the future

energy infrastructure that is environmentally friendly and sustainable. They convert thermal energy into electrical energy and vice versa by means of Seebeck [1] and Peltier [2] effects. Large scale applications are waste heat recovery and refrigeration. Small scale applications are power supplies for wearable electronics in medical diagnostics or the entertainment sector [37, 38]. All visionary applications however necessitate novel materials that excel in their performance over existing ones. The performance of thermoelectric materials is described by the dimensionless figure of merit ZT [4]

$$ZT = \frac{\sigma S^2}{\kappa} T \tag{2.1}$$

which depends on electrical conductivity $\sigma$, Seebeck coefficient $S$, thermal conductivity $\kappa$ and temperature $T$. The term $\sigma S^2$ is called power factor (PF).
Utilizing silicon for thermoelectric applications is a formidable task. Bulk silicon (bSi) has well-established synthesis and doping procedures. A highly tuned resistivity allows optimization of the power factor. Unfortunately, its high thermal conductivity [39] impairs the overall thermoelectric performance. The figure of merit is usually not higher than $ZT(bSi) = 0.01$ [40] at room temperature. Mesoporous silicon seems to provide a brilliant way to overcome this severe obstacle. Increased phonon boundary scattering [41] at the pore walls can reduce the thermal conductivity up to several orders of magnitude [42]. However, nanostructuring as well impairs the electrical properties. Charge carrier depletion at interfaces [43], increased electron (hole) boundary scattering [23], as well as the lack of percolating, conductive pathways upon high porosification [44] significantly reduce the electrical conductivity and thus limit the thermoelectric performance. Despite these obstacles, the thermoelectric performance of porous silicon is constantly improved by utilizing nanostructuring and disorder as measures to manipulate the thermal conductivity [45].
Tang et al. [46] reported that holey silicon, a silicon structure with nanoscopic holes and 35 % porosity exhibits ZT values of 0.4 at room temperature. The thermal conductivity was sufficiently reduced by two orders of magnitude due to enhanced phonon scattering on interfaces. At the same time, no strong electron scattering was observed as the electron mean free path is much smaller than the holey silicon pitch therefore a sufficient electrical conductivity was maintained. Yang et al. [47] described porous silicon nanowires with an ultra thin silicon crystallite size of about 4 nm that show a thermoelectric figure of merit of $ZT = 0.71$ at 700 K, outperforming Si with $ZT = 0.01$ - $0.04$ in the temperature range from 300 K - 700 K [39].

## 2.2 Synthesis of pSi

### 2.2.1 Chemistry

Electrochemical anodization of single-crystalline silicon wafers is a versatile approach to synthesize micro- and mesoporous silicon [18]. The control parameters for the etching process fall into three categories: properties of the source material, the electrolyte composition, and the anodization conditions. Single-crystalline silicon wafers with p-type or n-type doping, different doping levels, and different

crystallographic orientations lead to different pore morphologies [48]. Likewise, different electrolyte compositions, concentrations, and temperatures cause different porosities, pore size distributions, specific surface areas, and overall different pore networks [49]. Tuning the etching time and current density has a similar impact on the anodization result. Fig. 2.1 presents a cross-section of a mesoporous silicon synthesized by means of electrochemical anodization in hydrofluoric acid (HF) based electrolyte.

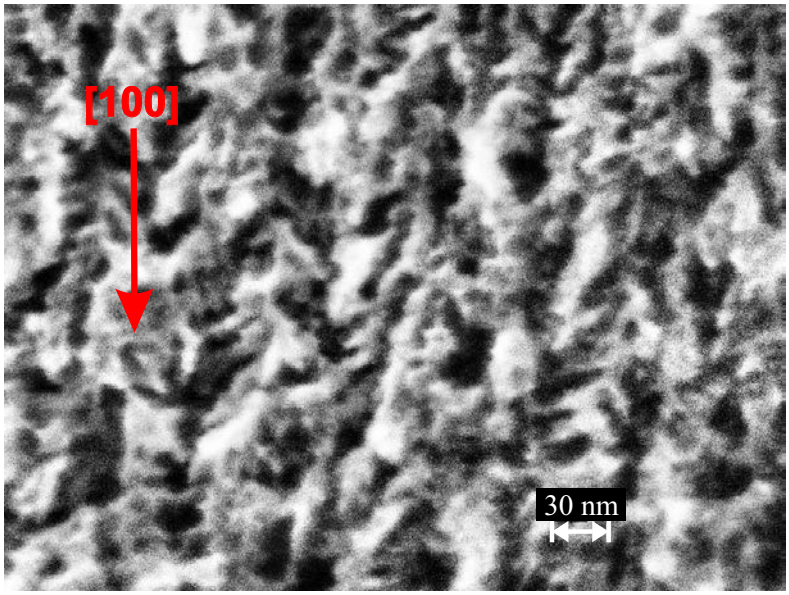


**Figure 2.1:** Cross-section of a mesoporous silicon membrane. The pore channels along the [100] crystal direction form a dendritic structure. Published in (P.2).

Electrochemical etching in HF-based electrolytes is one of the most common methods to fabricate porous silicon. The porosification starts on the wafer surface and progresses further into the silicon wafer under specific current conditions. The range of current density $j$ and applied potential $V$ in which porosification occurs depends on the composition of the electrolyte and the properties of the source silicon [50]. At higher potentials, the process turns into electropolishing, a uniform etching of the silicon without pore formation.
The porosification of silicon in an acidic electrolyte is driven by the current flow through the silicon. The basic equipment required are an electrolyte container, a platinum counter electrode and a power supply, while silicon acts as a working electrode. The silicon native oxide layer is removed once the wafer is immersed in HF, leaving silicon passivated with hydrogen atoms. The anodization process requires holes that facilitate the electrochemical dissolution process. For n-doped silicon, backside illumination might be necessary to generate electron-hole pairs and the holes to be injected into the silicon valence band. The valence band holes are oxidizing equivalents that start the process. They are driven to the Si surface by the electric field. When they reach the surface, the hydrogen passivated Si atoms become susceptible to an attack by fluorine ions $F^-$.
During the etching, the reaction that takes place at the platinum cathode is the reduction of protons to hydrogen gas:

$$2H^+ + 2e^- \rightarrow H_2 \qquad \text{(R 1)}$$

The reaction that drives the porosification is the oxidation which takes place at the silicon electrode. The two-electron oxidation process can be presented in two steps: the electrochemical step (R 2) and the chemical step (R 3):

$$Si + 2F^- + 2h^+ \rightarrow [SiF_2] \tag{R 2}$$

$$[SiF_2] + 4F^- + 2H^+ \rightarrow SiF_6^{2-} + H_2. \tag{R 3}$$

The net oxidation half-reaction is given by:

$$Si + 6F^- + 2H^+ + 2h^+ \rightarrow SiF_6^{2-} + H_2 \tag{R 4}$$

The silicon atom is removed from the crystal structure in form of a $[SiF_6]^{2-} \cdot 2H^+$ complex leaving a void in the surface. The silicon surface is hydrogen terminated and susceptible to further attack. The etching starts initially at multiple points in horizontal and vertical directions. When the pore walls start to be depleted of carriers they do not dissolve further during anodization [50] and the horizontal growth stops. This situation develops when the pore to pore distance reaches dimensions within which quantum confinement effects occur [51]. The holes tend to accumulate at the pore tips where the electric field is enhanced, leading to further pore growth. The porosification progresses within the established pores which leads to the preferential pore growth along the [100] crystallographic direction. The (100) crystal face is the least stable towards chemical attack. Quantum confinement in the pore walls leads to an increase in the band-gap in porous silicon compared to bulk Si [52].
The hydrogen gas produced during the process is generated at the cathode and partially at the anode, during the step when the holes attack Si-H bonds. The addition of ethanol in the electrolyte lowers the surface tension, facilitating the removal of $H_2$ from the pores and the system.

### 2.2.2 Etching set-up

Safety concerns are at the forefront of any synthesis attempt involving HF. In short, any contact of the experimentalist with the electrolyte must be avoided under any circumstances. Proper personal protective equipment, a safe working environment, proper safety training of the experimentalist, and a carefully designed electrochemical etching cell are as mandatory as the proper HF first aid kit in the laboratory. To assure such conditions, an etching cell was designed and built at Helmholtz-Zentrum Berlin (P.1) during the framework of this thesis. The cell design's primary objective is to guarantee safe working conditions for the experimentalist. For this purpose, it employs multi-wall containments (Fig. 2.2) for the electrolyte in combination with a peristaltic pumping system to transfer safely the electrolyte between the etching cell and the storage containers. A broad flexibility with respect to electrochemical synthesis conditions was also an important design goal. A customized control software allows us to run user-defined etch profiles. With the set-up, etching of self-supporting mesoporous membranes as thin as several tens of micrometers and mesoporous epilayers thicker than 1000 µm on silicon substrates becomes equally possible (Fig. 2.3).
The primary electrolyte container is the central part of the etching cell (Fig. 2.4). This vessel is made from Teflon to avoid any contamination of the electrolyte

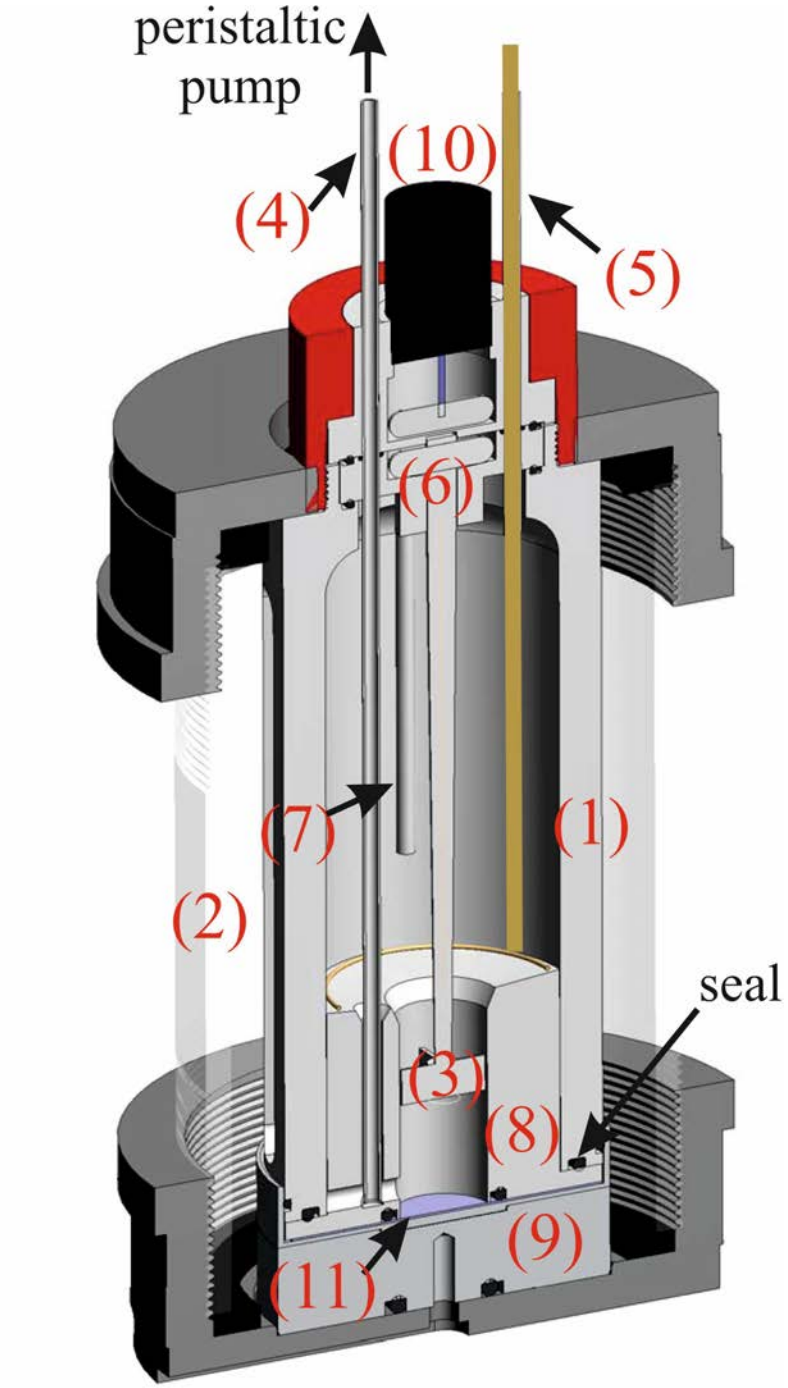


**Figure 2.2:** Anodization cell: (1) inner container, (2) outer container, (3) stirring bar, (4) Pt-tube, (5) Pt-cathode, (6) magnetic coupling, (7) exhaust, (8) high-current adapter, (9) Al-anode, (10) motor, and (11) Si wafer. Published in (P.1).

due to chemical reactions with the wall material. During cell operation, this vessel holds between 150 ml and 320 ml of the electrolyte for the synthesis of the porous silicon samples. Such a large volume of the primary container reduces the necessity of refilling and exchange of the electrolyte during the synthesis process and thus enables rather long etching times to increase sample thickness. The stirring bar is magnetically coupled to the drive motor on top of the access port.

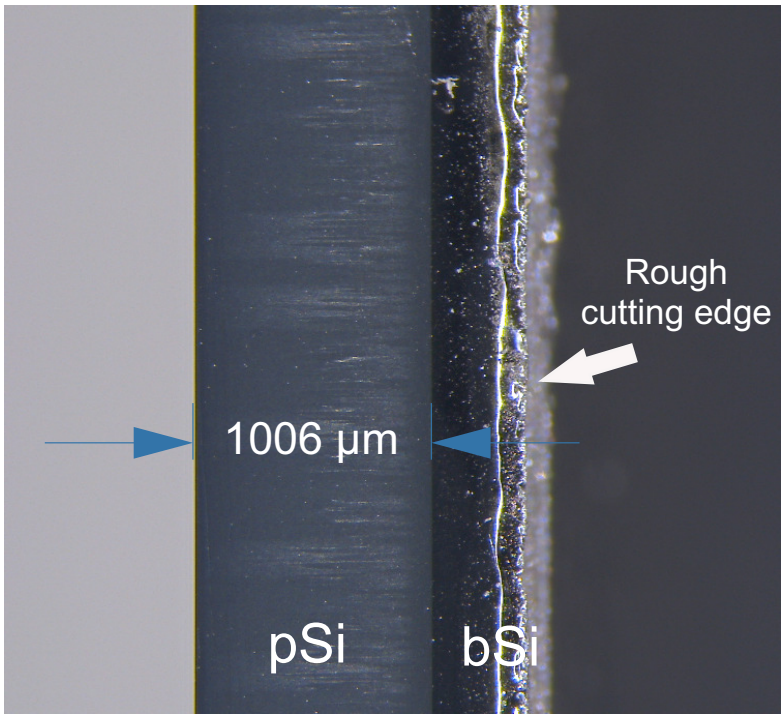


**Figure 2.3:** Optical microscopy image of a 1006 µm thick porous epilayer. The sample was etched in an 8 : 2 HF(48 %):Eth solution with a constant current density of 13 mA/cm$^2$ for 29 h. Published in (P.1).

During operation, it permanently circulates the electrolyte and guarantees a spatially homogeneous electrolyte for well-defined etching conditions. The third and last feed through is used as exhaust for gaseous hydrogen produced during the synthesis.

**Figure 2.4:** Inner container of the etching cell.

In the case of an inner leak, the secondary containment provides a buffer volume of 300 cm$^3$ to prevent a hazardous, dangerous HF spill into the environment. The entire cell design minimizes electrolyte evaporation. In particular, selective

evaporation of electrolyte components (HF and ethanol) that changes the electrolyte composition is significantly reduced minimizing variations of the process conditions. In turn, these stable long-time etching conditions allow for the synthesis of samples with huge thickness into the millimeter range. A peristaltic pump [53] connects the primary electrolyte container of the etching cell with various liquid reservoirs via elastic tubing. In order to ensure that the sample morphology is not altered by excessive contact to the electrolyte, it is important to remove the electrolyte promptly after the synthesis is completed, i.e., as soon as the electrical current is switched off.
A highly adaptable LabVIEW$^{TM}$-based software monitors and controls the anodization process. This software provides a direct interface to operate the power supply, ampere meters, and voltmeters used for anodization. It records and timestamps the current and the applied voltage bias during etching. Customized anodization sequences with time-dependent current density or etching voltage can be readily defined within the input mask of the graphical user interface (Fig. 2.5). In order to produce a freestanding membrane, the current needs to be raised for a short time right at the end of the synthesis process. The thus enlarged pore size leads to enhanced interconnection of the pores finally leading to the separation of the mesoporous membrane from the remaining bulk Si wafer.

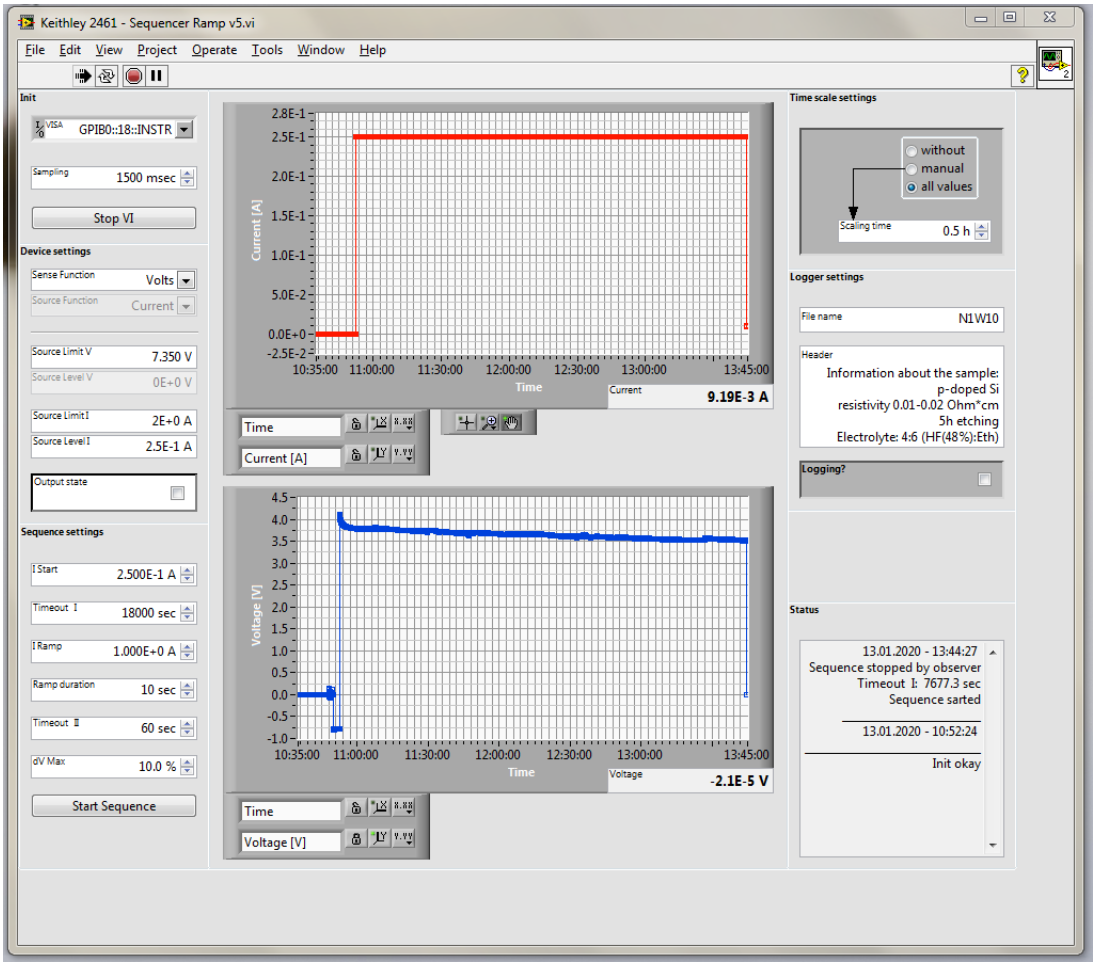


**Figure 2.5:** Interface of the control software. Published in (P.1).

In detail, the synthesis sequence for mesoporous silicon utilizing the novel cell consists of the following steps: 1. assembling of the cell, 2. connecting the electrodes to the current source, 3. defining the etching parameters in the control software, 4. electrolyte pumping from the reservoir to the primary containment, 5. initiating and finalizing the etching process by the control software, 6. pumping the electrolyte from the etching cell to a waste disposal container, 7. flushing the primary vessel multiple times with water and solvents via peristaltic pumping, 8. disassembling the cell to remove the sample, and 9. sample cleaning. The cell's primary and secondary safety containments for the electrolyte in combination with a closed peristaltic pumping system for the electrolyte transfer guarantee an improved and safe working environment for experimentalists performing Si anodization. The presented control software allows for more complicated, time-dependent etching sequences and provides a high degree of flexibility for the operator to control and adapt the etching process.

# Chapter 3

# Organic semiconductors

The first conductive organic materials reported were charge transfer complexes [54]. The first highly conductive polymers discovered were polypyrrole and polyaniline in the 1970s [55, 56]. The novel research field led to an interest in materials that had been previously considered to be insulators. The importance of the field was acknowledged in 2000 when Alan J. Heeger, Alan MacDiarmid and Hideki Shirakawa were awarded the Nobel Prize in Chemistry for their discovery and development of conductive polymers [56].

Organic semiconductors attract attention due to their tunable optical and electronic properties [57, 58]. Advantages over inorganic materials are cost effectiveness and easy processability [9]. Additionally, their mechanical flexibility and lightweight allow for novel applications like wearable electronics [12] that cannot be realized with inorganic, heavy and rigid materials.

Conjugated polymers (CPs) are organic macromolecules displaying alternating single and double bonds in their carbon backbone. Each double bond consists of a $\sigma$-bond of overlapping s-orbitals and a $\pi$-band of overlapping p-orbitals. The $\pi$-orbitals overlap along the backbone and form a filled $\pi$-band and an empty $\pi^*$-band separated by a band-gap.

This band structure results in interesting optical and electronic properties of these materials [59, 60]. Recent years saw the advent of conjugated polymers as promising functional materials for organic electronics. Organic semiconductors have received considerable attention in photovoltaics [10, 11], photocatalysis [61, 62], and optoelectronics [11, 63]. They are also recognized as novel thermoelectric materials [5, 6, 7, 8].

The energy gap between the valence and conduction bands is typically a few electronvolts. This is significantly larger than the thermal energy at room temperature (25 meV), hence the intrinsic conductivity of polymers is very low. In consequence, chemical doping is required to enhance the electrical conductivity. When an electron is removed from the valence band by e.g. oxidation in p-doping, the polymer becomes significantly more conductive. The mobile charge carriers are the charges on the polymer backbone and not the counterion formed during doping. Intrachain transport along the backbone is one of the two possible conductivity paths. In crystalline or semi-crystalline polymers, the stacking of overlapping $\pi$-orbitals creates a faster, interchain transport path [64]. Doping in organic materials is done by adding chemical molecules, which differs from its inorganic analogue where it is done by atomic substitution.

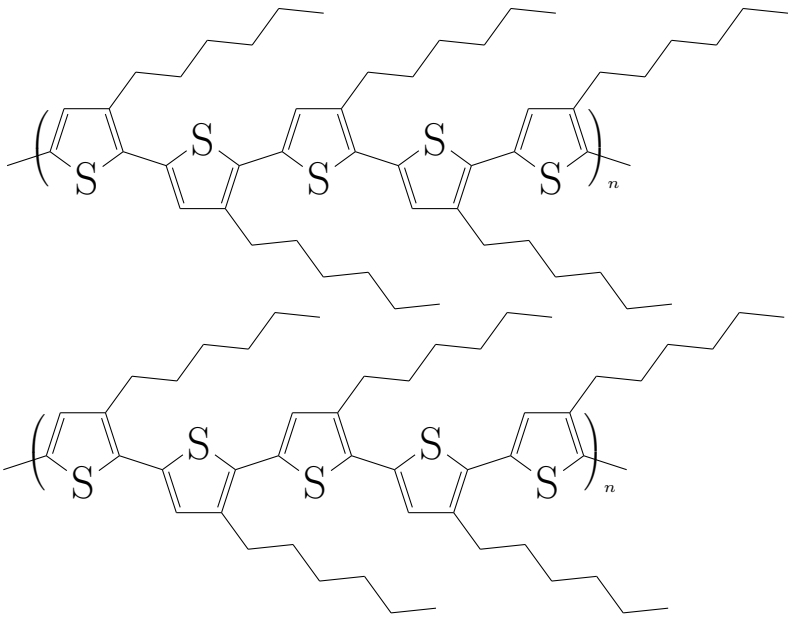

**Figure 3.1:** P3HT structure.

## 3.1 Polythiophenes

Polythiophenes are a group of conjugated polymers that are characterized by thiophene rings with a heteroatom in the aromatic ring, which is sulfur bonded to $sp^2$ hybridized carbons. The thiophene rings are coupled in the 2 and 5 position which allows the $\pi$-orbital conjugation to occur along the polymer chain [59]. They are intrinsically conductive, but their neutral state is characterized by a large band-gap leading to conductivities of about $10^{-8}\,\Omega^{-1}\,\mathrm{cm}^{-1}$ [65]. Polythiophene can be changed to a more conductive form by oxidation and creating polarons and bipolarons in the backbone [66]. Polythiophene and its derivatives have been extensively studied both theoretically and experimentally [67]. Their morphology has a drastic impact on the band-gap, therefore altering the geometry has a significant effect on the electronic and optical properties [68].

## 3.2 P3HT structure

Poly(3-hexylothiophene) (P3HT) is a hole-transporting (p-type) conductive polymer widely known in the organic electronics field with well-established synthesis and doping routes [69]. It exhibits an exceptionally high charge carrier mobility [70], which can be enhanced by a factor of 20 upon chain alignment inside straight nanopores [71].
P3HT is a semicrystalline polymer with the backbone that is $\pi$-conjugated and alkyl side chains [72]. The organized chain microstructure of the polymer is described as regioregularity, the situation where each repeating unit derives from the same isomer of the monomer. Regioregularity in P3HT can take three forms (dyads), head-tail (HT), head-head (HH) and tail-tail (TT). In a head-tail dyad the side chains are separated by three carbon atoms. It creates a stable repeating unit and is the favorable configuration. It is the HT configuration that can un-

dergo self-assembly, which provides a highly oriented polymer structure referred to as semicrystalline [73]. P3HT is a stiff polymer with flexible side chains, which already present a layered structure in the melt phase. The phase separation between stiff backbone and flexible side chains is preserved upon crystallization and the crystal lattice is formed [74]. In regioregular P3HT, the lattice parameters at room temperature are $a$ =1.64 nm, $b$ =0.76 nm and $c$ =0.77 nm [74].
The polymer chains can adopt different stacking configurations towards the substrate, namely edge-on and face-on. In the edge-on configuration, the lamellar side chains stack perpendicular to the substrate, while in the face-on configuration, it is the aromatic ring $\pi$-$\pi$ stacking that faces the substrate. These orientations depend on the substrate itself, the processing method, percent of regioregularity and molecular weight [72].

### 3.2.1 P3HT processability and doping

P3HT favours solution- and melt-based processing routes thanks to its good solubility in chloroform, 2-chlorotoluene and toluene [75] and its low melting temperature of $T = 510\,\mathrm{K}$ [76]. Unfortunately, as many conductive polymers, P3HT displays low stability due to easy oxidation under light illumination in air [77]. To avoid any air exposure, handling of the polymer during processing should be carried out in an inert atmosphere.
Electrical and optical properties of conjugated polymers depend highly on film morphology, doping mechanism and efficiency, which is the ratio of free carriers to dopant content. Typically, when a film is prepared from a solution with a premixed polymer and dopant, a non-homogeneous film formation can be witnessed [78], which is not observed with only the pure polymer. The sequential procedure, where doping is performed on the initially prepared polymer results in better film quality and crystallinity [78, 79]. The sequential incorporation of dopants into the polymer structure occurs by means of diffusion. Dopant size and electron affinity have also been shown to have an impact on the electrical conductivity of conjugated polymers [79].
Various chemical compounds are used as doping agents for polythiophenes. The most popular ones are the ferric salt of a triflimide anion ($TFSI^-$), (2, 3, 5, 6)-tetrafluoro-(7, 7, 8, 8)-tetracyanoquinodimethane ($F4TCNQ$), (7, 7, 8, 8)- tetracyanoquinodimethane ($TCNQ$), (1, 3, 5)-trichloro-benzene (TCB), molybdenum tris(dithiolene) complex ($Mo(tfd)_3$) and ferric chloride ($FeCl_3$) [79, 7, 5]. The doping procedures include immersion, vapor and electrochemical methods as well as spin-coating techniques [7, 5]. The dopants listed above present a range of different molecules that not only vary significantly in size and incorporation method but also with respect to their doping mechanisms.
Two mechanisms can be distinguished in the doping of organic semiconductors: an integer charge transfer (ICT) and a formation of the ground state charge-transfer complex (CTX) [79]. In the first case, the entire charge is transferred and localized on the molecule. This leads to the coexistence of charged and uncharged molecules [80] and ion pair formation. The ICT molecular doping can be compared to the model in inorganic chemistry as it occurs when the polymer's ionization energy is very close to the electronic affinity of the dopant [81]. In the CTX, the molecular orbitals of the organic molecule hybridize with the dopant molecule. They form a set of bonding and antibonding supramolecular

orbitals [82], which result in delocalized electronic states [83]. Different doping mechanisms have been observed for organic-dopant systems with the same conductive polymer base. For example, P3HT with $F4TCNQ$ forms an ICT system [82, 84], whereas it creates a CTX complex with $TCNQ$ and $FeCl_3$ [84, 85].

## 3.3 Electrical transport in P3HT

Conductive polymers attract attention in the thermoelectric field due to their excellent mechanical properties, flexibility and exceptional processability, advantages that are not common in inorganic, brittle materials [5, 6, 7, 8]. P3HT, next to PEDOT, is one of the most interesting organic thermoelectric material candidates. Its advantage over PEDOT is that it is highly dispersible in many organic solvents, extending its processing options. Various possible doping routes for P3HT broaden its application spectrum. The electrical conductivity and Seebeck coefficient of P3HT are two of the properties that vary strongly with not only the doping concentration but also the doping type.

In semi-crystalline polymers, charges move differently depending on the length scale and arrangement of the structure. The most efficient charge transport takes place when the polymer structure is in a crystalline form. The charge carrier can easily move along the polymer backbone, but only on a short, single chain length scale (intrachain transport). Further along the polymer chain, interchain hopping occurs, which dominates transport in ordered regions. At length scales where an active layer is usually used (e.g. in transistors $>$ µm), the presence of only a highly ordered phase is difficult to achieve [86], and the polymer layer consists of both ordered and amorphous regions.

The ordered regions consist of crystallites and aggregates, in which only the $\pi$ stacking occurs without any ordering towards the alkyl side [64]. In the amorphous phase even the $\pi$ stacking is disrupted. Efficient transport along the backbone only occurs on the scale of a few nanometers and the charge transfer in the organic layer is limited by transport through the amorphous phase. Therefore, it is important to ensure the optimal amount of interconnection between ordered phases in order to maintain efficient transport. In addition to the morphology of the polymer, the type of dopant, its size, concentration, method of doping and even the doping mechanism has a great influence on the final electrical properties of organic semiconductors.

The exact mechanism of charge transport in conjugated polymers is still not entirely understood. In general, polarons and bipolarons are responsible for charge transport in CPs and it is believed that polarons transfer charge at low doping concentration and bipolarons at higher concentrations. The polaron in this context is a quasiparticle which results from the interaction between charge carriers and local vibrations [87]. The charge is localized on the local deformation that can be either conformational or electrical [87]. To move, the charge carrier must hop to the adjacent neighbor site. This type of conduction is called hopping [87, 64].

Many different theories have been proposed to explain the conduction mechanism among which Mott's variable-range hopping was the most successful in various polymers. Variable-range hopping occurs when charge carriers are not strongly localized and hop into the position where the distance and activation energy are

optimal. Variable-range hopping was observed to govern electrical transport in $FeCl_3$-doped P3HT [85, 88].

Researchers are trying to find the best way to improve transport properties for their envisioned application. Values for electrical conductivity and Seebeck coefficient in doped P3HT change strongly from study to study. Singh et al. [85] discuss the conductivities of $FeCl_3$-doped P3HT films in terms of varying doping concentrations. The highest values of electrical conductivity $2.7 \times 10^{-3}\,\Omega^{-1}\,\mathrm{cm}^{-1}$ were obtained for the highest dopant concentration. In addition to electrical data, they provide information on the formation of charge carrier complexes upon doping with $FeCl_3$. Gregory et al. [89] prepared wire-bar coated P3HT films doped by drop casting of $FeCl_3$-acetonitrile solution. They have achieved conductivities from $0.1\,\Omega^{-1}\,\mathrm{cm}^{-1}$ to $100\,\Omega^{-1}\,\mathrm{cm}^{-1}$ and Seebeck coefficients from $140\,\mu\mathrm{V\,K}^{-1}$ to $30\,\mu\mathrm{V\,K}^{-1}$ with varying dopant solution concentration from 0.38 mM to 50 mM.

More attention is paid to the polymers morphology as its importance has been recognized over time. Hong et al. [90] showed that by controlling the thickness and morphology of the polymer layer, the thermoelectric properties are significantly improved. Through wire-bar coating processing and doping by immersion in a $FeCl_3$ solution, $\sigma$ values of $250\,\Omega^{-1}\,\mathrm{cm}^{-1}$ were obtained. It is ten times higher than for the drop casting method while maintaining the Seebeck coefficient of about $37\,\mu\mathrm{V\,K}^{-1}$. The electrical conductivity obtained in this study was the highest for the thickest prepared layer (4 µm). Wu et al. [91] observed that using a polymer with a higher molecular weight could improve the ordering and cause more densely packed P3HT polymer chains. With $FeCl_3$ as a dopant, they achieved the electrical conductivity of $\sigma = 250\,\Omega^{-1}\,\mathrm{cm}^{-1}$ and a Seebeck coefficient of about $S = 40\,\mu\mathrm{V\,K}^{-1}$ leading to a power factor of $PF = 20\,\mu\mathrm{W\,m}^{-1}\,\mathrm{K}^{-2}$.

High electrical conductivities were also obtained for other dopants. Zhang et al. [92] doped the P3HT films with $TFSI^-$ and reported a power factor exceeding $20\,\mu\mathrm{W\,m}^{-1}\,\mathrm{K}^{-2}$ at conductivity of $90\,\Omega^{-1}\,\mathrm{cm}^{-1}$. Lim et al. [93] used $F4TCNQ$ and achieved an electrical conductivity of $48\,\Omega^{-1}\,\mathrm{cm}^{-1}$ for a vapour doped sample and reached PF values of $27\,\mu\mathrm{W\,m}^{-1}\,\mathrm{K}^{-2}$. In this case, the dopant infiltration also changed the polymer film morphology. Untilova et al. [94] obtained values as high as $\sigma = 160\,\Omega^{-1}\,\mathrm{cm}^{-1}$, $S = 60\,\mu\mathrm{V\,K}^{-1}$ and a PF of about $20\,\mu\mathrm{W\,m}^{-1}\,\mathrm{K}^{-2}$ for highly oriented P3HT films doped with molybdenum dithiolene complex. The dopant level of highly oriented films was observed to be significantly higher than of the poorly aligned film despite following the same procedure of immersion doping. Qu et al. [95] obtained the highest power factor of $62\,\mu\mathrm{W\,m}^{-1}\,\mathrm{K}^{-2}$ at $T = 365\,\mathrm{K}$ ($\sigma = 200\,\Omega^{-1}\,\mathrm{cm}^{-1}$, $S = 55\,\mu\mathrm{V\,K}^{-1}$) owing it to a highly anisotropic P3HT film doped with TCB.

As shown above, varying dopant chemicals, preparation and doping methods result in a range of electrical conductivities and Seebeck coefficients which highly influence the thermoelectric performance.

## 3.4 Organic-inorganic hybrids

Further improvement, in addition to altering polymer properties, can be achieved by combining organic semiconductors with inorganic materials. In recent years, carbon nanotubes (CNT) sparked massive interest as an inorganic contribution to the composites. The enormous interest it generated a few years ago has led

many researchers to combine CNTs with their materials of interest to take advantage of CNTs' unique properties. Single- and multi-walled carbon nanotubes were also used to create composites with P3HT. In the work of Bounioux et al. this combination resulted in an exceptionally high PF of $95\,\mu W\,m^{-1}\,K^{-2}$ [96]. Hong et al. also prepared single-walled CNT/P3HT hybrid films, where CNTs formed an interconnected network, drastically improving electrical conductivity, resulting in PFs as high as $267\,\mu W\,m^{-1}\,K^{-2}$ [97] and $325\,\mu W\,m^{-1}\,K^{-2}$ [98].
Significantly enhanced thermoelectric properties were observed in other semiconducting polymers when mixed with different inorganic materials. Choi et al. designed a ternary hybrid of graphene / polymer / inorganic nanocrystal and observed double-carrier filtering at the two heterojunctions [99]. Wang et al. found an exceptionally high power factor of $PF = 1350\,\mu W\,m^{-1}\,K^{-2}$ in (PEDOT)/$Bi_2Te_3$ hybrid films [100]. Those enhanced properties result not only from mixing both materials, but from combined properties that are not simple compound averages. Such envisioned materials, organic-inorganic hybrids, form a bridge between conventional inorganic electronics and all-polymer based devices. In other fields of functional materials, Gélvez-Rueda and Sofos illustrate the potential of hybrids for solar-energy harvesting [101, 102]. Gélvez-Rueda [101] improved charge carrier separation in inorganic perovskite layers by incorporation of functional organic chromophores, whereas Sofos [102] synthesized alternating lamellar ZnO-conjugated molecule hybrids with improved photoconductive performance.
On a more fundamental level, porous silicon emerged in recent decades as a versatile host material to study the effect of nanoconfinement on the structural and dynamical properties of condensed matter [17, 103]. Functionalized molecules or polymers embedded in rigid, inorganic nanostructures are role models for nanoconfined soft matter. Their physical properties have to be carefully compared with the ones of their macroscopic bulk counterparts as spatial confinement affects their physical properties [17, 103] and consequently the hybrids themselves. To provide a few examples, confinement is responsible for a more effective electropolymerization of polyaniline inside silica pores than on bare ITO [104], for modified chain orientations in pore-confined MEH-PPV polymers, which lead to novel optical properties [105], and for nano-confinement induced chain alignment in poly(3-hexylothiophene) P3HT during thermal nanoimprinting [106], which is of obvious relevance for the inter-chain electronic conductance [107].
In the light of the presented potential of organic-inorganic hybrids, a system based on mesoporous silicon and P3HT was designed. Different strategies to incorporate organic molecules into the porous host matrix have been proposed. In case of solution filling techniques, big challenges are achieving homogeneous pore fillings as the removal of the solvent may cause redistribution of the active phase [108] and reaching a high degree of pore fillings for polymers with large radius of gyration, respectively with low solubility. The crucial parameter regulating the filling is the radius of gyration of the polymer [109]. If the radius of gyration is greater than the pore diameter, clogging of the pores may occur and the filling will remain insufficient. P3HT can be melt-processed which is of a great advantage to uniformly fill the inorganic host matrix. Melt infiltration is conceptually the simplest approach. The viscous flow of the polymer melt into the pore channel is triggered by capillary forces. It depends mainly on the pore

radius, surface tension, contact angle and viscosity. High degrees of pore filling can be achieved in a single step [108, 110, 111].
Experiments regarding P3HT incorporation into nanoporous membranes have been previously reported [71, 106, 112]. However, the incorporation depth usually is in the range of hundreds of nanometers and does not exceed 20 µm and the polymer occupies not more than 30 % [112] of the pore volume. In this work, 200 µm thick porous silicon membranes are used. Taking into account nanometer-sized pore channels of pSi, the melt-based polymer infiltration approach is selected as the organic molecule incorporation method. $FeCl_3$ is chosen as the P3HT dopant. Its easy diffusion into the polymer matrix and small molecule size make it the best fit to use in the confined polymer - pSi system. A high degree of pore filling ($> 50$ %) and successful dopant diffusion into the polymer structure were achieved for the P3HT-pSi system. This work presents a comprehensive study of its structural and thermoelectric transport properties.

# Chapter 4

# Transport properties

## 4.1 Thermoelectric phenomena

Thermoelectric effects provide a direct way to convert heat into electricity or vice versa via the Seebeck effect or the Peltier effect. The coupled transport of heat and electricity that governs thermoelectricity leads to interesting phenomena that could play a key role in a future energy infrastructure based on "green" technology, environmental friendly and sustainable power sources. The conversion of thermal energy into electrical energy is a great promise to recover waste heat that is constantly produced and in most cases lost or hardly usable. Thermoelectric generators are reliable, active sources of electric power that can utilize thermal energy in sectors like electronic devices, vehicles or buildings. They have no moving parts, operate in silence and could be integrated in many bulk devices that have long operating lifetimes [113].
The efficiency of thermoelectric devices needs considerable improvement. However, they can already be used in environments where no other power source could be used, e.g. rockets and satellites. For example, radioisotope thermoelectric generators are the central power source in the mission module of Voyager [114], a space probe launched to study the outer solar system. The thermal energy required to operate the generators is gained from radioisotopes.
While many operating materials are efficient at elevated temperatures, there is still a lack of well-performing materials that cover near-room temperature applications. Modules operating at this temperature range would be suitable for powering, e.g., wearable electronics from human body heat.
Thermoelectric effects comprise various separate effects [4] from which three are discussed below: the Seebeck effect [1], the Peltier effect [2] and the Thomson effect [4].

### 4.1.1 Seebeck effect

The Seebeck effect was discovered in 1821 by Thomas Johann Seebeck during experiments with bismuth and copper wires [1]. Seebeck had constructed a closed loop of two conductors and held the junctions at different temperatures. He then observed a magnetic field, which was induced by the current flow through the loop. Its strength increased with increasing temperature difference between the two junctions.
The effect can be explained with a schematic thermocouple (Fig. 4.1), a circuit formed from two different conductors (a and b) that are connected electrically

in series but thermally in parallel [4]. If the junctions are held at different $T$, an open circuit voltage is developed between points C and D. The ratio between the voltage induced in material a, to the temperature difference across material a is called the absolute Seebeck coefficient:

$$S_A = \frac{V_S}{\Delta T} \tag{4.1}$$

The net Seebeck coefficient is the difference between the absolute Seebeck coefficients of the circuit materials, $S_A - S_B$. The voltage between open ends is called thermoelectric voltage $V_S$

$$S_A - S_B = \frac{V_S}{T_H - T_C} \tag{4.2}$$

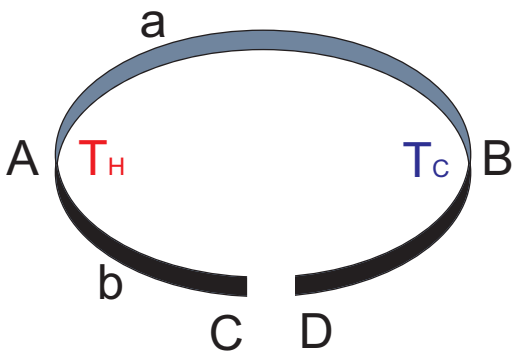


**Figure 4.1:** Schematic thermocouple made of two materials. Thermoeelctric voltage $V_S$ is produced when a temperature difference $\Delta T$ is generated between the junctions A and B.

On the more fundamental level, "the absolute Seebeck coefficient of a material is the entropy transported with a charge carrier in isothermal flow divided by the carrier's charge" [115]. The entropy dragged along by the flow of charge inside the material has two parts: the change in entropy associated with adding a charge carrier and the transfer of energy linked with a carrier movement in the material divided by the temperature.
As we will discuss in chapter 4.2, the electrical current, that is the particle current times the charge $eJ_N$, is caused by the electrochemical potential gradient $\nabla\mu$ and the temperature gradient $\nabla T$

$$J = eJ_N = -(\sigma/e)\nabla\mu - \sigma S\nabla T. \tag{4.3}$$

With Eq. 4.3 it becomes evident that in an open circuit ($J_N = 0$) a temperature gradient causes the gradient in the electrochemical potential. The general formula for a Seebeck coefficient writes as

$$S_A \equiv -\frac{1}{e}\frac{\nabla\mu}{\nabla T}. \tag{4.4}$$

With small gradients, the ratio of gradients equals the ratio of the differentials and the definition resembles the one from Eq. 4.1.

The Seebeck coefficient is a material property. The relationship between the temperature difference and the generated voltage is linear for small $\Delta T$. Knowing $\Delta T$ and measuring $V_S$ one can determine the relative Seebeck coefficient of materials. This is the basis of Seebeck coefficient determination. The probing material is typically platinum with absolute $S_{Pt}$ taken as $0\,\mu V\,K^{-1}$ therefore $S_B$ of an investigated material can be easily determined. The Seebeck coefficient is measured in Volts per Kelvin and the sign indicates what type of charge carrier is predominant in a material.

### 4.1.2 Peltier effect

When an electrical current is injected into the loop, heat is transported between the junctions depending on the direction of the current. During the current flow, heat is absorbed at one junction and released at the other. This effect is the basis of the thermoelectric cooling devices and was discovered by Jean Peltier in 1834 [2].
Peltier heat is the heat that is generated or absorbed at the junction. When a charge goes through the junction in isothermal conditions, in order to maintain it, the heat must be supplied to the junction under electron thermalization which usually happens via inelastic collisions with other electrons or phonons [115, 116]. The Peltier coefficient ($\Pi$) is the difference between heat flow associated with carriers leaving the junction ($J_{QA}$) and that associated with carriers entering the junction ($J_{QB}$), divided by the electric current that passes through that junction. $\Pi$ is a material-specific constant, and can be related to the Seebeck coefficient of the two junction materials with:

$$\Pi_{AB} = \frac{J_{QB} - J_{QA}}{eJ_N} = T(S_B - S_A). \tag{4.5}$$

The Peltier coefficient is the product of the junction's temperature and the difference between the Seebeck coefficient of the two materials. The relation between Seebeck and Peltier coefficient is called the second Kelvin relation [115].

### 4.1.3 Thomson effect

William Thompson, later known as Lord Kelvin, discovered a third thermoelectric effect in which Thomson heat $Q_T$ is exchanged with the environment when an electric current flows through a homogeneous wire with temperature gradient. The Thomson heat divided by the electrical current and thermal gradient is defined as Thomson coefficient [4, 115],

$$\tau \equiv \frac{Q_T}{eJ_N \nabla T}. \tag{4.6}$$

The Thomson coefficient is linked with the Seebeck coefficient by the first Kelvin relation:

$$\tau = T\frac{dS}{dT}. \tag{4.7}$$

The relationship between the Thomson and Seebeck coefficient of a material can be deduced from the energy balance upon steady-state flow through the circuit [115].

## 4.2 Generalized forces

The fundamental equation in classical equilibrium thermodynamics [117] in terms of entropy $S(U, V, N)$ is

$$dS = \frac{1}{T}dU + \frac{p}{T}dV - \frac{\mu}{T}dN. \tag{4.8}$$

U is the internal energy, V is the volume of the system, N is the particle number, T is the temperature, p is the pressure and $\mu$ is the chemical potential. At fixed volume $dV = 0$, the change in entropy density ($\tilde{\sigma} = S/V$) can be related to density of the particles $n$ and to the energy density $u$

$$d\tilde{\sigma} = \frac{1}{T}du - \frac{\mu}{T}dn. \tag{4.9}$$

This total differential defines the entropic conjugate variable of energy density and particle density as

$$\frac{\partial\tilde{\sigma}}{\partial u} = \frac{1}{T} \quad \text{and} \quad \frac{\partial\tilde{\sigma}}{\partial n} = -\frac{\mu}{T}. \tag{4.10}$$

These variables are the "potentials" for energy and particles, respectively. Their spatial gradients are entropic forces that drive energy and particle currents to increase the entropy in non-equilibrium situations [117]:

$$\nabla\left(\frac{1}{T}\right) \quad \text{and} \quad \nabla\left(-\frac{\mu}{T}\right) \quad . \tag{4.11}$$

Transport phenomena in general describe the flux of particles like electrons or phonons in a medium due to driving forces, such as electric fields, temperature or particle concentration gradients [116]. The link between the fluxes and driving forces can be described with a linear approximation in which one writes energy and particle currents as:

$$J_u = \tilde{L}_{11}\nabla\left(\frac{1}{T}\right) + \tilde{L}_{12}\nabla\left(-\frac{\mu}{T}\right) \tag{4.12}$$

$$J_N = \tilde{L}_{21}\nabla\left(\frac{1}{T}\right) + \tilde{L}_{22}\nabla\left(-\frac{\mu}{T}\right). \tag{4.13}$$

In 1931, Lars Onsager [118] showed that the coupling coefficients $\tilde{L}_{ij}$ form a symmetrical matrix meaning that for $B = 0$, off-diagonal terms are symmetric and $\tilde{L}_{12} = \tilde{L}_{21}$.
In the spirit of the first law of thermodynamics and the conservation of energy, the heat current can be written as:

$$J_Q = J_u - \mu J_N. \tag{4.14}$$

Using the chain rule one gets

$$\nabla\left(\frac{\mu}{T}\right) = \mu\nabla\left(\frac{1}{T}\right) + \frac{1}{T}\left(\nabla\mu\right) \tag{4.15}$$

and particle current and heat current become

$$J_N = L_{11}\left(-\frac{1}{T}\nabla\mu\right) + L_{12}\nabla\left(\frac{1}{T}\right) \tag{4.16}$$

$$J_Q = L_{21}\left(-\frac{1}{T}\nabla\mu\right) + L_{22}\nabla\left(\frac{1}{T}\right), \tag{4.17}$$

where $L_{12} = L_{21}$. $L_{ij}$ are called the kinetic coefficients with $L_{11} = \tilde{L}_{11}$, $L_{12} = \tilde{L}_{12} - \mu\tilde{L}_{11}$, $L_{22} = \tilde{L}_{22} - \mu(\tilde{L}_{21} + \tilde{L}_{12}) + \mu^2\tilde{L}_{11}$.
On the basis of the kinetic coefficients, electrical and thermal conductivity as well as Seebeck and Peltier coefficients can be determined.

### 4.2.1 Electrical conductivity

To determine the electrical conductivity $\sigma$ we assume the absence of a temperature gradient $\nabla T = 0$. The current can be described as the particle current times the electrical charge $e$

$$J = e \cdot J_N = eL_{11}\left(-\frac{1}{T}\nabla\mu\right). \tag{4.18}$$

With $E = -\frac{\nabla\mu}{e}$ it is

$$J = e^2 L_{11}\left(\frac{1}{T}\right) \cdot E = \sigma E \tag{4.19}$$

and the electrical conductivity in terms of kinetic coefficients can be defined as

$$\sigma = e^2\frac{L_{11}}{T}. \tag{4.20}$$

### 4.2.2 Thermal conductivity

Thermal conductivity in an open circuit can be obtained from Eq. 4.16 and Eq. 4.17. Without particle current flow, $J_N = 0$, it is

$$-\frac{L_{11}}{T}\nabla\mu + L_{12}\nabla\left(\frac{1}{T}\right) = 0 \tag{4.21}$$

and the heat flux density becomes

$$J_Q = -\frac{1}{T^2}\frac{L_{21}L_{12} - L_{11}L_{22}}{L_{11}}\nabla T. \tag{4.22}$$

The thermal conductivity is defined as

$$\kappa = \frac{1}{T^2}\frac{L_{11}L_{22} - L_{12}L_{21}}{L_{11}}. \tag{4.23}$$

The closed circuit thermal conductivity ($\nabla\mu = 0$) is

$$J_Q = -\underbrace{\frac{L_{22}}{T^2}}_{\kappa_E}\nabla T. \tag{4.24}$$

### 4.2.3 Seebeck coefficient

The Seebeck coefficient is measured in an open circuit, in the absence of any particle current, as in Eq. 4.21. If we consider the Seebeck coefficient as the ratio of the electrochemical potential gradient and the temperature gradient we can write

$$-\frac{1}{e}\nabla\mu \equiv S\nabla T. \tag{4.25}$$

When $T$ and $\mu$ gradients are small when measuring the materials' $S$, the ratio of the gradients $\Delta\mu/\Delta T$ is equal to the ratio of the differentials $\nabla\mu/\nabla T$. After substituting the $\nabla\mu$ to $e\Delta V$ in Eq. 4.21 and with (4.4) and Eq. 4.1 one gets

$$\Delta V = -\frac{1}{eT}\frac{L_{12}}{L_{11}}\Delta T \tag{4.26}$$

and the Seebeck coefficient becomes

$$S = -\frac{\Delta V}{\Delta T} = \frac{1}{eT}\frac{L_{12}}{L_{11}}. \tag{4.27}$$

### 4.2.4 Peltier coefficient

To describe the Peltier coefficient in terms of kinetic coefficients, one assumes an isothermal situation $\nabla\left(\frac{1}{T}\right) = 0$. The electrical current and the heat current become

$$J = eL_{11}\left(-\frac{1}{T}\nabla\mu\right) \quad \text{and} \quad J_Q = L_{21}\left(-\frac{1}{T}\nabla\mu\right). \tag{4.28}$$

The Peltier coefficient is the coupling term between current density and heat flux

$$J_Q = \underbrace{\frac{1}{e}\frac{L_{12}}{L_{11}}}_{\Pi} J \tag{4.29}$$

and the relation between the Peltier and the Seebeck coefficient is $\Pi = ST$.

## 4.3 Boltzmann transport

Electric field and temperature gradients are the driving forces leading to electron transport in solids. The movement of electrons is disturbed by their scattering on phonons and defects. The Boltzmann equation describes the interplay between these two mechanisms by describing the changes of the electron distribution function under the influence of external forces and as a result of electron collisions. The distribution of electrons at equilibrium, in $k$- and energy-space and without external fields is given by the Fermi-Dirac distribution [119]

$$f_0(E(k)) = \frac{1}{e^{[E(k)-\mu]/k_B T} + 1}. \tag{4.30}$$

Here, $E(k)$ is the energy, $\mu$ is the chemical potential, $k_B$ is the Boltzmann constant and $T$ is the temperature.
Outside of equilibrium, the required distribution can be space ($r$) and time ($t$) dependent and is affected by external fields and collisions.
To derive the distribution function $f(\vec{r}, \vec{k}, t)$ the change during the time from $t - dt$ to $t$ is considered. Under external fields and in the absence of collisions, the change over this time is $\vec{r} - \vec{v}(\vec{k})dt$ in the position of the electron and $\vec{k} + e\vec{E}dt/\hbar$ in the wavevector. The change due to scattering is described by the term $\left(\frac{\partial f}{\partial t}\right)_s$ which gives us [120]

$$f(\vec{r}, \vec{k}, t) = f(\vec{r} - \vec{v}(\vec{k})dt, \vec{k} + e\vec{E}dt/\hbar, t - dt) + \left(\frac{\partial f}{\partial t}\right)_s dt. \tag{4.31}$$

Expanding this equation to terms linear in $dt$ one gets:

$$\frac{\partial f}{\partial t} + \vec{v} \cdot \vec{\nabla}_{\vec{r}} f - \frac{e}{\hbar}\vec{E} \cdot \vec{\nabla}_{\vec{k}} f = \left(\frac{\partial f}{\partial t}\right)_s \tag{4.32}$$

which is the Boltzmann equation representing one starting point for approaching the transport problems in solids. It is often modeled in the so-called relaxation time approximation, which assumes that $f$ returns to the equilibrium $f_0$ due to scattering at a rate proportional to the deviation of $f$ from $f_0$

$$\left(\frac{\partial f}{\partial t}\right)_s = -\frac{f(\vec{k}) - f_0(\vec{k})}{\tau(\vec{k})}, \tag{4.33}$$

where the $\tau(\vec{k})$ is a relaxation time, which depends on the wavevector $\vec{k}$. If a stationary non-equilibrium distribution ($f_{stat}(\vec{k})$) is settled and the external field is then switched off, one can write $\frac{\partial f}{\partial t} = -\frac{f - f_0}{\tau}$. When the initial conditions $f(\vec{k}, t = 0) = f_{stat}(\vec{k})$ are fulfilled, the Boltzmann equation has the solution [120]:

$$f(\vec{k}) - f_0(\vec{k}) = (f_{stat}(\vec{k}, t = 0) - f_0(\vec{k}))e^{-t/\tau(\vec{k})}. \tag{4.34}$$

The relaxation time is therefore the time constant with which the non-equilibrium distribution relaxes to the equilibrium state via scattering after the external field is switched off.
In the presence of time-independent driving forces, the distribution function starts to change. At the beginning, when $f$ is close to $f_0$, the change is dominated

by driving forces (external fields) and as the $f - f_0$ increases, the importance of scattering increases. The distribution function becomes

$$f = f_0(\vec{k}) + \left(\frac{\partial f_0}{\partial E}\right) \tau(\vec{k})\vec{v}(\vec{k}) \left( e\vec{E} - \vec{\nabla}_{\vec{r}}\mu - \frac{(E(\vec{k}) - \mu)}{T}\vec{\nabla}_{\vec{r}}T \right), \tag{4.35}$$

a so-called linearized Boltzmann equation for the determination of the non-equilibrium distribution. For phenomena in which only a linear dependence on fields is expected (e.g. ohmic conduction), calculations can be restricted to the linear part of the Taylor expansion for $f(\vec{k})$ [120, 116].
A stationary non-equilibrium distribution that does not depend on the position $r$ can be represented by a distribution function where $f_0$ is shifted by $e\tau\vec{E}/\hbar$ from the equilibrium position [120] as an expansion around point $\vec{k}$

$$f(\vec{k}) = f_0\left(\vec{k} + \frac{e}{\hbar}\tau(\vec{k})\vec{E}\right). \tag{4.36}$$

Only electrons near the Fermi surface contribute to the electrical transport ($\frac{\partial f_0}{\partial E} \neq 0$). The stationary state of the Fermi distribution can be represented as a displacement of the Fermi sphere. When the external field causing the displacement vanishes, the sphere relaxes back to its equilibrium. When electrons scatter from occupied to unoccupied states, which are at different distances from the $\vec{k}$-space origin, the relaxation must involve inelastic scattering mechanisms (e.g, phonon scattering). The relaxation is caused by inelastic scattering only [120].
The Boltzmann transport equation can be used to derive transport coefficients of solids, described also in Section 4.2.

### 4.3.1 Drude model

Around 1900, Drude described metallic conductivity with the classical equation of motion, assuming an ideal electron gas [120]

$$m\frac{d\vec{v}}{dt} + \frac{m}{\tau}\vec{v_D} = -e\vec{E}, \tag{4.37}$$

where the scattering is accounted for by the friction term $m\vec{v_D}/\tau$. The $\tau$ term here also has the meaning of a relaxation time. In the stationary case, where $\frac{d\vec{v}}{dt} = 0$, the drift velocity $\vec{v_D}$ becomes

$$\vec{v_D} = -\frac{e\tau}{m}\vec{E} \ = -\mu\vec{E}. \tag{4.38}$$

The term $\mu = e\tau/m$ is the carrier mobility and hence the current density can be presented as [119, 120]

$$j = -env_D = ne\mu\vec{E} = \frac{e^2\tau n}{m}\vec{E}, \tag{4.39}$$

where $n$ is the volume density of free electrons and $\mu$ is the mobility. The electrical conductivity in the Drude model can be presented as

$$\sigma = \frac{e^2 n\tau}{m}. \tag{4.40}$$

In this simple model, all electrons contribute to the current.

For semiconductors one must consider both electrons in the lower conduction band and holes in the upper valence band. The current density of an isotropic semiconductor is then [119]

$$j = e(n\mu_n + p\mu_p)\vec{E}, \tag{4.41}$$

where $\mu_n$ and $\mu_p$ are the electron and hole mobilities, respectively, and $n$ and $p$ are the respective carrier densities. These mean values can be expressed as [119]

$$\mu_n = \frac{1}{m_n^*} \frac{\langle \tau(\vec{k}) v^2(\vec{k}) \rangle}{\langle v^2(\vec{k}) \rangle} e. \tag{4.42}$$

The $m_n^*$ here is the effective electron mass, $v(\vec{k})$ is the electron velocity and $\tau(\vec{k})$ is the scattering time in the state $\vec{k}$. From the temperature dependence of the carrier mobility, one can infer the dominant scattering mechanism that occurs in the material. Charge scattering due to acoustic phonons results in the proportionality $\mu_{ph} \sim T^{-3/2}$, while scattering due to charged impurities $\mu_{def} \sim T^{3/2}$ [119].

## 4.4 Thermal transport

Thermal energy in solids can be transported via electrons and various excitations such as phonons and magnons. While in metals the majority of heat is transported by electrons, in insulators and semiconductors phonons carry most of the heat, while electrons are responsible for part of the heat conduction [120]. We define the thermal conductivity $\kappa$ of a solid as the constant of proportionality between the driving temperature gradient and the resulting heat flux density $J_Q$ according to Fourier's law [119]

$$\vec{J_Q} = -\kappa \vec{\nabla} T, \tag{4.43}$$

where the heat flows from the hot end to the cold end of the sample.
The heat current density in terms of the phonon properties is defined as [119]

$$J_Q = \Sigma_{q,r} \hbar\omega_{q,r} \langle n_{q,r} \rangle v_x(q,r) = 0, \tag{4.44}$$

where $\hbar\omega_{q,r}$ denotes the phonon energy with wavevector $q$ and polarization $r$. $\langle n_{q,r} \rangle$ is the phonon density and $v_x$ the phonon group velocity $\partial\omega/\partial q$ in the $x$-direction.
In thermal equilibrium, $J_Q$ is zero as the $\langle n \rangle$ are the same for positive and negative $q$-values. The symmetry of the phonon dispersion results in $v_x(q) = -v_x(-q)$ and the sum in Eq. 4.44 vanishes [119, 120]. Heat flow exists when a temperature gradient is applied along the material so that the mean phonon density deviates from equilibrium $n^0$. There are two contributions to the change in phonon density per unit time $dn/dt$. The first part is due to diffusion $dn/dt = -\frac{\partial n}{\partial T}\frac{\partial T}{\partial x} v_x$ and the second due to scattering, which with the relaxation time approximation is $dn/dt = -\delta n/\tau$.
With a steady-state thermal current, the sum of these contributions vanishes and $\delta n$ becomes equal to $-\tau v_x \frac{\partial n^0}{\partial T}\frac{\partial T}{\partial x}$. Here we use $\langle n \rangle^0$ instead of $\langle n \rangle$ as an approximation. When substituted into Eq. 4.44, one derives the heat current density in the non-equilibrium state [119]

$$J_Q = -\Sigma_{q,r} \hbar\omega_{q,r} \tau v_x^2(q,r) \frac{\partial n^0}{\partial T}\frac{\partial T}{\partial x}. \tag{4.45}$$

The factor in front of the temperature gradient represents the thermal conductivity $\kappa$. One can write for isotropic systems the phonon velocity as $v_x^2 = 1/3 v^2$. Using the expression for specific heat, $c_v = \Sigma_{q,r} \hbar\omega_{q,r} \frac{\partial}{\partial T} \langle n_{q,r} \rangle^0$, one can further express the thermal conductivity as

$$\kappa = \frac{1}{3} c_v v l \tag{4.46}$$

with the introduced mean free path $l = v\tau$ and the assumptions of constant $\tau(q)$ and $v_x(q)$.
Heat current due to electrons can be represented by the analogous equation [120]

$$J_Q = -\Sigma_{q,r} (E_q - \mu) \tau v_x^2(q) \frac{\partial f^0}{\partial T}\frac{\partial T}{\partial x} = J_E - \mu J_N. \tag{4.47}$$

Here, $E$ is the energy of the electron, $\mu$ is the electrochemical potential and $\frac{\partial f^0}{\partial T}$ is the change in electron distribution due to a temperature change.

## 4.5 Landauer/Lundstrom approach

In semiconductors, most of the heat is carried by phonons. The Landauer formula for phonon current is given by [121]

$$J_Q = \frac{1}{h}\int_0^\infty T_{ph} M_{ph} \hbar\omega (n_1 - n_2) d(\hbar\omega), \tag{4.48}$$

where $h$ is the Planck constant, $T_{ph}$ is the transmission at given phonon energy $\hbar\omega$, $M_{ph}$ is the number of conducting channels at a given energy and $n_1$ and $n_2$ are Bose-Einstein distributions

$$n_0(\hbar\omega) = \frac{1}{e^{\hbar\omega/kT} - 1} \tag{4.49}$$

for the two contacts across which the heat flows. In the phonon current, the energy $\hbar\omega$ moves across the channel (analogous to the charge being transported in electron current) transferring heat. The transmission function $T_{ph}$ describes the phonon transmission across the channel and is given by [121]

$$T_{ph} = \frac{\lambda_{ph}(\omega)}{L + \lambda_{ph}(\omega)} \tag{4.50}$$

with $\lambda_{ph}(\omega)$ as a mean free path and L for the length of a conductor. For a small temperature gradient the thermal conductance ($K_{ph} = J_Q/\nabla T$) becomes

$$K_{ph} = \frac{k_B^2 T_L \pi^2}{3h}\int_0^\infty T_{ph} M_{ph} W_{ph} d(\hbar\omega), \tag{4.51}$$

where $k_B^2 T_L \pi^2/3h$ is the quantum of thermal conductance with $T_L$ being the lattice temperature and $W_{ph}$ a window function that specifies which modes carry the heat current [121, 122]

$$W_{ph} = \frac{3}{\pi^2}\left(\frac{\hbar\omega}{k_B T_L}\right)^2 \left(-\frac{\partial n^0}{\partial(\hbar\omega)}\right). \tag{4.52}$$

The integral of the window function from 0 to $\infty$ is 1, similar to the derivative of the Fermi function ($-\partial f^0/\partial E$) for the electrical conductivity for electrons. The final thermal conductivity can be presented as

$$\kappa_{ph} = \frac{k_B^2 T_L \pi}{6}\int_0^\infty \frac{4}{3}\Lambda(\omega) M_{ph}(\omega) W_{ph}(\omega) d(\omega). \tag{4.53}$$

The mean free path for three-dimensional structures is averaged and comes with a 4/3 prefactor for the spectral mean free path $\Lambda(\omega)$ [121, 122].

### 4.5.1 Modified Landauer/Lundstrom model for $\kappa$

Recently, a modified Landauer/Lundstrom model has been proposed to describe thermal conductivity in sintered porous silicon - aluminum nanomaterials (P.3). It was developed to elucidate the impact of porosity and nanostructure on the heat transport, as the material optimization, for e.g. thermoelectrics, requires a deep understanding of the transport mechanisms. The model decouples the

effects of porosity and the domain size by introducing the relative thermal conductivity $\kappa_r$

$$\kappa_{eff} = \kappa_r \kappa_0 = \kappa_r \frac{k_B^2 T_L \pi}{6} \int_0^\infty \frac{4}{3} \Lambda(\omega) M_{ph}(\omega) W_{ph}(\omega) d(\omega). \tag{4.54}$$

The factor $\kappa_0$ is the intrinsic thermal conductivity of the dense material and depends on the domain (crystallite) size, while $\kappa_r$, the relative thermal conductivity, is a function of porosity ($0 \leq \kappa_r \leq 1$). This formulation allows to decouple the thermal conductivity decrease caused by porosity and to analyze it separately from nanostructuring effects (P.3).
In Eq. (4.54) the free parameters to be fitted to the data are the relative thermal conductivity $\kappa_r$ and the phonon mean free path $\Lambda$. The phonon mean free path is determined by the material's individual scattering mechanisms. The scattering times corresponding to these mechanisms are added by means of Matthiessen's rule

$$\tau = \left(\tau_{imp}^{-1} + \tau_{boundary}^{-1} + \tau_{umklapp}^{-1} + \tau_D^{-1}\right). \tag{4.55}$$

They correspond to impurity scattering, boundary scattering, Umklapp scattering and additional scattering by nanostructured domains. $\Lambda_D = v_g(\omega)\tau_D$, where $v_g(\omega)$ is the phonon group velocity, represents the phonon mean path that combines scattering at domains and pores (P.3).

# Chapter 5

# Characterization methods

This chapter discusses the methods used to characterize the structural and transport properties of mesoporous silicon and P3HT-pSi hybrids. Experimental results on structural characterization are described in Chapter 7 and on electrical and thermal transport in Chapter 8.

## 5.1 Sorption isotherms

Analysis of sorption isotherms is a versatile method for characterizing porous materials with respect to porosity, pore size distribution and specific surface area [123]. Isotherms probe the volumetric uptake of liquid nitrogen $f(P/P_0) = N/N_0$ inside the pore space at $T = 77\,\mathrm{K}$ as the reduced pressure $P_{red} = P/P_0$ of the coexisting gas phase is stepwise changed. Here, $N$ is the number of nitrogen molecules physisorbed and $N_0$ is the number of molecules required to fill the pore volume completely. $P$ and $P_0$ refer to the equilibrium pressure of the confined liquid and the saturation pressure of the bulk liquid.
The International Union of Pure and Applied Chemistry (IUPAC) classifies pores according to their size [123]. Pores with width below 2 nm are called micropores. Pores of widths in the range from 2 nm - 50 nm are called mesopores. Pores with width exceeding 50 nm are called macropores and have less significance in the context of nitrogen physisorption [123]. In this work, we utilize mesoporous silicon.
A schematic drawing of the device used for the measurement is shown in Fig. 5.1. The main parts of the nitrogen sorption isotherm set-up are a small sample container, a gas reservoir, a liquid Nitrogen tank, various valves and a pump. The parts are isolated with valves. The sample container is kept at 77 K during the measurement, while the gas reservoir is kept at room temperature. This set-up allows for a procedure in which $P_{red}$ is stepwise increased. The volume of the sample container $V_S$ should be smaller than the gas reservoir $V$ ($V_s << V$).
The very first step is measuring the sample mass and outgassing the sample container along with the specimen in it at an elevated temperature. This step allows the removal of previously adsorbed molecules in the sample, such as water. Once the sample is attached to the set-up, it is pumped again so that there is no air in the container or pore space. A typical adsorption step starts with a constant pressure $P_1$ in $V$ and $V_s$ with both valves 1 and 2 closed. The number of nitrogen molecules in the gas phase is given by

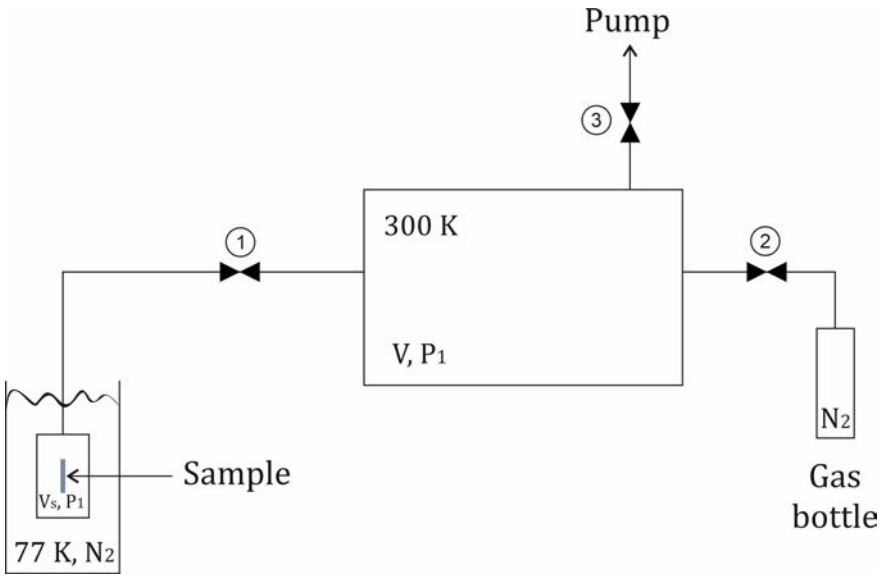


**Figure 5.1:** Schematic set up of sorption isotherm measurement (Quantachrome autosorb iQ).

$$N_1 = \frac{P_1 V}{k_B 300K} + \frac{P_1 V_s}{k_B 77K}. \tag{5.1}$$

Now the second valve opens to establish a new pressure $\tilde{P}$ in the gas reservoir and closes afterwards. The number of nitrogen molecules in the gas phase changes to

$$\tilde{N} = \frac{\tilde{P} V}{k_B 300K} + \frac{P_1 V_s}{k_B 77K}. \tag{5.2}$$

Subsequently, the 1st valve opens and enables gas to enter the sample container. As soon as the pressure equalizes to $P_2$, the valve is closed. The number of $N_2$ molecules in the gas phase is now

$$N_2 = \frac{P_2 V}{k_B 300K} + \frac{P_2 V_s}{k_B 77K}. \tag{5.3}$$

The number of molecules absorbed in a sorption step is given by

$$\Delta N = \tilde{N} - N_2. \tag{5.4}$$

The procedure is continued step by step until the pressure of the coexisting gas phase reaches the saturation pressure $P_0$. A desorption step is conducted accordingly using valve 3 instead of 2 to remove gas molecules stepwise from the system.

Fig. 5.2 shows a typical sorption isotherm of mesoporous silicon, which shows how the amount of absorbed $N_2$ molecules in the pores changes with pressure. This process can be divided into three stages. In region A (up to $P_{red} \leq 0.65$), a multilayer is absorbed on the pore walls. Analysis of this region with the Brunauer-Emmett-Teller (BET) method [124] gives information on the effective surface area of the porous specimen. In regime B (hysteresis, $P_{red} \geq 0.65$), the onset of pore condensation begins as the reduced pressure increases, until the entire pore space is filled with liquid nitrogen (region C).

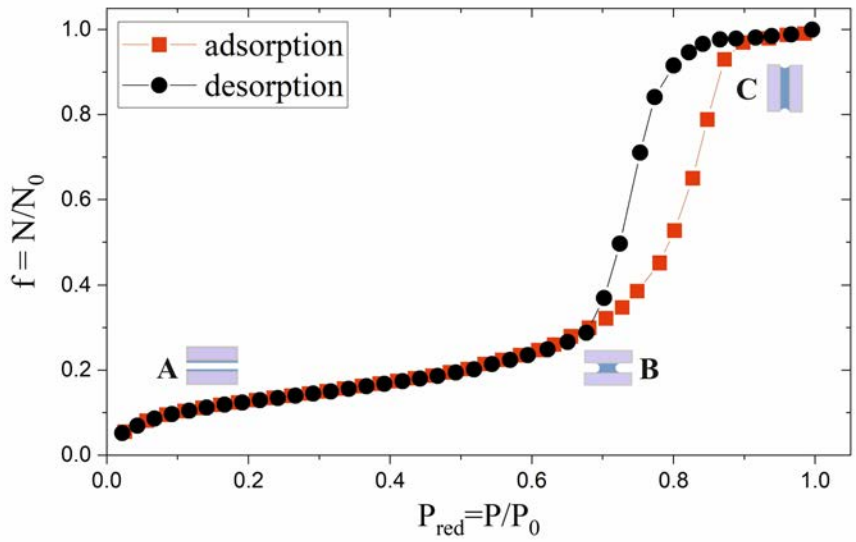


**Figure 5.2:** $N_2$ sorption isotherm of as-etched pSi at $T = 77\,\mathrm{K}$.

The isotherm usually follows a hysteresis path upon adsorption and desorption. It depends on the material's pore size and structure [125, 123]. One can name several reasons for the hysteresis. In a single cylindrical pore, one expects a delayed onset of capillary condensation due to the metastable liquid film on the pore wall, while in desorption the capillary condensate coexists in thermodynamic equilibrium with the wall film [125, 123]. This configuration nucleates from the liquid meniscus at the pore "mouth" (see C in Fig. 5.2).
In a pore network, one expects pore blocking in desorption, as smaller pores might delay the desorption from connected larger pores. The larger pore remains filled until the narrow pore is emptied at a lower saturation pressure. As the consequence, the wider pore does not desorb at its pressure "window" causing the change in hysteresis [126]. Pore blocking usually shows steep, nearly vertical desorption branches at higher fillings. Because the pSi sorption isotherm does not show pore blocking, the desorption branch is used for further analysis.

### 5.1.1 Kelvin equation

Let us consider a liquid-vapor interface with constant mean curvature H, such as a spherical drop, meniscus or cylindrical film. The pressure difference across the interface is given by the Young-Laplace equation [127]

$$\Delta P = \gamma H \tag{5.5}$$

with $\gamma$ as the surface tension.
Moreover, the vapor pressure is changed compared to the bulk according to the Kelvin equation [128]

$$ln\left(\frac{P}{P_0}\right) = -\frac{\Delta P\, V_m}{RT} \tag{5.6}$$

which can be derived from the Gibbs-Duhem equation [129] or by hydrostatic

theory [130].
In the equation, $P$ is the pressure of the coexisting gas phase, $P_0$ is the saturated vapor pressure, $V_m$ is the molar volume of the liquid. This equation is the basis of pore-size analysis as described in Sec. 5.1.4.

### 5.1.2 Specific surface determination

The specific surface area of mesoporous materials can be obtained by employing the BET theory [124]. The application of this method involves the use of the BET equation, which describes the isotherm for multilayer growth on a flat substrate

$$\frac{1}{W((P_0/P)-1)} = \frac{1}{W_m + C} + \frac{C-1}{W_m C}\left(\frac{P}{P_0}\right), \tag{5.7}$$

where W is the mass of absorbed gas, $P/P_0$ is the relative pressure and $W_m$ is the mass of absorbed gas forming the monolayer on the mesoporous surface. $C$ is the BET constant, related to the energy of adsorption in the first adsorbed layer. Eq. 5.7 in our case is restricted to the x-range of 0.05 - 0.35 (with nitrogen as adsorbate), where a linear plot of $1/(W(P_0/P)-1))$ versus relative pressure $P/P_0$ can be extracted. The mass $W_m$ can be obtained from the slope $s$ and the intercept $i$, and the total surface area of the sample is

$$S_t = \frac{W_m N A_{cs}}{M}, \tag{5.8}$$

where $N_A$ is the Avogadro's number, M is the molar mass of nitrogen and $A_{cs}$ is cross-sectional area of nitrogen (16.2 Å at $T = 77\,\mathrm{K}$) [125]. The specific surface area is finally calculated with the sample mass $w$

$$S = \frac{S_t}{w}. \tag{5.9}$$

### 5.1.3 Pore volume

The total pore volume is derived from the amount of absorbed vapour close to the saturation pressure, around $P_{red} = 0.99$, with the assumption that all pores are filled with liquid nitrogen. The volume of liquid nitrogen in the pores $V_{liquid}$ can be obtained from the volume of adsorbed nitrogen gas $V_{ads}$ with

$$V_{liquid} = \frac{P_a V_{ads} V_m}{RT}, \tag{5.10}$$

where the $P_a$ and T are the ambient pressure and the temperature, and $V_m$ is the molar volume of liquid adsorbate [125].

### 5.1.4 Mesopore size analysis

Barret, Joyner and Halenda [131] developed a method for analyzing the pore size in a sample using the desorption branch at relative pressures $P_{red}$ that are above the onset of capillary condensation. It uses the Kelvin relation, which relates $P_{red}$ to the pore radius $r_p$ using the molar volume of the liquid $V_m$ and the surface tension $\gamma$. The method takes into account the thickness of the preadsorbed multilayer film $t_c$ and thus the Kelvin equation for cylindrical pores is

$$ln\,(P_{red}) = -\frac{2\gamma V_m}{RT(r_p - t_c)}. \tag{5.11}$$

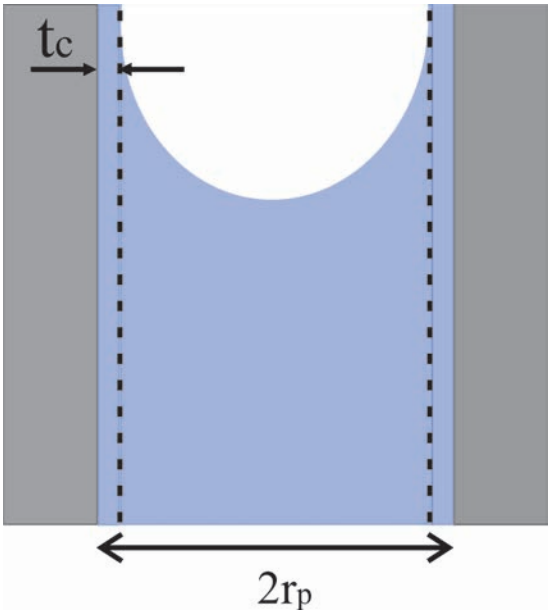


**Figure 5.3:** A scheme for capillary condensation inside cylindrical pore.

The equation assumes a tubular pore and a hemispherical meniscus inside the pore as shown in Fig. 5.3. Despite many concerns with the analysis of narrow mesopores [123], it is still the most popular technique to extract the pore size distribution from sorption isotherms. The generally accepted assumptions are that the preadsorbed layer is evenly distributed over a planar surface and the pores are of cylindrical shape. The pore size distribution is the distribution of the pore volume with respect to $r_p$, $(dV/dr_p)$. The distribution resulting from the model is normalized with respect to the mass and has units of $cm^3/nm/g$.

## 5.2 X-rays and UV-Vis

The discovery of X-rays by W.C. Röntgen in 1895 [132] began a new era in science, especially in physics and medicine. The importance of this discovery was recognized shortly thereafter and awarded the first Nobel Prize in Physics in 1901. Since then, X-rays have been employed to solve a variety of problems, from the medical diagnostics to probing the structure of materials and even proteins. X-rays are electromagnetic waves with wavelengths in the Ångström region, comparable to inter-atomic distances [119]. This size scale makes them one of the most important tools to study the structures at the atomic level. Storage rings, also known as synchrotrons, are state-of-the-art X-ray sources particularly suited for the study of inorganic and organic matter in basic research, in particular in physics, biology, chemistry, medicine and pharmacology.
In a storage ring with diameters up to 2.2 km [133], electrons or positrons move on average in a circular orbit. Locally, the beam trajectory is altered with wigglers and undulators to trigger the acceleration induced X-ray emission. For example, at the PETRA III storage ring in Hamburg, photon energies between 150 eV and 200 keV can be produced [134]. These energies are able to probe the structure and properties of inorganic and organic matter at the atomic level.

### 5.2.1 Scattering from periodic structures

With X-rays as a probe, scattering occurs on the electrons of the sample under investigation. Characteristic distances between electrons are inducing scattering signals at different angles, and therefore detecting those intensities provides structural information on a distinct length scale. Bragg's law describes the constructive interference of scattered waves from a periodic crystal lattice, where the waves reflect from lattice planes [119, 120]

$$n\lambda = 2dsin(\theta). \tag{5.12}$$

Here $n$ is the diffraction order, an integer, $d$ is the spacing between the lattice planes, $2\theta$ is the scattering angle and $\lambda$ is the wavelength of an incident, monochromatic beam. It is a condition for constructive interference of waves. The scattering vector $\vec{K}$ is the difference between incident $\vec{k}$ and scattered $\vec{k'}$ X-rays

$$\vec{K} = \vec{k} - \vec{k'}. \tag{5.13}$$

In a crystal, scattering occurs only if $\vec{G} = \vec{K}$, where $\vec{G}$ is a reciprocal lattice vector [120]. This condition, where the difference between the incident and scattered waves $\vec{k} - \vec{k'}$ is equal to the reciprocal lattice vector, is called the Laue condition [120]. Because we only consider elastic scattering, $|\vec{k}| = |\vec{k'}|$, the condition $\vec{G} = \vec{K}$ can be used as a selection rule for the scattering vector change. This selection rule can be graphically represented with the help of the Ewald sphere. From an arbitrary chosen point of the reciprocal lattice, set as the coordinate origin, we draw an incident wavevector $\vec{k}$ and draw a sphere around the starting point with the length of $2\pi/\lambda$. The difference $\vec{G}$ is the scattering vector and since $\vec{k'}$ has the same length as the incident one, $\vec{G}$ lies on the constructed

sphere, which is called the Ewald sphere (Fig. 5.4). Diffraction occurs whenever a reciprocal lattice point lies exactly on the Ewald sphere. The reciprocal lattice vector modulus for elastic scattering can be presented as

$$G = |\vec{G}| = \frac{4\pi}{\lambda} sin(\theta) \tag{5.14}$$

During X-ray diffraction experiments with fixed wavelength $\lambda$, the reciprocal lattice vectors are found at specific scattering angles $2\theta$ and the distances between lattice planes can be analyzed based on these $2\theta$ values.

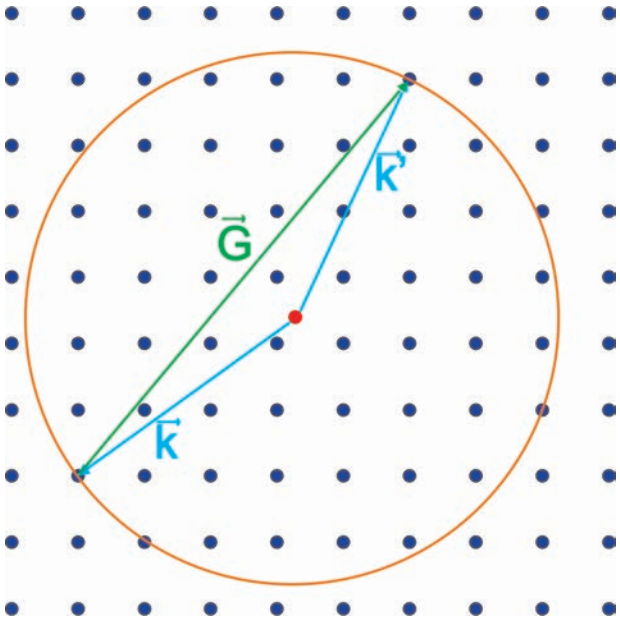


**Figure 5.4:** The construction of the Ewald sphere.

### 5.2.2 Synchrotron scattering experiments

Scattering experiments were performed to probe the structure and ordering of P3HT polymer inside the mesoporous silicon pore channels. The orientation of the polymer backbones and thiophene rings, that comes along with overlapping $\pi$-orbitals, define strongly the charge transport in the polymer. Highly conductive pathways coincide with the stacking of thiophene rings, therefore this orientation is of particular interest. To investigate the potential P3HT texture inside the pSi pores, Small Angle X-ray Scattering (SAXS) techniques were employed. Temperature-dependent scans were performed at beamline P08 at PETRA III (Fig. 5.5), DESY in Hamburg.
Transmission XRD experiments enable to probe the confined polymer structure to reveal its potential ordering. Fig. 5.6 shows the scattering geometry. Samples of 200 µm thickness were mounted in a way that the pore axis is horizontal and the rotation is performed about the vertical axis $\chi$ in increments of 2°. Such rocking scans from 0° to 90° were performed from 300 K to 380 K to elucidate the thermal stability of the polymer morphology. An X-ray beam of energy 24 keV was used to reduce the absorption in the 200 µm thick samples. A Perkin-Elmer area detector was used for intensity mapping. High flexibility of the set up was

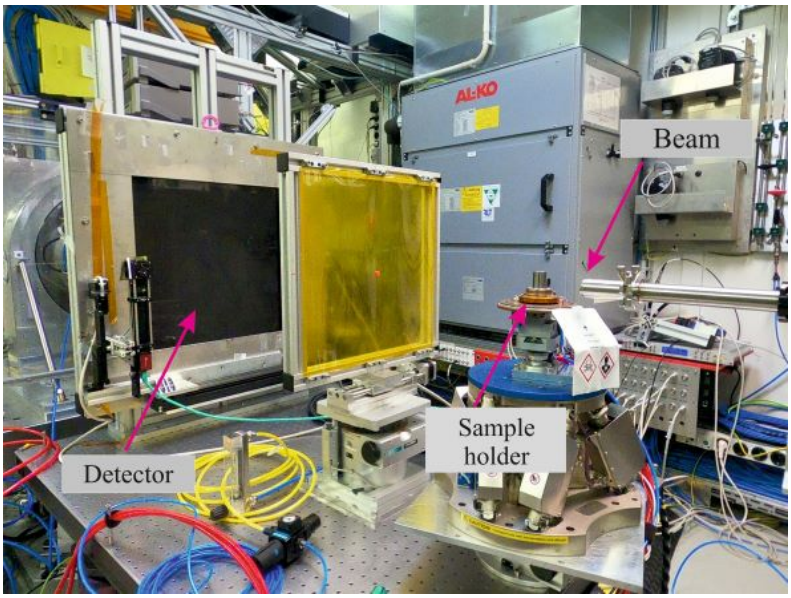


**Figure 5.5:** P08 experimental hutch with area detector, sample holder with beryllium cap and the beamline.

achieved by using the goniometer with a horizontal rotation and x, y, z translation stages.
The thiophene ring stacking gives rise to a (010) reflection at wavevector transfer $q \approx 1.7\,\text{Å}^{-1}$. The hexyl-side chains separating thiophene rings give rise to a (100) lamellar reflection at $q \approx 0.37\,\text{Å}^{-1}$. At the beginning of the scan, ($\chi = 0°$), the beam hits the hybrid perpendicular to the membrane top surface, and as the sample rotates to $\chi = 90°$, the grazing-incidence SAXS (GISAXS) geometry can theoretically be reached.

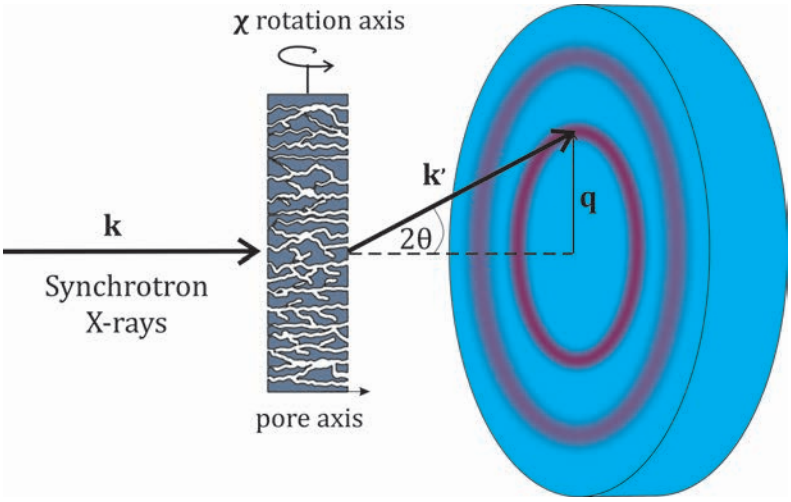


**Figure 5.6:** Scattering experiment geometry: X-rays hits the sample perpendicular to the surface and along the pore axis. The sample can rotate along the vertical axis from 0° to 90°.

The 2D intensity maps were collected by scanning the hybrid sample with a beam size of 200 µm x 200 µm. At a given temperature, the sample at a particular rotation angle $\chi$ was scanned twice to obtain a good signal-to-noise ratio. To

avoid beam damage, the sample was moved in the vertical direction by 0.4 mm after each scan, with an exposure time of 2 s for each scan.
Due to the mechanical structure of the hybrid and the fact that the polymer filling is not even at the edge of the membrane, a slight bending of the hybrid can be observed. Because of this bending, a well-defined GISAXS geometry can practically not be realized.

### 5.2.3 Absorption of light

Absorption spectroscopy includes techniques in which the absorption of light by the specimen occurs at a particular wavelength. The resulting absorption spectrum can be characterized to determine composition, structural information as well as electronic structure information on the specimen depending of the sample and range of the electromagnetic spectrum.
During the photoelectric absorption process, a photon is absorbed by the atom and its energy is transferred to an electron. At sufficiently high energy transfers, the atom is ionized and the electron is ejected [135]. This photoelectric absorption is given by the absorption coefficient $\alpha$. The attenuation of the beam through a thickness $dz$ at a depth $z$ from the surface is defined as $\alpha dz$ [135]. The depth-dependent intensity $I(z)$ becomes

$$I(z) = I_0 e^{-\alpha z} \tag{5.15}$$

with incident intensity $I_0$.

### 5.2.4 UV-Vis

UV-Vis spectroscopy is an analytical technique probing the amount of ultraviolet or visible light absorbed by a sample. It is measured in comparison to the reference sample, made from the same material as the sample cell. Absorption occurs when electrons are excited to higher energy states upon illumination. The measurement results in an absorbance spectrum as a function of the wavelength (Fig. 5.7). This method is commonly used to analyze organic materials, but also serves as an important tool for inorganic materials characterization [136].
The absorbance is defined as [137]

$$A = -log_{10}\left(\frac{I}{I_0}\right) = \frac{\alpha d}{2.3} \tag{5.16}$$

with an optical absorption coefficient $\alpha$ and under consideration of Eq. 5.15 with the sample thickness d.
The absorbance depends on the probability $P$ for the transition between two electronic states and the effective density of states for initial and final states that comply with energy and momentum conservation.
In 1966 J. Tauc [138] proposed the relation

$$(\alpha \cdot h\nu)^{1/r} = B(h\nu - E_g) \tag{5.17}$$

to extract the optical band-gap $E_g$ directly from the absorption spectra. Here $\nu$ is the energy of the absorbed photon and $r$ depends on the nature of the electronic transition. Motivated by analytical calculations of $\alpha$, assuming parabolic and

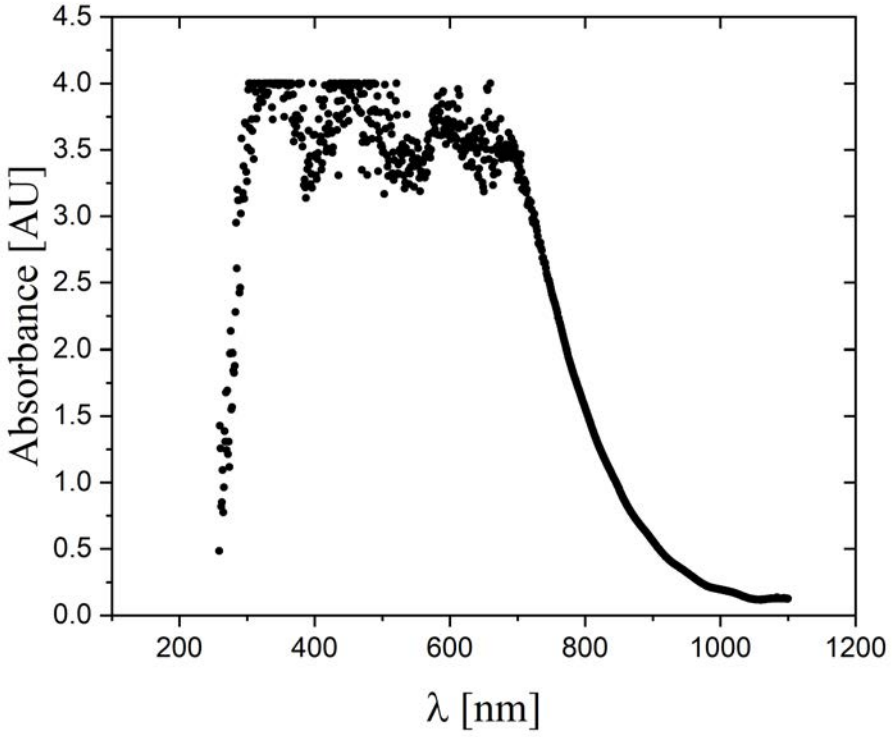


**Figure 5.7:** A representative measurement of the porous silicon sample. Absorbance spectrum measured in the wavelength range from 200 nm to 1100 nm.

isotropic bands, one gets $r = 2$ for indirect and $r = 1/2$ for direct transitions [138, 139].

## 5.3 Scanning electron microscope

### 5.3.1 Electron as a wave

Louis de Broglie discussed in his doctoral thesis [140] that particles such as the electron also have wave properties. The wavelength of an electron, known as the de Broglie wavelength $\lambda$, is associated with the wavevector $k = 2\pi/\lambda = p/\hbar$, where $p$ is the particle momentum. The acceleration of an electron with mass $m_0$ and acceleration voltage $U$ results for instance in a de Broglie wavelength of

$$\lambda = \frac{h}{\sqrt{2m_0eU}}. \tag{5.18}$$

From the modern but equivalent quantum mechanics' point of view, electrons are represented by a wave function that describes the probability density of finding this particle at a given point in space. The wave function of a free electron is

$$\Psi(x,t) = Ae^{\frac{i}{\hbar}(px-Et)}. \tag{5.19}$$

$A$ is the amplitude of the wave function, $E$ its energy ($E = p^2/2m$) [119]. The probability density of finding a particle in an interval $\Delta x$ about the position $x$

at time t is $|\Psi(x,t)|^2\Delta x$.
The wave nature of electrons can be exploited to probe matter and perform diffraction experiments [119].

### 5.3.2 Electron microscopy

Scanning electron microscopy is a versatile method to examine the morphology and chemical composition of a specimen [141]. It is commonly used in scientific and technical fields. Utilizing an electron beam to replace light in microscopy investigations has been a great advance in scientific research. The limitations of optical microscopy come from the source beam, where magnification of an image through optical lenses results in maximum resolution of about 2000 Å [141].
The spatial resolution $d$ of an optical microscope depends on the wavelength $\lambda$ of the light source used, the refraction index $n$ of the medium between the sample and the microscope optics and the angle of acceptance $\theta$ over which the optical system collects light from the sample spot [141]. According to Abbe, it is

$$d = \frac{0.612 \cdot \lambda}{n \cdot sin(\theta)}. \tag{5.20}$$

The denominator is also referred to as numerical aperture.
From Abbe's equation it becomes evident that the resolution of optical microscopes is limited by the wavelength of visible light. But it also provides the ingenious insight that a microscope that exploits the wave character of electrons allows for atomic resolution. The wavelength of electrons, and consequently the resolution of an electron microscope, is defined by the acceleration voltage between cathode and anode. Electrons with higher kinetic energy have shorter wavelength, therefore the resolution of the system is increased. The relation between the wavelength and acceleration voltage ($U$) is, employing relativistic correction, is [142]

$$\lambda = \frac{h}{\sqrt{2m_0 \cdot e \cdot U(1 + \frac{e \cdot U}{2m_0 \cdot c^2})}}, \tag{5.21}$$

where $m_0$ is the electron rest mass, $e$ is the electron charge and $c$ is the speed of light. For the 100 keV acceleration voltage the wavelength is about 3.9 pm.
A scanning electron microscope employs this principle to achieve atomic resolutions for sample characterization. Electron guns are used to produce a stable electron beam with high current, small spot size and adjustable energy. The beam is focused by magnetic fields in electromagnetic lenses and, after hitting the specimen surface, the electron signal is collected by detectors. SEM requires ultra-high vacuum, which is indispensable to avoid electron beam scattering and contamination of electron guns [142].
Accelerated electrons interact with a specimen in two ways, elastic and inelastic scattering. Various interaction processes have their information volume, a depth-volume that depends on the energy spectrum of emitted electrons. The contribution to the spectrum comes from secondary electrons (SE), backscattered electrons (BSE) and Auger electrons (AE) [142]. SE are generated by inelastic collisions but are highly susceptible to both elastic and inelastic scattering. Because of that, the secondary electrons can escape the specimen from the surface

layer that is only about a few nanometers thin [142]. The AE, which can provide similar information as characteristic X-ray emission after ionization, have also limited escape depth. SE give information on the topographic level and can be easily collected owing to their low exit energy. Backscattered electrons are reflected from the sample by elastic scattering. The backscattering coefficient depends on the mean atomic number ($\overline{Z}$), which allows to contrast the sample by means of phases with different $\overline{Z}$.
In 1986 Ernst Ruska was awarded the Nobel Prize in Physics "for his fundamental work in electron optics, and for the design of the first electron microscope" [143]. In 1931 together with Max Knoll they designed the first electron microscope at the Berlin Technische Hochschule which revolutionized what is now called nanoscience [143].

### 5.3.3 Energy dispersive X-ray spectroscopy

When the electron beam strikes the sample, another important signal is produced. The emission of characteristic X-rays is of great importance to further investigate the material, as it provides chemical information about the specimen's composition [142]. It is the most widely used microanalytical technique.
The incident beam can excite and eject an electron from the sample's atomic inner shells. The remaining hole is filled by an electron from the outer shells, accompanied by X-rays emission that results from the energy difference between the two states. The energies of the emitted X-rays are characteristic to a specific atom, therefore an analysis of the X-ray spectrum by an energy-dispersive spectrometer (EDX) gives important information about the sample's elemental composition. By scanning a sample with an electron beam one can collect maps of elemental composition [141].
EDX analyzers are the most widely used option for SEM devices. The imaging and energy dispersive X-ray spectroscopy mapping of the hybrids' cross-section is performed utilizing a LEO GEMINI 1530 UltraPlus (Zeiss) electron microscope. The characteristic energies for the elements in question are listed in Tab. 5.1.

**Table 5.1:** Characteristic energies for silicon, sulfur, chlorine and iron.

| Element | Characteristic energy [keV] |
|---|---|
| Si (pSi) | $K\alpha$ 1.74 |
| S (P3HT) | $K\alpha$ 2.30 |
| Cl (dopant) | $K\alpha$ 2.62 |
| Fe (dopant) | $K\alpha$ 6.398 |
| | $L\alpha$ 0.705 |

### 5.3.4 Sample preparation and signal acquisition

In order to probe the polymer distribution in the porous matrix, EDX mapping was performed on cross-sectional surfaces of the hybrid samples. Just before the characterization, the samples were cracked and mounted on the sample holder. The beam approaches the sample from the bottom and the detector collects the signal from the opposite side of the sample. The elemental map is created by scanning the area line by line.

## 5.4 Seebeck analyzer

Simultaneous determination of electrical conductivity ($\sigma$) and Seebeck coefficient ($S$) is performed in a SBA 458 Nemesis device by Netzsch [144]. The experimental set-up consists of two current pins and two thermocouples for measuring voltage and temperature. Two micro-heaters are placed under the sample edges to create a temperature gradient in two directions.
An electrical connection utilizing 4 separated probes precisely measures the sample's resistance $R_S$ excluding cable and contact resistances, minimizing errors. Fig. 5.8 shows the measurement set-up. The current injected to the circuit from the current pins (rhodium probes) passes exclusively through the sample and the voltage drop is measured with separated voltage contacts.

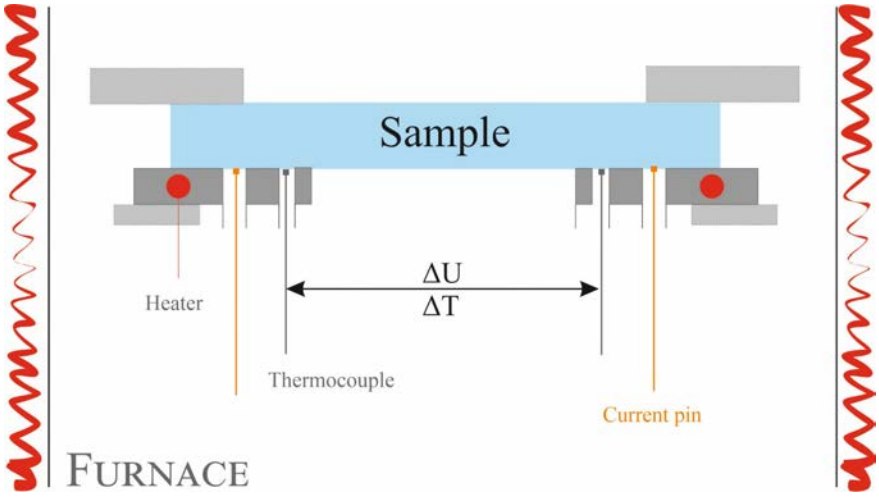


**Figure 5.8:** Measurement set-up of the SBA 458 Nemesis by Netzsch.

During the measurement, at each temperature point, different current values are applied to the sample through current injection pins in two directions and the resulting voltages are measured. The resulting I-V curves are straight lines indicating ohmic behavior (Fig. 5.9). The sample sheet resistance is determined by the slope of the I-V curve $R_S = \Delta V/\Delta I$ and the resistivity ($\rho = 1/\sigma$) is further calculated using the sample's geometric dimensions.
The Seebeck coefficient is measured in the same configuration. Once the electrical conductivity is determined for a given temperature, a temperature gradient is generated in both sample directions by micro-heaters. A temperature difference of 5 K is created and the voltage change is measured by the voltage pins, which also serve as thermocouples. The relative Seebeck coefficient of the sample is measured with respect to a platinum reference sample. In terms of the control parameter $\Delta T$ and the measured voltage $V$ it is

$$S(T) = -\frac{\partial}{\partial \Delta T} V(\Delta T)\bigg|_T. \tag{5.22}$$

## 5.5 Laser flash analysis

The thermal diffusivity D is a measure of the rate of heat transfer in a material. To measure D Parker et al. [145] introduced in 1961 the laser flash analysis (LFA)

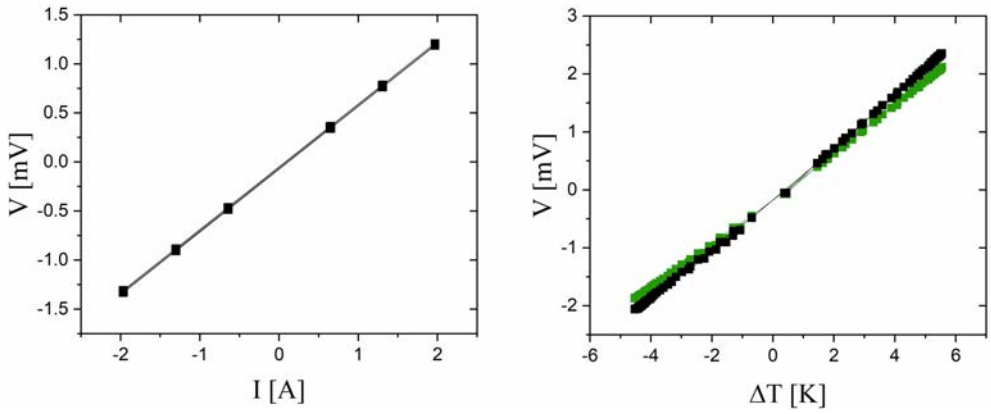


**Figure 5.9:** I-V curve and Voltage-ΔT plot for electrical conductivity and Seebeck coefficient determination.

technique. It is a non-steady state thermal characterization method.
In a vertical set-up, a short laser pulse heats up the bottom side of the sample. The subsequent heat transfer to the top side is measured as the temperature response with an IR-detector. This T-response (Fig. 5.10) relates directly to the diffusivity. In Parker's model it is

$$D = \frac{0.138}{t_{1/2}} d^2, \tag{5.23}$$

where $d$ is the sample thickness and $t_{1/2}$ is the time at which the sample reached half of the maximum temperature.

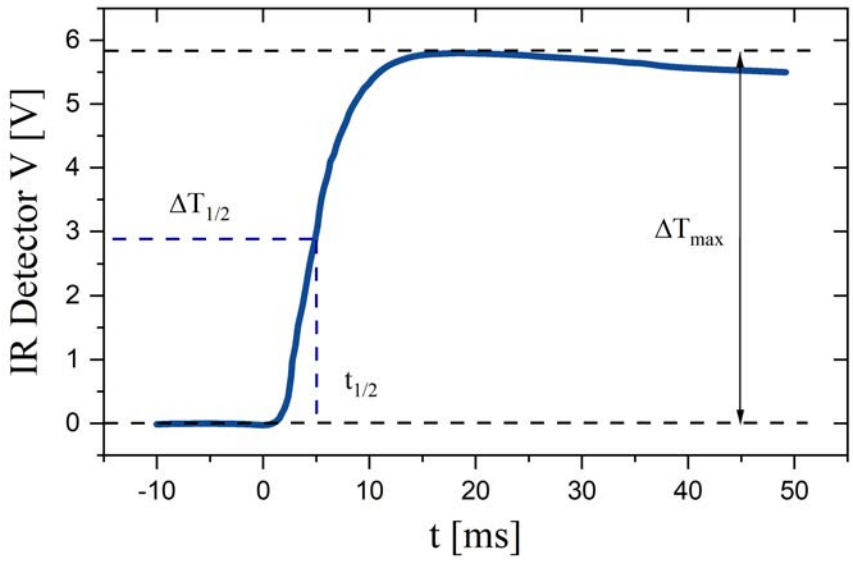


**Figure 5.10:** Overview chart presenting the detected voltage in time.

Parker's model is restricted to near-adiabatic conditions, which occur for high thermal diffusivity samples and short measurement duration. In case of heat loss by radiation and convection, more advanced models have been proposed to describe experimental data [146, 147].

It is elementary to relate the diffusivity to the thermal conductivity $\kappa$

$$\kappa(T) = D(T) \cdot \rho(T) \cdot c_p(T). \tag{5.24}$$

Here, $\rho(T)$ and $c_P(T)$ are the sample density and the specific heat capacity.
The LFA method certainly has the advantage of being fast, contactless and generally non-destructive. This method is recommended for high-temperature measurements of homogeneous samples, which creates limitations for the T-range and samples used.

## 5.6 Physical Property Measurement System

The Physical Property Measurement System (PPMS) is a versatile device for measuring various temperature- and field-dependent material properties. Automated measurements allow to determine material properties such as heat capacity, resistivity and thermal conductivity. Measurements were performed in the T-range $1.9\,K - 320\,K$.

### 5.6.1 Heat Capacity

The PPMS measures the heat capacity at constant pressure $C_p = (dQ/dT)_p$. The basic idea of the measurement is to probe the thermal response of a sample, that is in contact with a thermal bath $T_b$, upon resistive heating P(t). This temperature response obviously encodes $C_p$. It is

$$C_p \frac{dT}{dt} = -K_W(T - T_b) + P(t). \tag{5.25}$$

Here, $K_W$ is the thermal conductance towards the thermal bath with temperature $T_b$, T is the temperature of the sample and $P(t)$ is the power applied by the heater.
One solution of Eq. 5.25 is

$$T - T_b = (T_{max} - T_b)e^{-t/\tau}. \tag{5.26}$$

It applies after turning off the resistive heating at $t = 0$ with a characteristic time constant $\tau = K_w/c_p$ and $T_{max} = T(0)$
The measurement requires high vacuum to minimize parasitic losses via convection. An initial $C_p$ measurement of the empty sample holder (with grease) is required to obtain good accuracy of the sample's heat capacity. The sample is mounted to the holder with a thin layer of grease to provide thermal connection and support.

### 5.6.2 Thermal conductivity

The thermal conductivity transport option in a PPMS allows to measure the thermal conductivity of rod- or bar-like shaped samples. Resistive heating with power P(t) at one end of the sample induces heat flow to the other end that is connected with a heat sink. Under steady state conditions a t-independent temperature gradient develops along the sample. It is measured with spatially separated thermocouples.

If one accounts additionally for radiation losses $R_L$, one can determine the sample's thermal conductivity using Fourier's law

$$\kappa_{PPMS} = \frac{P - R_L}{\Delta T} \frac{l}{A}. \tag{5.27}$$

Here $\Delta T$ is the steady state T-difference between the thermocouples separated by a distance $l$ and $A$ is the sample's cross-section [148].

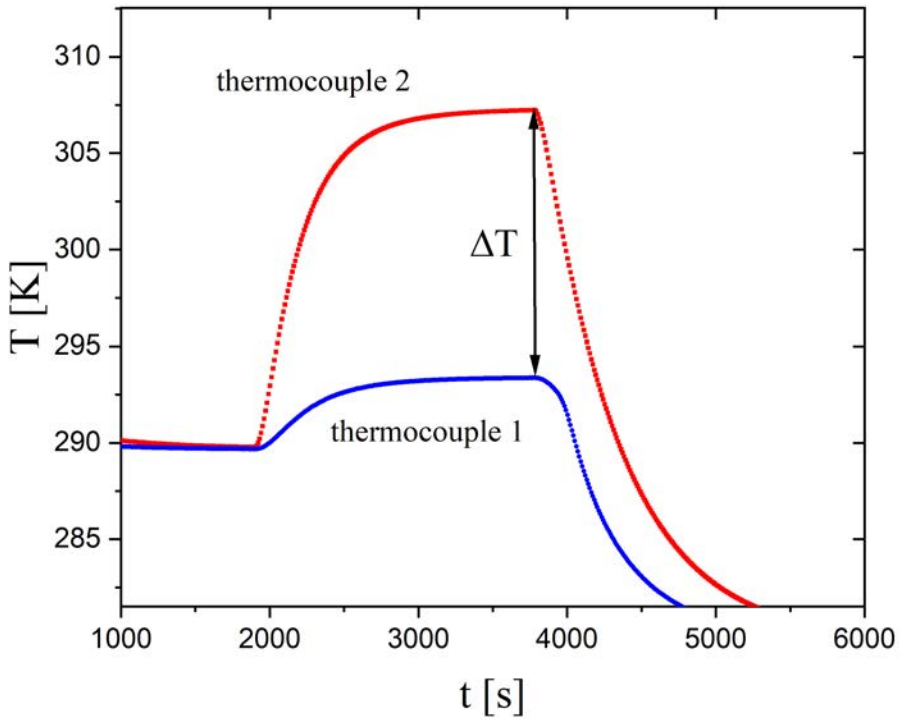


**Figure 5.11:** Temperature response of the thermocouples during thermal conductivity measurement.

# Chapter 6

# Synthesis

## 6.1 Porous silicon

Mesoporous silicon is synthesized by means of electrochemical anodization in hydrofluoric acid (HF) based electrolytes. The source materials are single-crystalline boron-doped [100] Si wafers with a resistivity of $\rho = 0.01$ - $0.02\,\Omega\,\mathrm{cm}$, according to the supplier's specifications. For electrochemical etching, we utilize a novel, custom-built anodization cell designed by Gostkowska-Lekner et al. (see key publication P.1) and developed as part of this PhD thesis. The closed cell consists of a double-walled container to avoid any hazardous electrolyte contact with the user and at the same time to minimize liquid evaporation. The design comes with the pumping system utilizing a peristaltic pump for electrolyte transfer (Fig. 6.1) and a custom-made LabVIEW$^{\mathrm{TM}}$ - based control software that allows for user-defined etching profiles. The cell design and software control are discussed in detail in Sec. 2.2.2.

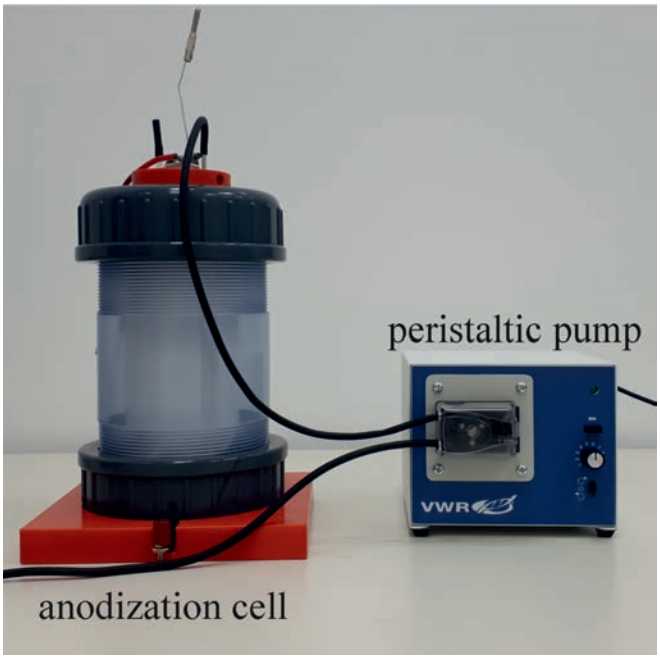


**Figure 6.1:** Anodization cell and peristaltic pump. Published in (P.1).

Electrolyte composition and anodization current are key synthesis parameters. Membranes for this study are anodized in HF(48 wt.%)/ethanol(99.9 wt.%) so-

lution ($HF : C_2H_6O = 4 : 6$) with a constant current density of $j = 13\,\mathrm{mAcm^{-2}}$. Such selection of substrate and etching parameters allows to obtain a free-standing membrane with good mechanical properties as well as pore size and porosity that allow for effective phonon scattering and embedding of functional molecules in the pore space. An anodization time of 5 h leads to the growth of a 200 µm thick epilayer on the bulk Si wafer with pores roughly 9 nm across. A typical etching profile is shown in Fig. 6.2. The anodization ends with an increased current density of $j = 52\,\mathrm{mAcm^{-2}}$ for 40 s to detach the epilayer from the wafer and to obtain a self-supporting pSi-membrane with diameter of 5 cm (Fig. 6.3). The voltage rise is followed by a sharp drop, which indicates successful detaching. The detached membrane is further washed several times with water and ethanol and dried in air.

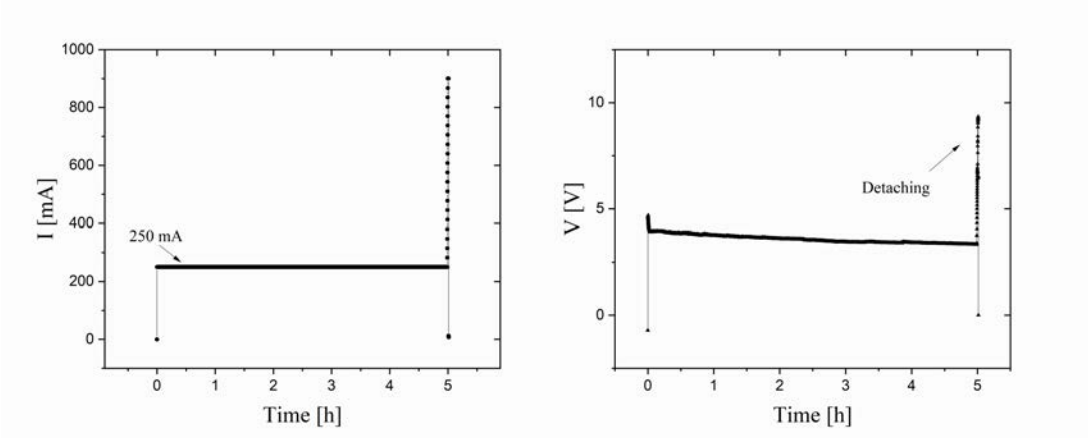


**Figure 6.2:** Current and voltage profiles during the etching process. The change in both I and V at the end of the anodization marks the detaching process.

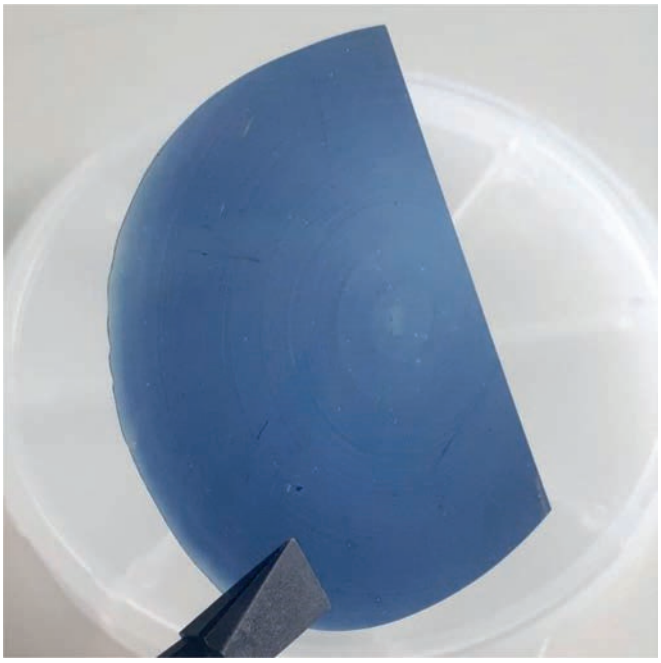

**Figure 6.3:** Free-standing porous silicon membrane.

## 6.2 Hybrid synthesis

The P3HT was embedded in the pSi pore space by means of melt infiltration. The regioregular (> 90%) P3HT powder with low molecular weight ($M_W$ = $2 \times 10^4\,\mathrm{gmol}^{-1}$ to $4.5 \times 10^4\,\mathrm{gmol}^{-1}$) was purchased from Sigma Aldrich™ and used as received. Adopting low molecular weight P3HT with a small radius of gyration reduces potential pore clogging [149]. The as-etched pSi membrane is heated up to 550 K, a temperature well above the melting point of P3HT ($T$ = 510 K). The polymer powder placed on top of the heated membrane melts and flows into the nanochannels due to capillary forces [76]. The sketch in Fig. 6.4 shows a visualization of the process. The synthesis of P3HT-pSi hybrids is thoroughly discussed by Gostkowska-Lekner et al. (see key publication P.2).

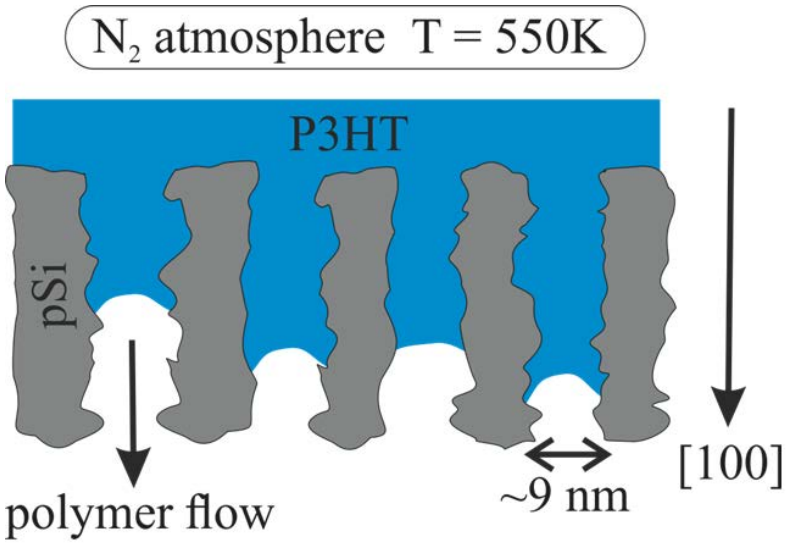


**Figure 6.4:** Melt infiltration of P3HT into silicon mesopores.

The polymer flow in the nanochannels is an exceptionally slow process due to the high viscosity of the polymer liquid (99 Pa · s) [150]. It takes up to 48 h to fill the pores of the membranes as discussed below in detail. After cooling to room temperature a residual P3HT layer that is not embedded in the pores is removed with a cotton swab and chloroform. One should also note that the entire imbibition procedure is conducted in a glove box in an inert nitrogen atmosphere to avoid polymer oxidation and degradation upon illumination in air [151].
Conjugated polymers in their neutral stable state conduct electricity rather poorly because of their large band-gap. It is of importance to improve their electrical conductivity by means of doping to compete with the traditional inorganic semiconductors [152]. Solution-based chemical doping is one of the most popular and straightforward methods to incorporate doping counter ions into the polymer structure as discussed in Sec. 3.2.1. Synthesized hybrids are doped by immersion in saturated $FeCl_3$ chloroform solutions for 48 h or 72 h. The doping procedure takes place in a glove box under an inert atmosphere.
Obtaining high degrees of polymer fillings was a challenging task. Drop casting of the P3HT solution on top of the pSi prior to heating resulted in minimal imbibition depths. The amount of P3HT deposited on the pSi membrane after several cycles of drop casting was insufficient to fill the pores even at a depth of several

micrometers. Doping P3HT prior to infiltration caused unfavorable aggregation of the polymer, which hindered the melt infiltration process. The post-imbibition doping successfully incorporated the doping agents into the P3HT matrix without affecting the melt imbibition process.

# Chapter 7

# Structural characterization

## 7.1 Mesoporous silicon

Mesoporous silicon is morphologically characterized with sorption isotherms and SEM images. The BJH sorption isotherm analysis allows to extract the pore size distribution of the as-etched membrane. The typical distribution is presented in Fig. 7.1 where the mean pore radius is 4.5 nm. The pore size distribution justifies the characterization of anodized silicon as mesoporous. The porosities of self-supporting membranes vary in general between $60\% - 65\%$ with specific surface areas of about $A = 380\,\mathrm{m}^2/\mathrm{g}$.

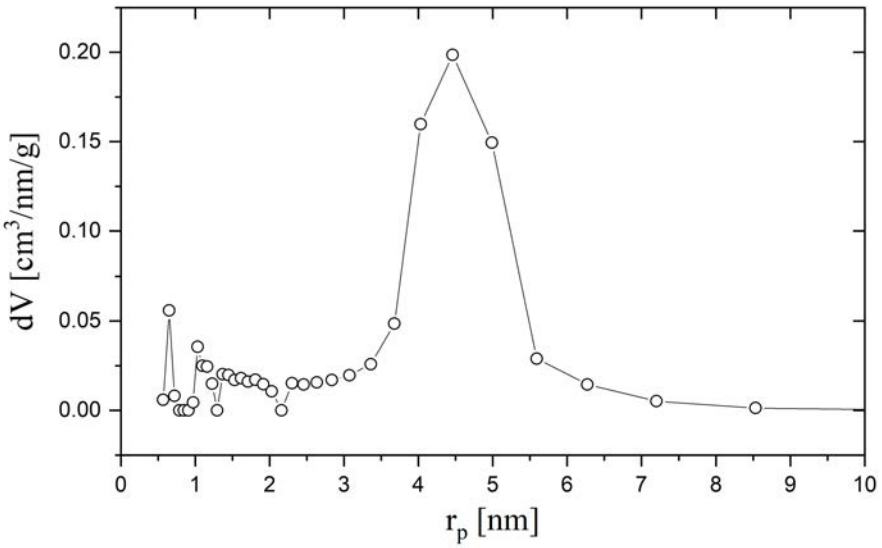


**Figure 7.1:** Pore size distribution of a pSi sample with 62% porosity.

The pore formation progresses in a specific crystal direction [100] of the silicon wafer, but the structure of the porous membrane is rather rough and dendritic. The pore forms a multi-connected sponge-like structure. The pores grow along the [100] direction with dendritic side branches. The branching is caused by the fact that the pore walls are depleted of charge carriers but not completely devoid of them [18]. The relation between porosity and pore diameter is highly dependent on the etching conditions which affects the pore wall morphology. The surface of the etched pSi is hydrogen terminated, but it covers itself with a

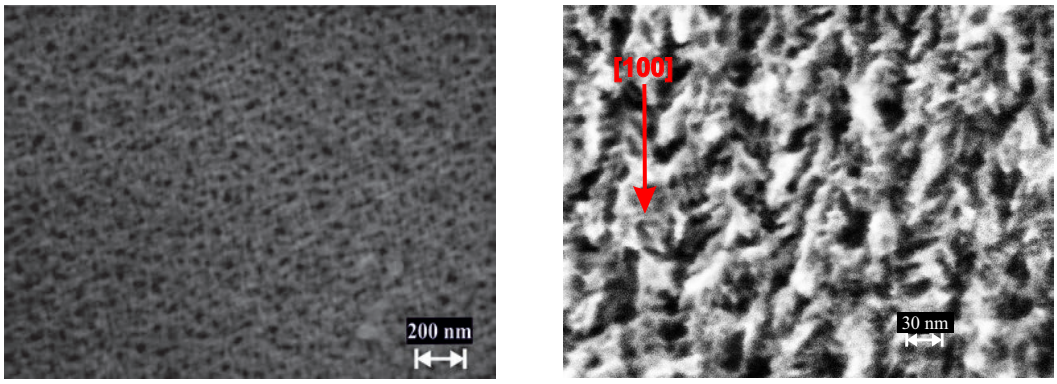


(a) (b)

**Figure 7.2:** SEM images of pSi a) top view and b) cross-section. Published in (P.2).

silicon-oxide layer when dried in air. The oxide can be removed by immersing the pSi in HF which can also lead to changes in pore morphology and pore channel smoothness [153].
Fig. 7.2 shows SEM images of silicon membranes, both top view and cross-sectional view. The pore shape does not necessarily resemble round, cylindrical structures and the cross-section image reveals a dendritic pore network. This pore architecture can affect the imbibition process of the guest molecules [112]. The interconnected pores are filled by means of capillary forces as the melt propagates through the membrane.

## 7.2 P3HT-pSi hybrids

The amount of P3HT incorporated into porous silicon pores is described with a filling factor $f$, that is the percentage of pore space occupied by P3HT. It is determined with three different methods. EDX mapping, gravimetry and sorption isotherms are employed to find $f$.

### 7.2.1 EDX spectroscopy

EDX spectroscopy provides a detailed elemental map, here probed on the cross-sectional area of the P3HT-pSi hybrids. The presence of characteristic elements (Si, S, Fe) manifests in depth dependent EDX signals $I^{EDX}(x)$. Such signals can be used to define the degree of polymer filling. We assume that the EDX signal for selected elements is proportional to the amount of polymer in the pores. The polymer-specific element in the hybrid is sulfur, the heteroatom in the aromatic ring, which is used as the main signal source for the analysis. With the assumption that the pores on top of the membranes are filled completely, one obtains

$$f_p^{EDX} = \frac{\int I^{EDX}(x)dx}{I^{EDX}(0)\int dx}. \tag{7.1}$$

To estimate the filling factor with EDX, the sulfur signal is integrated over the cross-section and normalized to the signal at the top of the membrane multiplied with the membrane thickness.

EDX spectroscopy provides the most striking proof for successful P3HT imbibition. By the very design of the conceived synthesis route, the polymer melt flows into the pore network from the top of the membrane and a liquid polymer front propagates along the [100] crystallographic direction. As an instructive illustration, Fig. 7.3 shows the polymer filling at an intermediate state after 7 h. The EDX sulfur signal clearly evidences that the membrane is filled up to a depth of 80 µm and the sharp transition between filled and empty pSi is evident. In contrast, Fig. 7.4 indicates the presence of P3HT across the entire membrane after an imbibition time of 48 h.

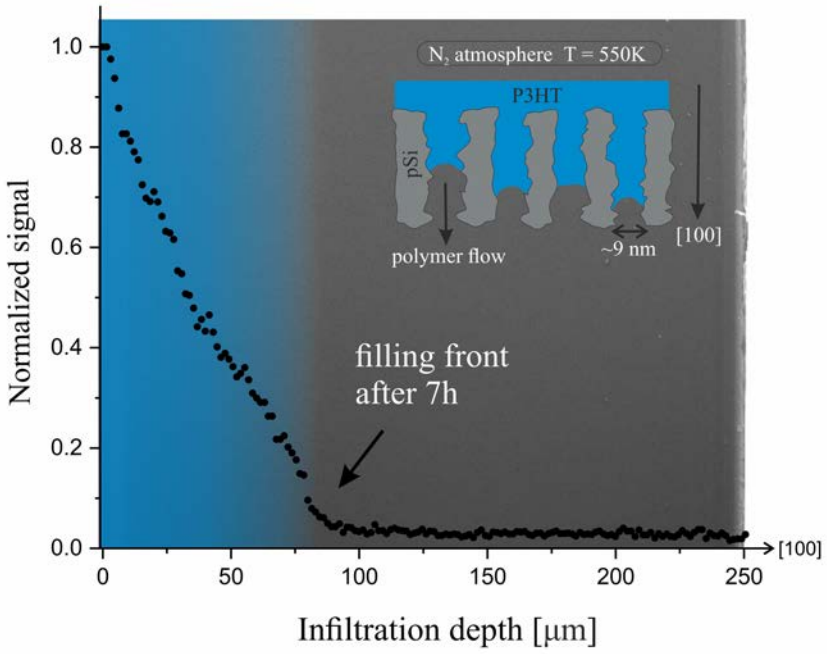


**Figure 7.3:** PSi membrane partially filled with P3HT: Sample cross-section and EDX sulfur signal (symbols) as function of depth. The membrane was etched for 7 h. The blue color indicates the filling region. The inset sketches the polymer flow into the pore space. Published in (P.2).

However, the underlying assumption that the signal at the top of the membranes represents complete filling has to be taken with caution. It is experimentally almost inevitable to probe part of the membrane surface along the first few microns of the depth scan and consequently to overestimate $I^{EDX}(0)$.
Some additional insights are gained from the fact that the strength of the sulfur signal decays continuously across the membrane. The most appealing explanation is that the imbibition involves two different time-scales [76, 110]. In this scenario, the polymer melt wets the pore walls on a "fast" time scale as it creeps along the pore surfaces through the channels while the center remains empty. Then on a significantly "slower" time scale polymer in the pore center follows this precursor film.
In a less sophisticated explanation, one would assume that the polymer flow is increasingly impaired by bottlenecks in the channels as the liquid front propa-

gates along the pores. This could readily lead to a depth gradient in the polymer distribution and consequently a decaying EDX sulfur signal.
Despite the issues with the maximum signal at the top of the membrane, EDX mapping of the doped hybrids shows successful incorporation of $FeCl_3$ dopant atoms into the polymer matrix. In the element map of Fig. 7.4 one can distinguish the distribution of silicon, sulphur, iron and chlorine as a result of the discussed synthesis approach.
It is remarkable, that the signals from iron and chlorine which are characteristic of the dopant exhibit exactly the same decaying profile along the pore channels as the sulfur signal which is characteristic for the polymer. This clearly indicates successful diffusion of the doping agents into the polymer matrix contrary to physisorption of the $FeCl_3$ simply onto silicon pore walls or vacant pore space.

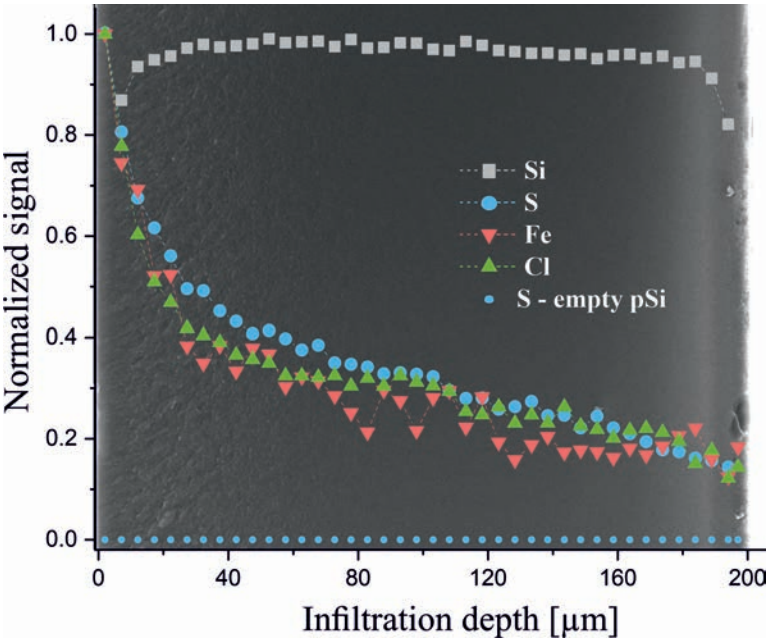


**Figure 7.4:** Doped pSi-P3HT hybrid (48 h): EDX signals (symbols) of silicon, sulfur (P3HT), chlorine (dopant) and iron (dopant). The vanishing sulfur signal in the empty pSi membrane serves as reference. The background shows the membrane cross-section. Published in (P.2).

### 7.2.2 Sorption isotherm

The sorption isotherms of hybrids are also used to estimate the degree of filling. Estimating the empty pore volume $V_p$ from sorption isotherms that are measured prior and post filling results in an polymer filling fraction $f_p^{iso}$ of

$$f_p^{iso} = 1 - \frac{V_p^{post}}{V_p^{prior}}. \tag{7.2}$$

A comparison of the cumulative pore space in both as-etched and filled pSi samples is shown in Fig. 7.5.
The degree of polymer filling obtained from the sorption isotherms could be biased by pore clogging. The dendritic growth of the pores comes along with

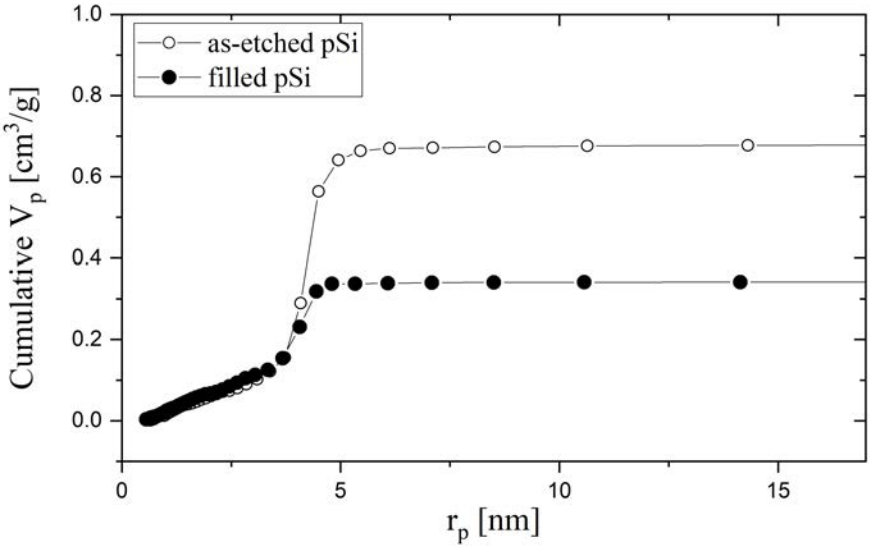


**Figure 7.5:** Cumulative pore volume of an as-etched pSi membrane (open symbols) and vacant pore space after polymer imbibition (black symbols).

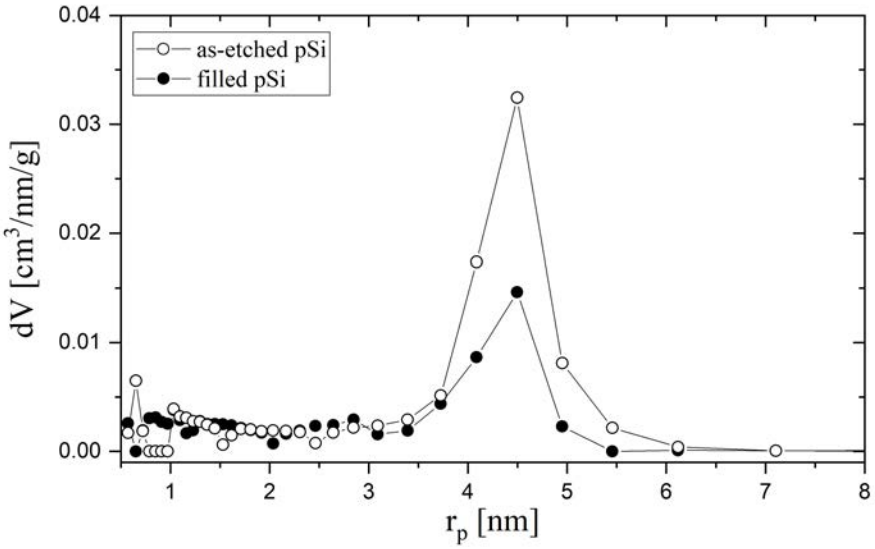


**Figure 7.6:** Pore-size distribution of an as-etched pSi membrane (open symbols) and vacant pore space after polymer imbibition (black symbols).

bottlenecks between wider pores. These bottlenecks and consequently some connected pores are not filled during imbibition. In particular, isolated islands of empty pore space within the otherwise filled substrate form. The volume of these islands is not probed by the $N_2$ isotherms due to a lack of access over the filled pore network. Therefore, $f_p^{iso}$ is prone to overestimating the degree of pore filling. Fig. 7.6 shows the comparison between the pore-size-distribution of as-etched membrane and that of a P3HT-filled membrane. The amount of pore space available for nitrogen is significantly decreased. Comparison to the filling factors obtained with the gravimetric method does not show heavy susceptibility

to pore clogging (Tab. 7.1).

### 7.2.3 Gravimetry

Gravimetry provides an alternative, quantitative estimate of the degree of polymer filling in the membranes. The mass of the empty membrane $m_e$, the mass of the filled membrane $m_f$ and the empty membrane's pore volume $V_p$ as obtained from the sorption isotherm predict a polymer filling of

$$f_p^{grav} = \frac{m_f - m_e}{\rho_{P3HT}} \frac{1}{V_p}, \tag{7.3}$$

where $\rho_{P3HT}$ is the polymer density.
The filling fractions $f_p^{grav}$ for selected samples based on Eq. 7.3 are around $40\% < f_p^{grav} < 50\%$ as seen in Tab. 7.1. These values are slightly lower than the ones obtained from sorption isotherms. The method provides no uncertainty related to signal overestimation or pore clogging and blocking, therefore the gravimetrically determined amount of pSi pore volume occupied by P3HT is the most accurate one. Together with nitrogen sorption isotherm measurements and SEM/EDX mapping there is no doubt about a successful infiltration of P3HT polymer into the mesoporous silicon membranes.

**Table 7.1:** Filling factor for 48h infiltration time: comparative characterization based on sorption isotherms, gravimetry, and EDX cross-section scan.

| Small area samples ($< 50$ mm$^2$): | Sorption Isotherm | Gravimetry | EDX |
|---|---|---|---|
| Hybrid 1 | 49.8% | 41% | 19% |
| Hybrid 2 | 55% | 45% | 21% |
| Large area samples ($> 50$ mm$^2$): synthesized for SBA measurements | | | |
| Hybrid 3 | - | 55% | 30% |
| Hybrid 4 | - | 52% | 31% |
| Hybrid 5 | - | 50% | 28% |
| Hybrid 6 | - | 45% | 22% |
| Hybrid 7 | - | 37% | 19% |

### 7.2.4 X-ray scattering experiments

The orientation of thiophene rings and polymer backbones define strongly the charge carrier transport in P3HT. To investigate the polymer structure inside porous silicon pores, temperature-dependent SAXS scans were performed using synchrotron radiation on P08 at DESY. The (100) lamellar reflection at wavevector transfer $q \approx 0.37\,\text{Å}^{-1}$ corresponds to the hexyl-side chains arranged along the lattice parameter $a$. The reflection (010) at $q \approx 1.7\,\text{Å}^{-1}$ is caused by the thiophene ring stacking and corresponds to the lattice parameter $b$ (see Sec 5.2.2).
Utilizing the scattering geometry described previously in Sec. 5.2.2 it is possible to infer correlations between crystallographic direction and the pore orientation. The sample rotation $\chi$ enables us to probe the potential polymer configurations towards the pore walls. Using a photon beam energy of 24 keV ($\lambda = 0.5166\,\text{Å}$) the sample rotation angle at which the lamellar stacking perpendicular to the pore walls could be observed is $\chi = 90° - \theta = 88.25°$ according to

$$q = \frac{4\pi}{\lambda} sin(\theta). \tag{7.4}$$

For all samples and temperatures the (100) peak intensity increases monotonically as the $\chi$ increases, reaching a maximum at the angle 90°. Fig. 7.8 shows scans of the undoped hybrid measured at 300 K and 380 K. Fig. 7.7 presents the P3HT (100) peak intensities plotted against the effective thickness of the sample during the scan at selected rotation angles. It provides the information that the peak intensity increase scales simply with the amount of probed polymer. Moreover, if P3HT would form a texture in pSi pores, the (010) peak would show an intensity $\chi$-dependence complementary to the one of (100). In conclusion, no preferred orientation of the lamellar stacking with respect to the pore wall can be identified.

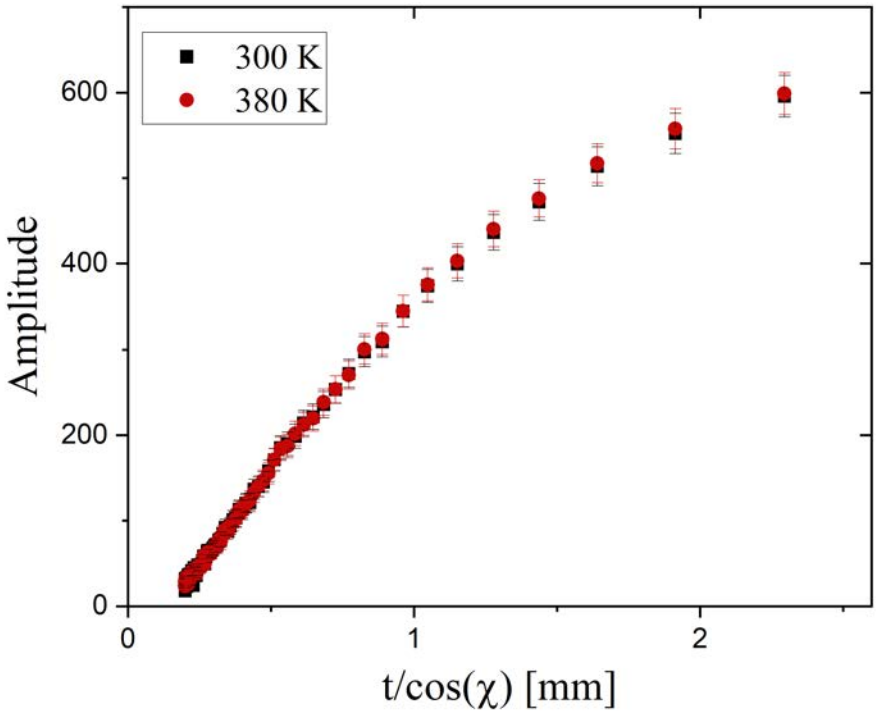


**Figure 7.7:** Intensity of the (100) peak in undoped hybrids as a function of sample's effective thickness.

At elevated temperatures, the peak position moves towards lower q values from 3.69 $nm^{-1}$ at 300 K to 3.59 $nm^{-1}$ at 380 K for undoped hybrids (Fig. 7.8). The lamellar, spacing, calculated for the given peak positions changes from 1.70 nm to 1.75 nm, showing the stretching of the hexyl-size chains with temperature.
The $FeCl_3$-doped hybrid exhibits similar behavior. Fig. 7.9 presents analogous rocking scans, where the doped hybrid is measured at 300 K and 380 K. The shift in (100) peak position is not as distinct as for the undoped sample, shifting from 3.48 $nm^{-1}$ at 300 K to 3.51 $nm^{-1}$ at 380 K. The corresponding change in the lattice constant for hexyl-size chains is 1.79 nm to 1.80 nm. The increased

lattice parameter $a$ is caused by the incorporation of dopant in the P3HT semi-crystalline structure and it is yet another proof of successful diffusion of those atoms into the confined polymer.

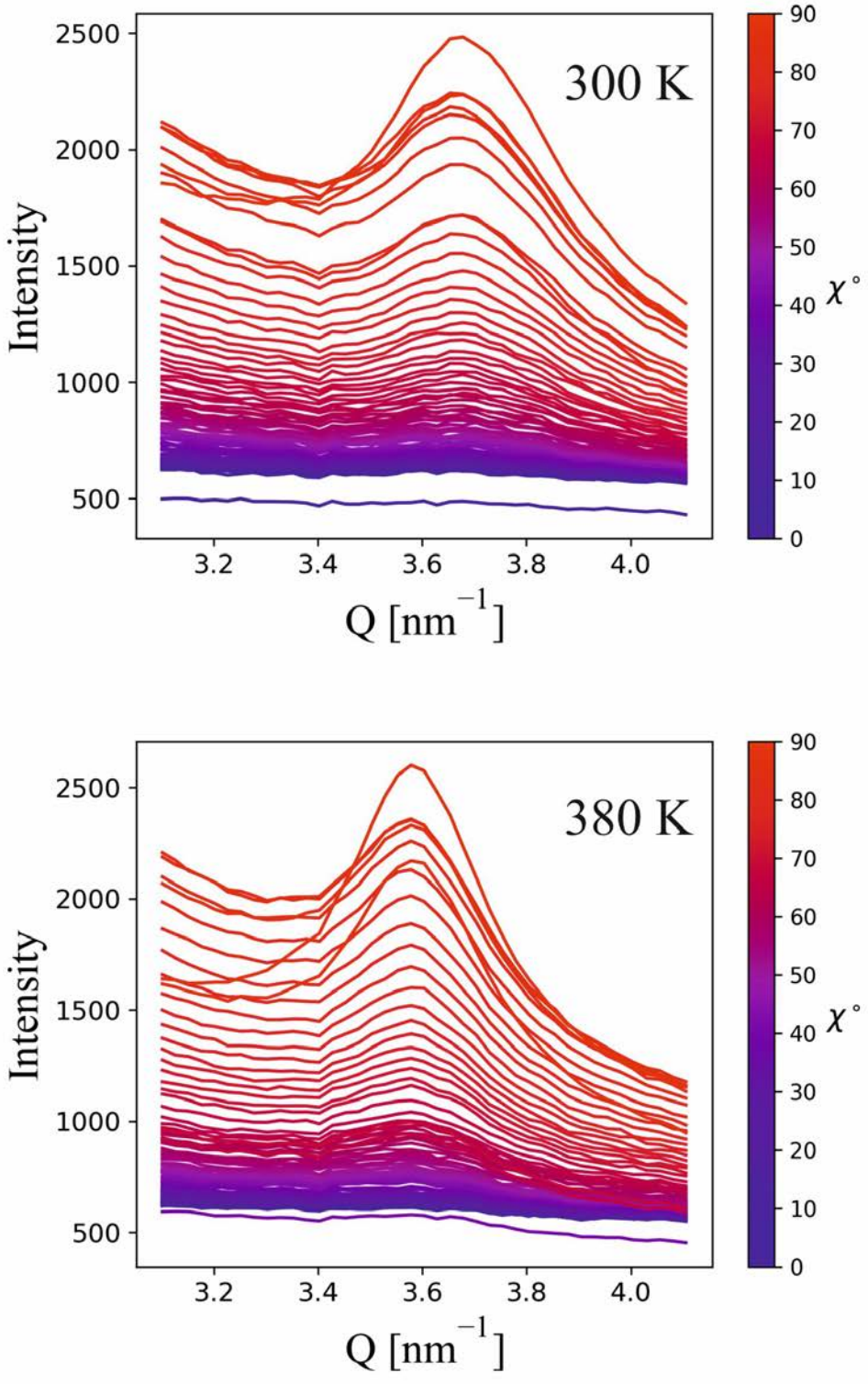


**Figure 7.8:** P3HT (100) peak of the undoped hybrid at 300 K and 380 K.

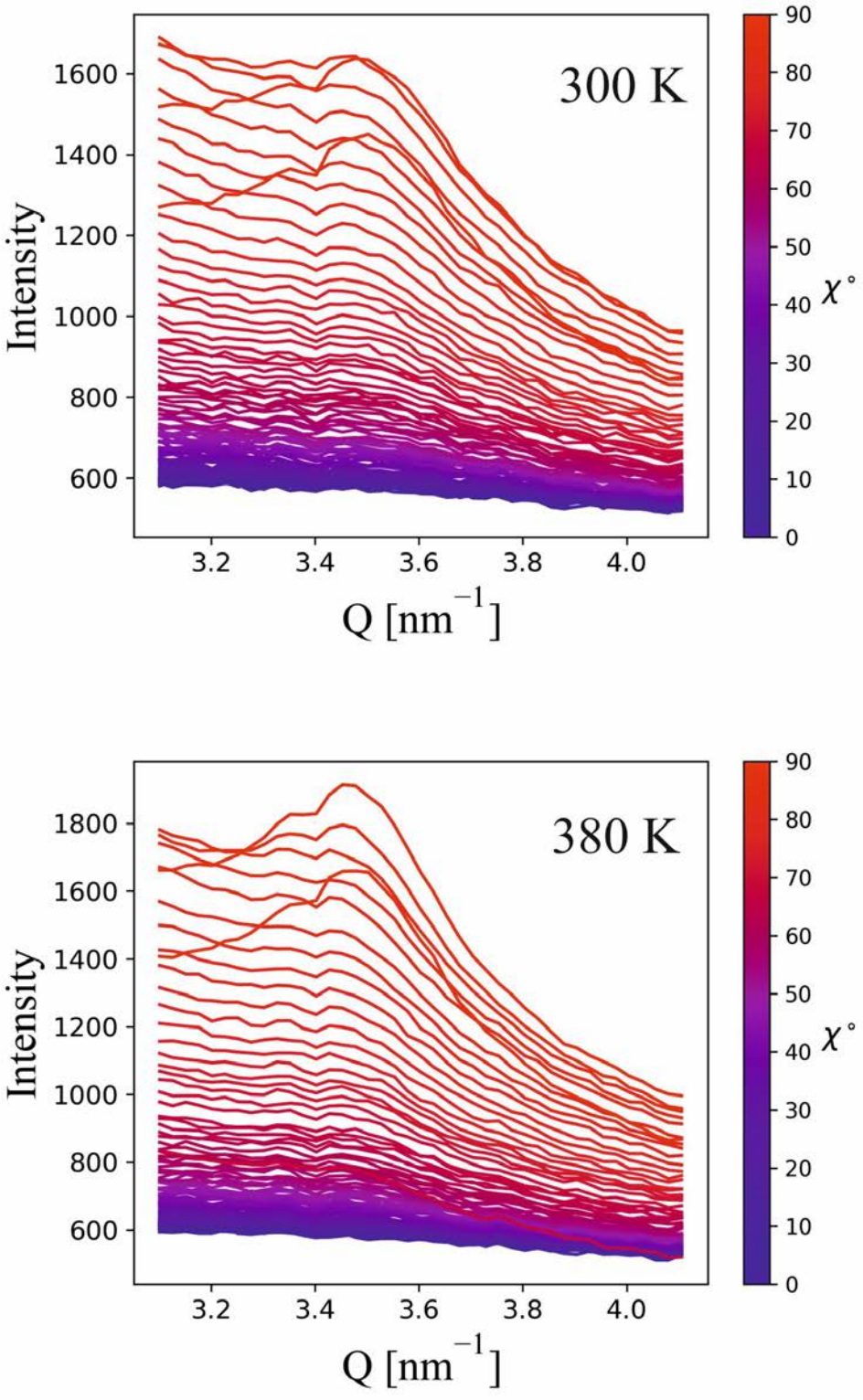


**Figure 7.9:** P3HT (100) peak of the $FeCl_3$-doped hybrid at 300 K and 380 K.

# Chapter 8

# Characterization of transport phenomena

## 8.1 Heat capacity

Heat capacity is a physical property of a material which describes how much heat is required to change its temperature by a certain amount [120]. Its relation to the internal energy comes from the first law of thermodynamics, $dQ = dU + pdV$, where $dQ$ is the amount of heat added to the system, $dU$ is the change in the internal energy and $dW = -pdV$ is the work performed on the system. At fixed volume $dV = 0$ one gets the heat capacity at constant volume $C_V$ as the derivative of the internal energy with respect to the temperature [120, 119]

$$C_V = \left(\frac{\partial U}{\partial T}\right)_V . \tag{8.1}$$

In the harmonic approximation $C_V$ and $C_P$ have similar values [120]. It is an important remark, since the heat capacity measurement at constant pressure ($C_P$) is experimentally accessible and can be easily measured with a PPMS system [154] in contrast to a constant volume measurement.
At high temperatures, the heat capacity reaches a constant value of $C_V = 3\ Nk_B$ which is known as Dulong-Petit limit with $N$ as the total number of atoms in a sample. One derives the Dulong-Petit limit directly by assigning an average energy $1/2k_BT$ to any contribution to the total energy of the system. For a system with 3N degrees of freedom, there are 3N potential and 3N kinetic terms. At elevated temperatures this law is a fairly good approximation of $C_V$, at low temperatures the heat capacity becomes temperature dependent [120, 119].
Einstein [155] considered each atom as an independent quantum harmonic oscillator with the same frequency $\omega_E$ and used the Bose-Einstein distribution to derive the total energy

$$\langle U \rangle = 3N\hbar\omega_E \left(\frac{1}{2} + \frac{1}{e^{\hbar\omega_E/k_BT} - 1}\right). \tag{8.2}$$

With $T_E = \hbar\omega_E/k_B$ as the Einstein temperature, the heat capacity is

$$C_V = \frac{\partial\langle U\rangle}{\partial T} = 3Nk_B \left(\frac{T_E}{T}\right)^2 \frac{e^{T_E/T}}{(e^{T_E/T} - 1)^2}. \tag{8.3}$$

$T_E$ is the characteristic temperature below which thermal excitations of the harmonic oscillators start to freeze-out and $C_V$ decreases. Einstein's model underestimates the low-temperature heat capacities in most cases since dispersive acoustic phonons are relevant at these temperatures [119].
Peter Debye used the continuum limit of the phonon dispersion $\omega = qv_s$, that are sound waves with velocity $v_s$, to predict the heat capacity of solids [120, 119]

$$C_V = 9Nk_B \left(\frac{T}{T_D}\right)^3 \int_0^{T_D/T} \frac{x^4 e^x}{(e^x - 1)^2} dx \tag{8.4}$$

with the substitution of $x = \frac{\hbar\omega}{k_B T}$ and the so-called Debye temperature $T_D = \frac{\hbar\omega_D}{k_B}$ with $\omega_D$ as the Debye cut-off frequency [119]. This calculation uses the energy density of states that depends on $\omega^2$. It predicts the $C_V$ at low T very well where the $T^3$ dependence is valid. The model may fail at moderate temperatures, but like the Einstein model it reaches the Dulong-Petit limit at high T.
Specific heat capacity $c$ is the heat capacity divided by the mass of the sample.

### 8.1.1 Debye-Einstein model for bulk silicon

The specific heat capacity of bulk silicon and mesoporous silicon was measured in the temperature range from 1.8 K - 300 K using the PPMS device. The measured parameter is $c$ at constant pressure, which as mentioned in Sec. 8.1 is measurable and has a similar value as the specific heat capacity at constant volume.
A combination of Debye and Einstein models was used to analyze the data. Complementary weighting by factors $\alpha$ and $1 - \alpha$ guarantees the Dulong-Petit limit at high T

$$c_V = \alpha c_V^{Debye} + (1 - \alpha) c_V^{Einstein}. \tag{8.5}$$

The weighting factors define the contribution from each model: $\alpha$ for the Debye model and $1 - \alpha$ for the Einstein model.
This combined model works well describing the specific heat capacity of bulk crystalline silicon (Fig. 8.1). The fitting for bSi resulted in the Debye temperature of $T_D = 598\ K$ and Einstein temperature $T_E = 177.8$ K with the weighting factor $\alpha = 0.88$. The found $T_D$ value is close to the literature value of $T_D = 645$ K [156]. Including the Einstein model in Eq. 8.1 is necessary, since the Debye model does not correctly describe the behavior at moderate temperatures [157]. An excess $c_P$ in this range is caused by a flat TA branch in the phonon dispersion curve [158]. This flattening is characteristic for silicon [158] and is better modeled with Einstein's theory.

### 8.1.2 Porous silicon heat capacity

The specific heat capacity data obtained for both bSi and pSi samples are plotted in Fig. 8.2. Both samples display similar values of specific heat over the entire temperature range, with room temperature values around 0.7 $J/gK$. But differences between $c_P$ for bSi and pSi can be seen by looking closely at the temperatures from 5 K - 100 K in the inset plot. The difference in $c_P$ in this region may have various causes. Size-dependent effects on heat capacity have been

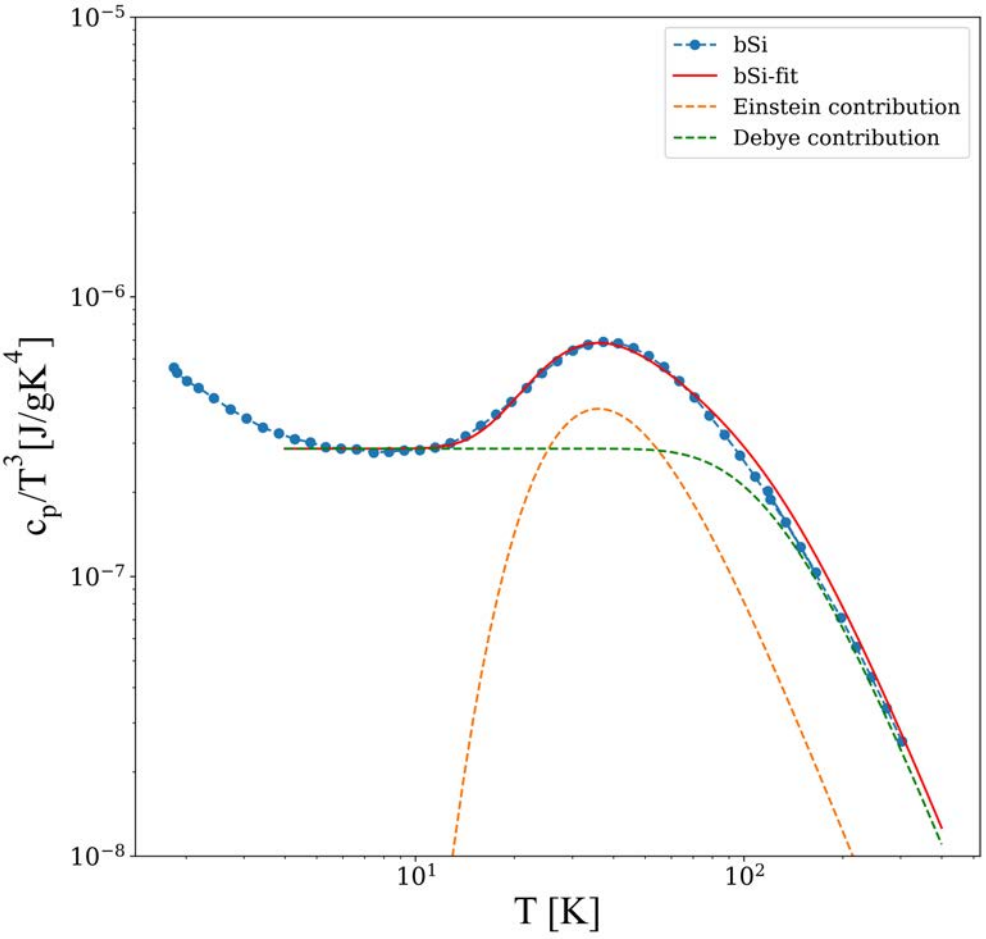


**Figure 8.1:** Specific heat data for bulk silicon fitted with the combined Debye and Einstein model.

reported for metallic nanoclusters and nanodielectrics [159, 160]. A reduced Debye temperature was reported in amorphous silicon with lowered heat capacity compared to bulk crystalline silicon [158]. Since the phonon dispersion in mesoporous silicon is not altered by nanostructuring compared to bulk silicon [161], the excess specific heat capacity arises from another factor.

At very low temperatures $T < 5K$, $c_P$ of bulk silicon follows a $T^3$ dependence, typical for crystalline solids, where the density of states varies with $\omega^2$. For mesoporous silicon, this power law is different and the heat capacity $c_P$ decreases with $T^{2.89}$. This observation necessitates including additional contributions when modeling the $c_P$ of pSi.

To better understand the excess heat capacity in pSi at low temperatures, the data are fitted with a modified Debye-Einstein model. This model accounts for additional contributions to $c_p$ [162]. The combination of bulk-like, three dimensional Debye and Einstein terms with two dimensional ones that represents in our model surface contributions writes as

$$c_V = (\beta\alpha c_V^{Debye} + \beta(1-\alpha)c_V^{Einstein} + \\ + \alpha_S c_V^{Debye-surface} + (1-\beta-\alpha_S)c_V^{Einstein-surface}). \tag{8.6}$$

$c_V^{Debye-surface}$ and $c_V^{Einstein-surface}$ are the Debye and Einstein surface heat capacities with obvious definitions of $T_D^S$ and $T_E^S$. $\alpha_s$ and $\beta$ are additional scaling factors, again to guarantee the Dulong-Petit limit at high T.

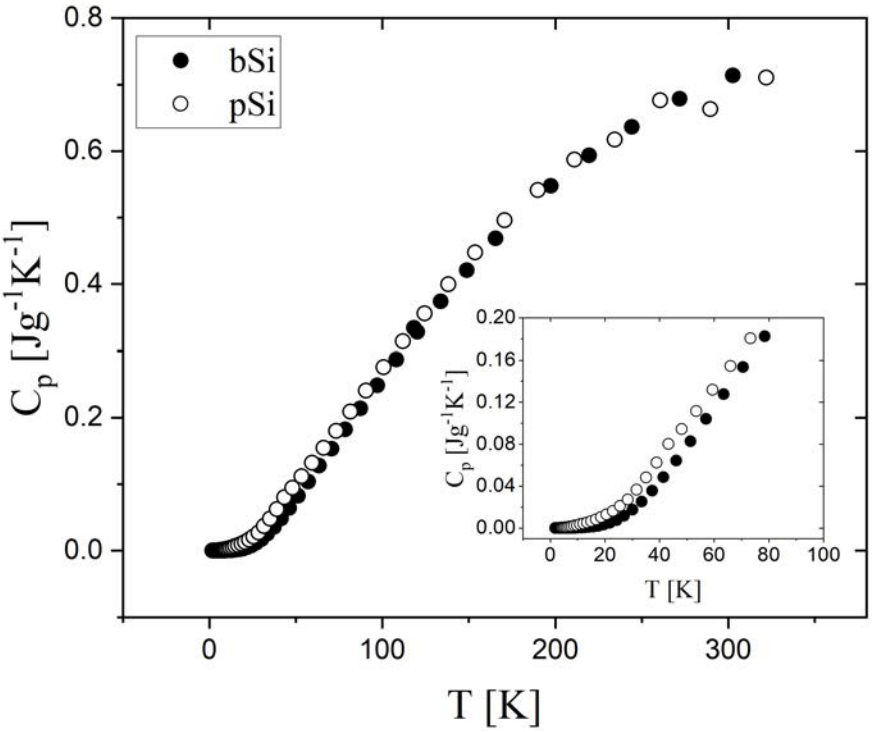


**Figure 8.2:** Specific heat data for bulk silicon (filled symbols) and mesoporous silicon (empty symbols).

We assume a bulk-like contribution to the specific heat of pSi. This assumption allows to use $\alpha$, $T_D$ and $T_E$ from 8.1.1 in Eq. 8.6. The excess of heat capacity at low temperatures in pSi comes in our model from the contribution of surface states. In case of mesoporous silicon, the specific surface area is significantly larger than for bulk silicon, which motivates the addition of surface terms.
The calculated Einstein and Debye temperatures of the surface contribution and weighting factors are listed in Tab. 8.1. The fit of pSi data to the model is shown in Fig. 8.3, together with the model's contributions.
The additional Einstein mode-like contribution to $c_p$ becomes evident as "anomaly" in a $c_P(T)/T^3$ plot, where a characteristic feature occurs at very low temperature $T \sim 10K$ (Fig. 8.3). This feature is well known in the low temperature heat capacity of amorphous as well as of disordered materials and is referred to as a "boson peak". Its origin is still a matter of debate [163]. Benassi et al. [164] discuss its origin in terms of sound modes while Vacher et al. [165] argue that there is a crossover to strong scattering of acoustic modes in disordered materials. Explanations based on vibrational excitations and elastic mode propagation with

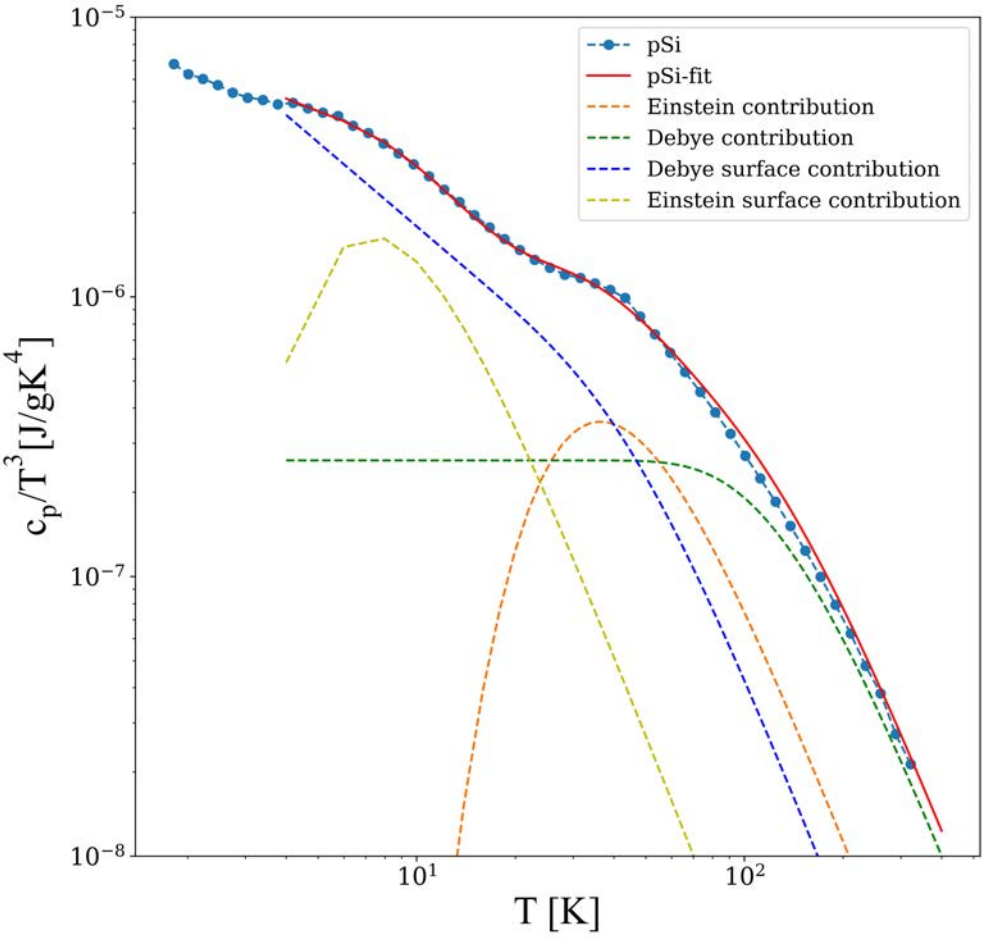


**Figure 8.3:** Modeled specific heat capacity data of porous silicon.

**Table 8.1:** Fitting parameters for mesoporous silicon heat capacity.

| Parameter | Value |
|---|---|
| $T_D$ | 598.7 |
| $T_E$ | 179.4 |
| $T_D^S$ | $200.5 \pm 18.1$ K |
| $T_E^S$ | $35.7 \pm 0.4$ K |
| $\alpha$ | 0.882 |
| $\alpha_S$ | $0.083 \pm 0.012$ |
| $\beta$ | $0.92 \pm 0.015$ |

diffusive damping [166] were also proposed. Recently, Hu et al. [163] relate in their numerical study the boson peak to quasi-localized vibrations of string-like dynamical defects.

The boson peak was previously reported in disordered $SiO_2$ at around 10 K [167, 168]. The feature is not visible in the bulk silicon data, which follows Debye's theory for crystals. The contribution to the boson peak in pSi is possibly linked

with the native $SiO_2$ layer covering the pore walls after etching or a highly disordered surface.
The vibrational states, responsible for the boson peak, are also believed to cause the plateau in thermal conductivity for glassy materials [163]. Although we observe the distinct peak in $c_P(T)/T^3$ vs. $ln(T)$ plot, the aforementioned plateau is not present in the thermal conductivity plot (Fig. 8.4). The lack of a plateau may be due to the fact that the main contribution to the heat capacity of porous silicon comes from a bulk like part.
In pSi, $\kappa$ is not isotropic and PPMS measures the in-plane thermal conductivity of a material with structural anisotropy. The room-temperature thermal conductivity measured with PPMS differs by an order of magnitude when compared with the cross-plane one measured with the LFA method (Sec. 8.4.2). The in-plane measurement results also in a different T-dependence. The typical $T^3$ at low T is not preserved as a $T^1$ dependence is valid over a wide temperature range. The linear dependence was previously reported in amorphous materials, where it was discussed as a consequence of interaction between localized low-T modes and phonons [169, 170].

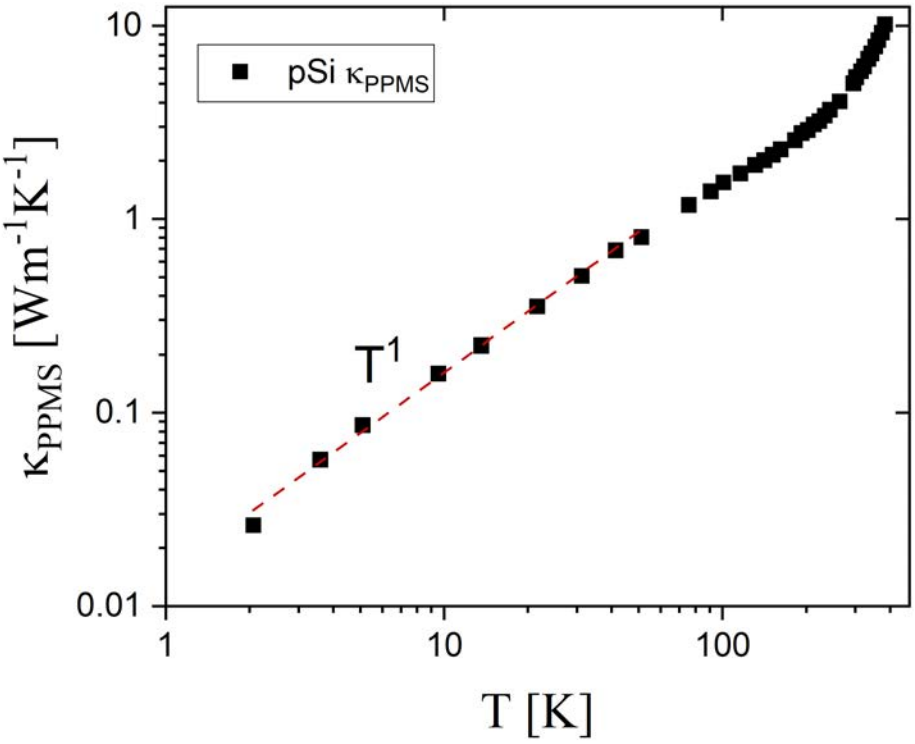


**Figure 8.4:** In-plane thermal conductivity of mesoporous silicon measured with PPMS.

## 8.2 Electrical transport in porous silicon

Electrical conductivity measurements on bulk and porous silicon were performed in the temperature range between $T = 300\,\mathrm{K}$ and $T = 770\,\mathrm{K}$. The electrical conductivity of bulk silicon at room temperature used as the source material for pSi is in the range from $100\,\Omega^{-1}\,\mathrm{cm}^{-1}$ to $50\,\Omega^{-1}\,\mathrm{cm}^{-1}$. The electrical conductivity of bSi (Fig. 8.5) shows the T-dependence expected for highly doped semiconductors and decreases from $62\,\Omega^{-1}\,\mathrm{cm}^{-1}$ to $32\,\Omega^{-1}\,\mathrm{cm}^{-1}$ in this temperature range. $\sigma$ decreases with temperature as the charge carrier mobility decreases, caused by the scattering by phonons [119].

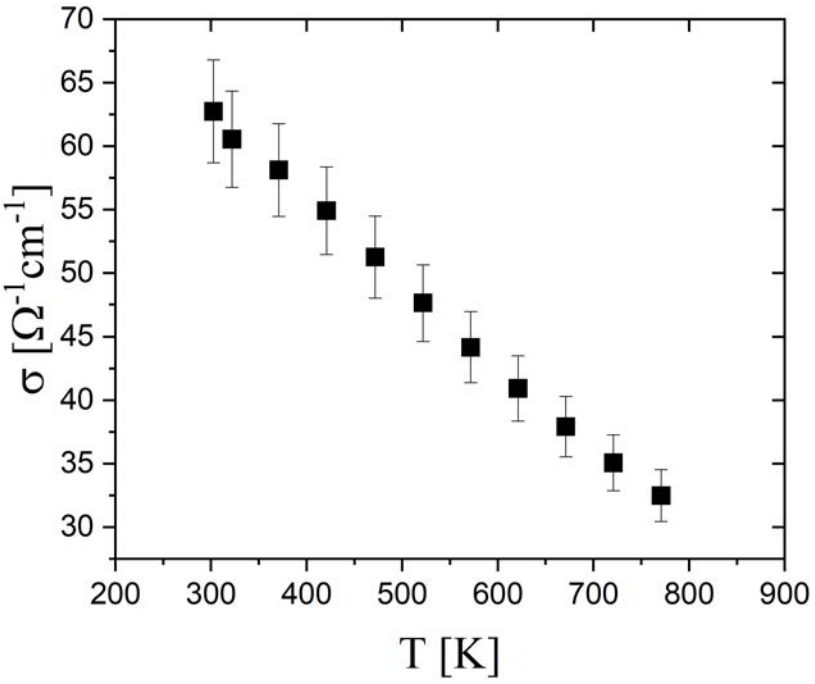


**Figure 8.5:** Electrical conductivity dependence on temperature for bulk silicon.

The electrical conductivity of porous silicon decreases significantly upon porosification. One obvious reason for the drastic drop in $\sigma$ is the disorder introduced via porosification which results in strong scattering of charge carriers at the boundaries. The porosification also changes the T-dependence of $\sigma(T)$. The charge transport is thermally activated and the conductivity depends exponentially on the inverse temperature T as evident in the Arrhenius plot (Fig. 8.6). The values of $\sigma$ drop several orders of magnitude and below 400 K the conductivity is even below the resolution limit of the used device that is $\sigma = 0.05\,\Omega^{-1}\,\mathrm{cm}^{-1}$. To approximate the room temperature value, a low temperature extrapolation is shown in Fig. 8.6. Assuming a thermally activated behavior, the room temperature conductivity is $\sigma(T = 300\,\mathrm{K}) = 10^{-4}\,\Omega^{-1}\,\mathrm{cm}^{-1}$. The obtained value is in a good agreement with studies by Lee et al. [171], where porous silicon with similar porosity shows an electrical conductivity between $10^{-4}\,\Omega^{-1}\,\mathrm{cm}^{-1}$ and $10^{-3}\,\Omega^{-1}\,\mathrm{cm}^{-1}$ in the temperature range from $T = 300\,\mathrm{K}$ to $T = 370\,\mathrm{K}$.
UV-Vis absorption spectra were collected for as-etched porous silicon samples. Optical band-gaps were extracted from the measured spectra (Fig. 8.7) using

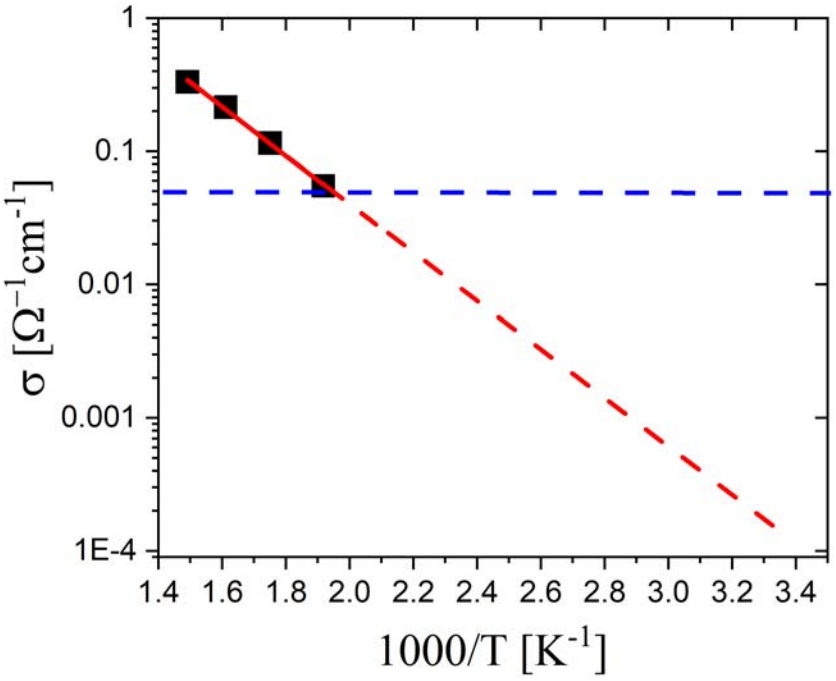


**Figure 8.6:** Temperature-dependent electrical conductivity of pSi: the red dashed line is extrapolated from measurement data at high temperature (square symbols). The blue horizontal line indicates the sensitivity limit of the device. Published in (P.2).

Tauc plots (see Sec. 5.2.4). Although silicon is an indirect band-gap semiconductor [137], direct transitions were found in porous silicon. Therefore we use $r = 1/2$ in Eq. 5.17 to estimate the band-gaps.
Upon porosification, the band-gap of nanostructured silicon changes from $E_g^{bSi} = 1.12\,\text{eV}$ [172] to about $E_g^{pSi} = 1.50\,\text{eV}$. The values for various samples are listed in Tab. 8.2. This red shift in the absorption threshold comes from quantum confinement effects in porous silicon. The electron is confined in a quantum well which in the case of porous silicon is the nanometer-sized pore wall. In a simple particle-in-the-box model, the pSi band-gap depends on the size of the box D, in our case the wall thickness:

$$E_g^{pSi} = E_g^{bSi} + \frac{\hbar^2\pi^2}{2D^2}\left(\frac{1}{m_e^*} + \frac{1}{m_h^*}\right). \tag{8.7}$$

$E_g^{bSi}$ is the silicon energy gap, $m_e^* = 1.18m_0$ is the effective mass of the electron, $m_h^* = 0.81m_0$ is the effective mass of the hole in silicon [172] and $m_0 = 9.11 \times 10^{-31}\,\text{kg}$ is the the free electron rest mass.
To better understand the conduction mechanisms that govern electrical transport in pSi, the activation energies of various pSi samples were determined. The thermally activated transport can be expressed with the equation

$$\sigma(T) = \sigma_0\ exp\left(-\frac{E_A^\sigma}{k_B T}\right), \tag{8.8}$$

where $E_A^\sigma$ is a activation energy and $\sigma_0$ is theoretically a high temperature limit

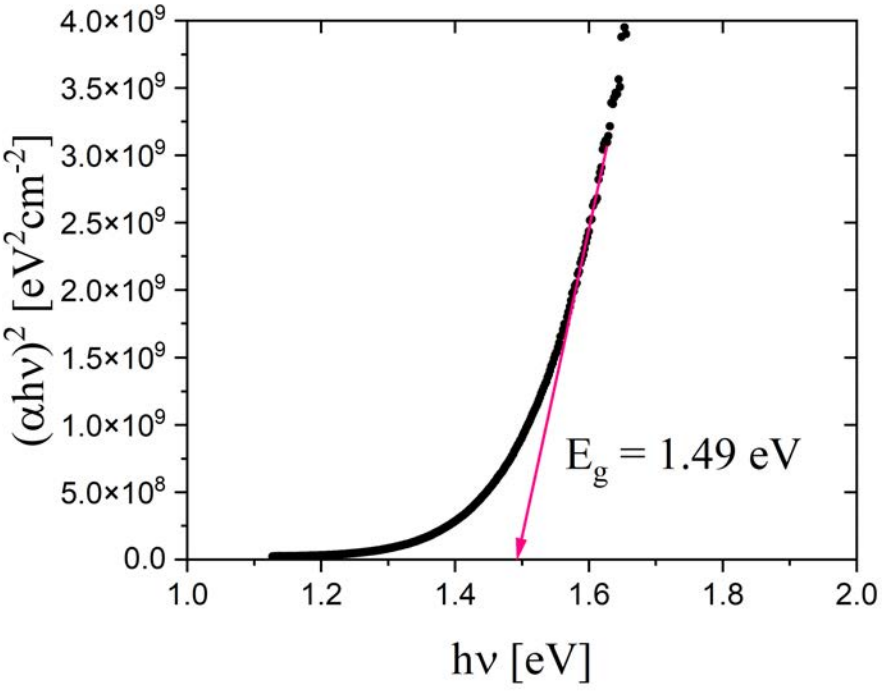


**Figure 8.7:** Tauc plot for extracting the optical band-gap of mesoporous silicon.

**Table 8.2:** Energy band-gaps and pore wall thickness (Eq. 5.17).

| Optical energy gap $E_g^{pSi}$ [eV] | Pore-wall thickness [nm] |
|---|---|
| 1.49 | 4.11 |
| 1.51 | 4.00 |
| 1.48 | 4.17 |
| 1.51 | 4.00 |
| 1.50 | 4.06 |

for the conductivity. A potential T-dependence of $\sigma_0$ is neglected over the dominant exponential term. The activation energy differs from sample to sample and is in the range between 160 meV - 520 meV. Fig. 8.8 presents the Arrhenius plots for various pSi samples that were synthesized under the same conditions. It is distinctive that all the data sets intersect at a common point, which is a demonstration of the Meyer-Neldel compensation rule (MNR) [173]. It is an empirical relation that relates $\sigma_0$ with $E_A^\sigma$ via

$$\sigma_0 = \sigma_{00}\ exp\left(\frac{E_A^\sigma}{E_{MN}}\right). \tag{8.9}$$

$E_{MN}$ is called Meyer-Neldel energy. Fig. 8.9 shows $\sigma_0$ depending on $E_A^\sigma$. A least-squares approximation provides an estimate for $E_{MN} = 54$ meV.
A Meyer-Neldel rule is observed for many thermally activated processes such as diffusion and conduction processes. It was previously observed in porous and amorphous silicon [174, 175].
"The statistical shift" is one theory used to explain the MNR for electrical conductivity. It relates the conductivity to the temperature induced shift of the

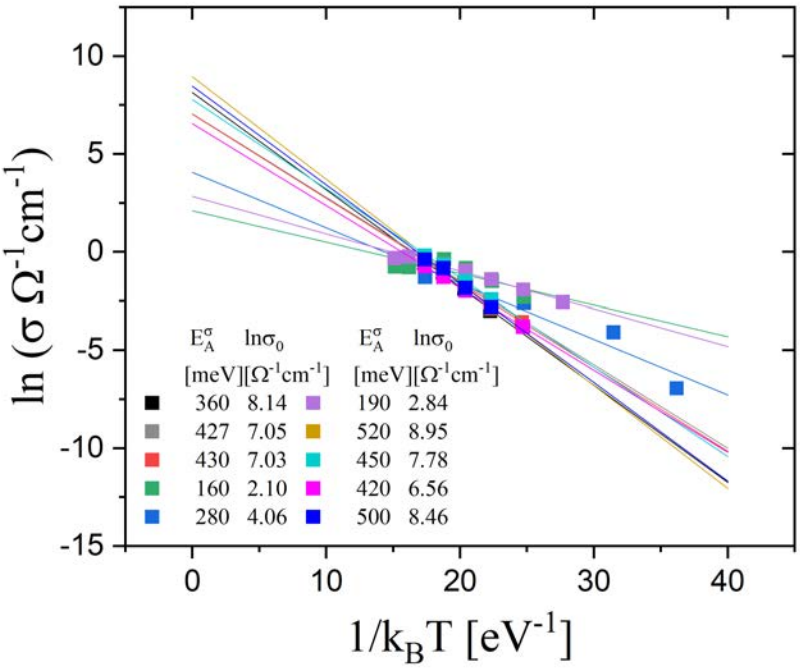


**Figure 8.8:** Temperature-dependent electrical conductivity of pSi samples.

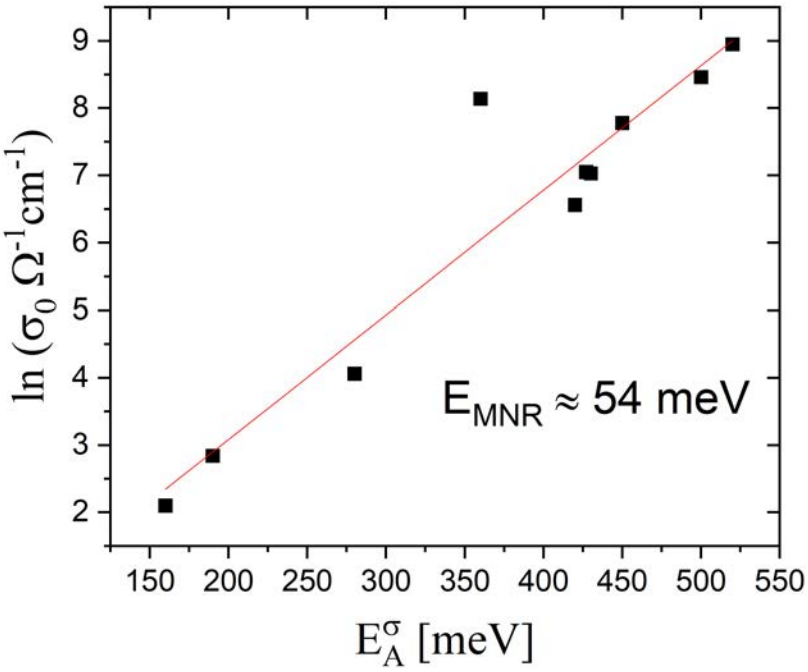


**Figure 8.9:** Meyer-Neldel Rule for porous silicon. Different data points correspond to different samples.

Fermi level if the density of states around $E_F$ is asymmetric [176].
The kinetic model, suggests that the MNR is a result of an interaction between charge carriers and multiple elementary excitations, an interaction that facilitates

charge transport [174]. In this scenario, multiple excitations such as phonons must be absorbed to overcome the activation energy for transport [177]. In this case, the charge transport in pSi would rely on multi-phonon absorption since the activation energy is much larger than the highest phonon energy. In the frame of the kinetic model, the characteristic energy $E_{MN}$ of pSi should be a function of an optical phonon energy [176, 178].
The discussion which of these models (if any) describe the charge transport in pSi best is not finally settled. One notes that $E_{MN} = 54\,\text{meV}$ for pSi is in excellent agreement with a pronounced maximum in the Si phonon density of states at 54 meV and consequently the kinetic model becomes quite appealing. However, one should also state, that the kinetic model in its microscopic variants [179] does not necessarily predict equality between $E_{MN}$ and the characteristic phonon energy $\hbar\omega_0$ rather a proportionality that accounts for the strength of the charge carrier phonon interaction.
Additional insights into the charge transport mechanism might be taken from the temperature-dependent Seebeck coefficient (thermopower) $S(T)$ measurements. The Seebeck coefficient of porous silicon is larger than that of bulk Si. It depends linearly on 1/T. An activation energy $E_A^S$ can be extracted from the linear relation of thermopower and inverse temperature [180]:

$$S(T) = \frac{k_B}{e}\left(\frac{E_A^S}{k_B T} + A\right). \tag{8.10}$$

$A$ contains details of the scattering mechanisms [180].
The sign of the thermopower is a reliable indicator of the charge-carrier type. Fig. 8.10 presents the temperature dependence of $S$ and activation energies extracted in accordance with Eq. 8.10 are listed in the inset. The sign of $S$ confirms the hole transport in pSi. The activation energies $E_A^S$ are between 68 meV and 354 meV. They are noticeably smaller than the activation energy for charge carrier flow $E_A^\sigma$. There are two distinct explanations for this observation.
In a crystal, one expects for the transport in extended states $E_A^S = E_A^\sigma$ [180]. For disordered systems, there are two main ideas to explain the discrepancy in the activation energies. If the transport is phonon assisted through localized states, one claims easily from Eq. 4.20 and 4.27 that the T-dependent phonon population alters the activation energy of $\sigma$ but not $S$. To be more precise the difference $E_A^S - E_A^\sigma$ is the phonon activation energy. This explanation would favor the kinetic model, unfortunately it is not unique.
The difference in the activation energies of conductivity and thermopower can be also attributed to long-ranged potential fluctuations at the mobility edge in disordered systems. Charge flow is characterized by the highest potential barrier $E_A^\sigma$ that carriers must overcome while $E_A^S$ is smaller because electrons only need to come into diffusive equilibrium without current flow [181].
To summarize, our experiments show unambiguously, that in pSi the Meyer Neldel energy of $E_{MN} = 54\,\text{meV}$ agrees well with a maximum in the phonon density of states. Additionally, the measured differences between $E_A^S$ and $E_A^\sigma$ at least do not reject the idea of a multi-phonon assisted charge carrier hopping as underlying transport mechanism in pSi as outlined above. But a few questions remain that go beyond the scope of this experimental study and its appealing results. First, is it possible to develop a theoretical framework that predicts

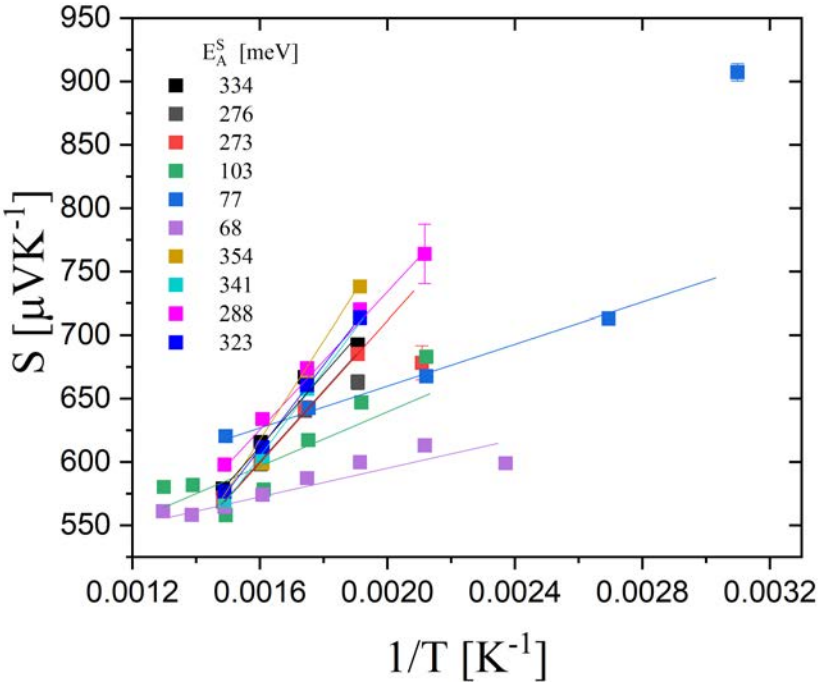


**Figure 8.10:** Seebeck coefficient of various porous silicon samples at different temperatures.

the Meyer Neldel energy $E_{MN}$ to be equal with a particular phonon energy and not only a functional dependence between both? And secondly, can the microscopic origin of the necessarily strong charge carrier phonon interaction in pSi be identified to allow for the envisioned multi-phonon absorption process?

## 8.3 Electrical transport in pSi-P3HT hybrids

### 8.3.1 General transport equations

Charge transport can be described by generalized Boltzmann transport equations, where the electrical conductivity is characterized by the transport function $\sigma_E$:

$$\sigma = \int_{-\infty}^{\infty} \sigma_E \left(-\frac{\partial f}{\partial E}\right) dE. \tag{8.11}$$

$\sigma_E$ describes electrical transport at energy $E$ and temperature $T$. $f$ is the Fermi-Dirac distribution.
The Seebeck coefficient can be expressed as

$$S = \frac{1}{\sigma}\left(\frac{k_B}{e}\right) \int_{-\infty}^{\infty} \left(\frac{E - E_F}{k_B T}\right) \sigma_E \left(-\frac{\partial f}{\partial E}\right) dE \tag{8.12}$$

with chemical potential $E_F$. These expressions for electrical conductivity and thermopower are used to describe isotropic conduction in a band [182].
In metals, only the electrons with energies near the Fermi level contribute to the current flow and the derivative of the Fermi-Dirac distribution can be approximated with the Delta function $\partial f/\partial E \approx -\delta(E - E_F)$. The expression for the electrical conductivity reduces to the Drude formula (Eq. 4.40)

$$\sigma = \frac{e^2 \tau(E_F)}{m^*} n = \sigma_{E_F}. \tag{8.13}$$

The Mott equation for the thermopower of metals is [180]

$$S = \frac{\pi^2}{3}\frac{k^2 T}{3}\left\{\frac{d(ln\sigma)}{dE}\right\}_{E=E_F}. \tag{8.14}$$

The magnitude of the Seebeck coefficient for a metal vanishes at absolute zero and raises with temperature [115]. The absolute thermopower is very small, in the range of $(k_B/|e|)(kT/E_F)$, and depends on the slope of the density of states at the Fermi level $E_F$ [115].
In non-degenerate semiconductors transport occurs away from the Fermi level and the energy difference between conduction band and Fermi level is $E_c - E_F > 3kT$ so the energy term in the integral in Eq. 8.12 is $(E_c - E_F)/k_B T \gg 1$. The derivative of the Fermi-Dirac function in semiconductors is

$$-\frac{\partial f}{\partial E} = \frac{1}{k_B T} exp\left(-\frac{E - E_F}{k_B T}\right). \tag{8.15}$$

$\sigma_E$ contains many expressions related to scattering mechanisms and depends on the density of states. Eq. 8.12 can be rewritten using those expressions and Eq. 8.15 as

$$S = \frac{1}{\sigma}\left(\frac{k_B}{e}\right) \int_{-\infty}^{\infty} \frac{E - E_F}{(k_B T)^2} exp\left(-\frac{E - E_F}{k_B T}\right) \tau(E) v^2(E) N(E) dE, \tag{8.16}$$

where $\tau(E)$ is the relaxation time, $v(E)$ is the carrier velocity and $N(E)$ is the density of states.
These parameters depend on the energy $E - E_C$ with varying power laws. Assuming parabolic bands, the proportionalities are $N(E) \propto (E - E_C)^{1/2}$, $v^2(E) \propto (E - E_C)$ and $\tau(E) \propto (E - E_C)^r$ [119]. The Seebeck coefficient for non-degenerate semiconductor becomes

$$S = \frac{k_B}{e}\left(\frac{E_c - E_F}{k_B T} + \frac{5}{2} + r\right). \tag{8.17}$$

$r$ reveals the dependence of the Seebeck coefficients on dominant scattering mechanisms. One expects $r = -1/2$ for scattering on acoustic phonons. It is $r = +3/2$ for scattering on ionized impurities for weakly screened carriers and $r = -1/2$ for strongly screened ones [119].

### 8.3.2 Transport model

Kang and Snyder developed a model for conducting polymers based on the generalized charge-transport model [183]. They used the generalized Boltzmann equation and used essentially two parameters $E_t$ and $s$ to describe a wide range of conducting polymers.
The Kang-Snyder model postulates a power law for $\sigma_E(E, T)$

$$\begin{aligned} \sigma_E(E,T) &= \sigma_{E_0}(T) \times \left(\frac{E - E_t}{kT}\right)^s \quad \text{for} \quad (E > E_t) \\ &= 0 \text{ for } \quad (E \leq E_t) \end{aligned} \tag{8.18}$$

with $\sigma_{E0}(T)$ as an energy-dependent factor, $E_t$ as a transport edge and parameter $s$. The charge carriers with energy above the transport edge contribute to the charge transport. Below the transport edge, there is no carrier contribution to the conductivity.
$\sigma_E$ includes the density of states, the charge carrier velocity and the scattering time. In crystalline materials, $s$ is related to the scattering mechanisms through $s = r + 3/2$ (see above). Acoustic phonon scattering ($r = -1/2$) and ionized-impurity scattering ($r = 3/2$) correspond to $s = 1$ and $s = 3$, respectively [184]. Porous silicon is a disordered system, where these relations do not necessarily hold.
For polymers a microscopic explanation for particular $s$-values does not exist. They must be considered empirical. Kang and Snyder conclude simply, that the value of $s = 1$ or $s = 3$ basically fits the data best [183].
For the analytical treatment of the model, we express $S$ and $\sigma$ with the help of Fermi-Dirac integrals

$$F(\eta) = \frac{1}{\Gamma(s+1)} \int \frac{\xi^s}{1 + exp(\xi - \eta)} d\xi, \tag{8.19}$$

where the gamma function $\Gamma(n) = (n-1)!$, $n$ an integer and $\eta$ the reduced Fermi energy $\eta = \frac{E_F - E_t}{kT}$. Using the Fermi-Dirac integral and integration-by-parts, one writes

$$S \cdot \sigma = \frac{k_B}{e}\sigma_{E0}(T)\{(s+1)\Gamma(s+1)F_s(\eta) - \eta s\Gamma(s)F_{s-1}(\eta)\} \tag{8.20}$$

and

$$\sigma = \sigma_{E0}(T)s\Gamma(s)F_{s-1}(\eta). \tag{8.21}$$

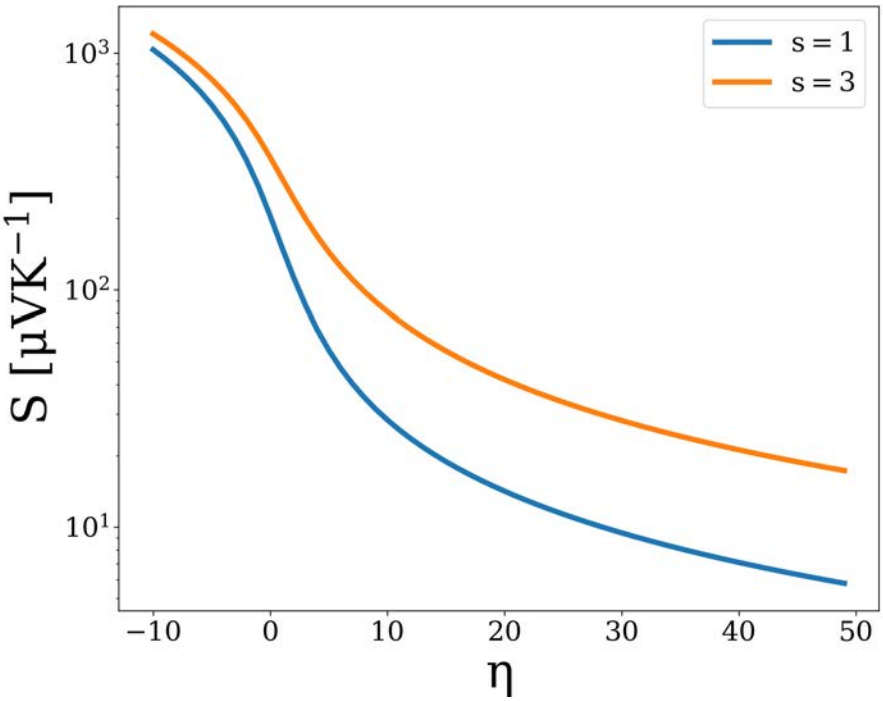


**Figure 8.11:** Thermopower versus $\eta$.

The steps to fit the data with the Kang-Snyder model include finding the reduced Fermi energy $\eta = \frac{E_F - E_t}{kT}$ for given $s$. The Seebeck coefficient only depends on $\eta$ (Fig. 8.11). At high doping level a small variation in $S$ results in a large change in $\eta$. With these equations, using $S(\eta)$, the data $S(\sigma)$ at fixed T can be fitted for both $s = 1$ and $s = 3$ and values for the transport coefficient $\sigma_{E0}$ can be extracted.

The Kang-Snyder model was used to describe P3HT and PEDOT transport data [183, 185]. P3HT usually follows the $s = 3$ fit, which is attributed to inhomogeneous disorder [183]. It shows the T-dependence of thermally activated conductivity above $E_t$. Transport via delocalized states may emerge at elevated doping levels of P3HT, which is then modeled with $s = 1$, but the transport is still temperature-activated [89]. Different $FeCl_3$-doped polythiophene derivatives were also modeled with the Kang-Snyder approach and showed $s = 1$ behavior [186]. The PEDOT data fit better with $s = 1$ which is believed to be favorable for the thermoelectric application [183, 89].

### 8.3.3 Data analysis

Variable-range hopping [85, 88], polaronic hopping [187] and mobility edge [188] approaches are commonly used to describe the transport mechanisms in semiconducting polymers. Typically, P3HT shows thermally activated conduction but metal-like transport can occur at elevated doping levels.
Electrical conductivity measurements on P3HT-pSi hybrids were performed in the temperature range between $T = 300\,\mathrm{K}$ and $T = 370\,\mathrm{K}$. Compared with the low temperature extrapolation, the conductivity of the hybrids is remarkably increased by five orders of magnitude compared to pSi (Fig. 8.12). It is $\sigma(T = 300\,\mathrm{K}) = 13\,\Omega^{-1}\,\mathrm{cm}^{-1}$. Contrary to the thermally activated transport in pSi, the electrical conductivity of hybrids decreases with temperature. This contrast resembles the situation encountered in undoped vs. doped semiconductors.

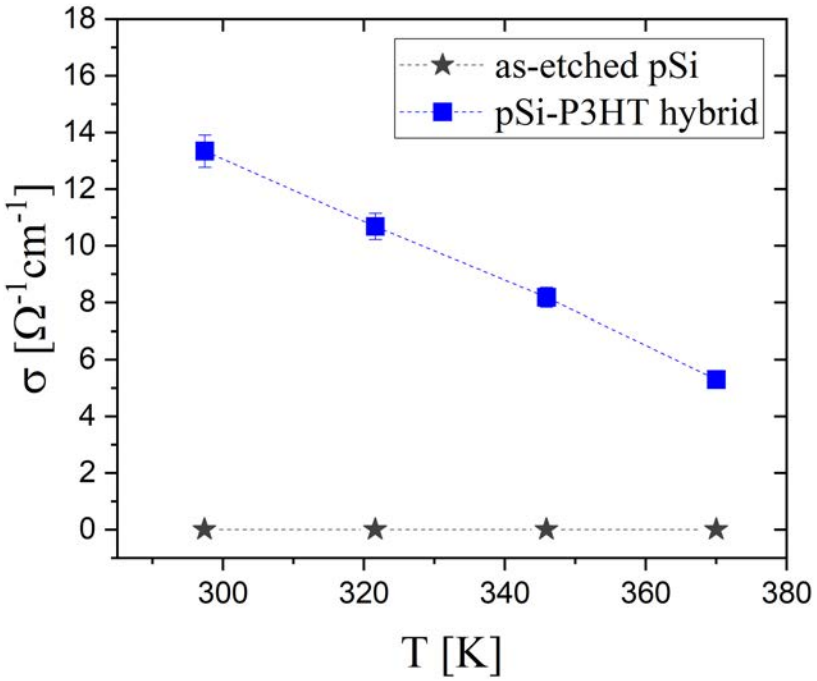


**Figure 8.12:** Electrical conductivity of a representative hybrid. Published in (P.2).

The Seebeck coefficient versus inverse temperature data of a representative hybrid are presented in Fig. 8.13. The values change from about $260\,\mu\mathrm{V\,K}^{-1}$ at $T = 300\,\mathrm{K}$ to $314\,\mu\mathrm{V\,K}^{-1}$ at $T = 370\,\mathrm{K}$. These $S$ values are a factor of 2 or 3 lower than literature data of pSi at room temperature ($630\,\mu\mathrm{V\,K}^{-1}$ to $900\,\mu\mathrm{V\,K}^{-1}$) [189] and the extrapolation value ($1000\,\mu\mathrm{V\,K}^{-1}$, see Tab. 8.3). The S(T) dependence of P3HT-pSi hybrids is in contrast to the pSi thermopower T-dependence. A Seebeck coefficient that decreases with temperature is also known from highly doped polymer films [190].
The room temperature values of $\sigma$ and $S$ of several hybrids are collected in Tab. 8.3. Additionally, the measured values for bulk silicon at $T = 330\,\mathrm{K}$ and porous silicon at $T = 520\,\mathrm{K}$ are presented, together with room-temperature extrapolation of pSi data. Various literature data of $FeCl_3$-doped P3HT and P3HT-

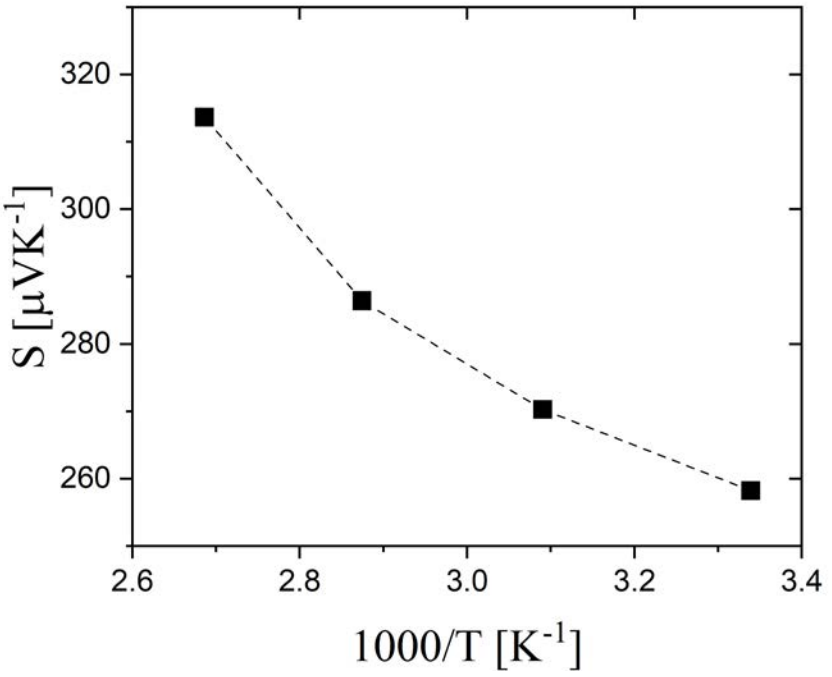


**Figure 8.13:** Seebeck coefficient of a representative hybrid.

inorganic hybrids are also listed. Electrical conductivity and Seebeck coefficient are not significantly different among the six hybrids.

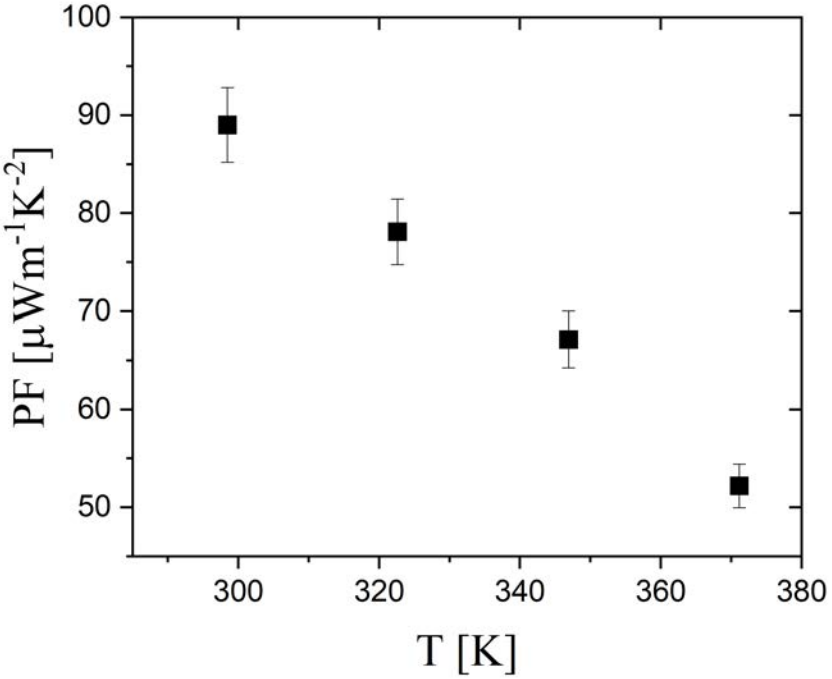


**Figure 8.14:** Power factor of a representative hybrid.

Whereas the $\sigma$ values for hybrids in this work are comparable or lower than

literature values for $FeCl_3$-doped P3HT [89, 90, 91], the $S$ values are significantly higher in case of P3HT-pSi hybrid samples. The power factor falls in the range from $80\,\mu W\,m^{-1}\,K^{-2}$ to $120\,\mu W\,m^{-1}\,K^{-2}$ and is similar to other hybrids utilizing P3HT and inorganic components like CNTs [96]. The power factors in these hybrids exceed those of the polymer film.

**Table 8.3:** Electrical conductivity, Seebeck coefficient and power factor values for hybrids measured at room temperature. The names of the hybrids correspond to the ones from the filling factor studies in Tab. 7.1. Measured data for bulk silicon and porous silicon are included for comparison as well as extrapolated room-temperature pSi values. Literature data on $FeCl_3$-doped P3HT films and other hybrids with P3HT are also included.

| Sample | $\sigma[\Omega^{-1}\,cm^{-1}]$ | $S[\mu V\,K^{-1}]$ | PF $[\mu W\,m^{-1}\,K^{-2}]$ |
|---|---|---|---|
| Hybrid 3 | $13.3 \pm 0.6$ | $258.2 \pm 0.3$ | $89 \pm 3$ |
| Hybrid 4 | $11.5 \pm 0.5$ | $265.8 \pm 0.3$ | $81 \pm 3$ |
| Hybrid 5 | $10.4 \pm 0.5$ | $283.4 \pm 14.2$ | $83 \pm 4$ |
| Hybrid 7 | $17.7 \pm 0.9$ | $263.6 \pm 13.2$ | $122 \pm 6$ |
| Hybrid 8 | $11.1 \pm 0.6$ | $295.9 \pm 14.8$ | $96 \pm 4$ |
| Hybrid 9 | $14.9 \pm 0.6$ | $276.8 \pm 2.3$ | $114 \pm 4$ |
| bSi (at 330 K) | $60.6 \pm 3.8$ | $344.6 \pm 2$ | $718 \pm 45$ |
| pSi (at 520 K) | $0.550 \pm 0.002$ | $698.3 \pm 0.9$ | $27 \pm 2$ |
| pSi (at 300 K) | $10^{-4}$ (*extrap.*) | 1000 (*extrap.*) | 0.01 |
| $FeCl_3$-doped P3HT [89] | 100 | 30 | 9 |
| $FeCl_3$-doped P3HT [89] | 0.1 | 140 | 0.2 |
| $FeCl_3$-doped P3HT [90] | 250 | 37 | 34 |
| $FeCl_3$-doped P3HT [91] | 250 | 40 | 40 |
| P3HT/SWCNT [96] | 1000 | 30 | 90 |
| P3HT/SWCNT [97] | 2760 | 31 | 267 |
| P3HT/SWCNT [98] | 345 | 97 | 325 |
| P3HT/SWCNT [191] | 118 | 44 | 23 |
| P3HT/SWCNT [192] | 550 | 30 | 49 |

In the measured temperature range, the best thermoelectric performance is seen near room-temperature. This T-range is highly requested from the application point of view, as many operation conditions demand a low temperature region. The temperature-dependent power factor is presented in Fig. 8.14. The highest values of PF are achieved at room temperature, more than 300 K lower than for porous silicon.

To better understand the transport mechanism in P3HT-pSi hybrids the electrical transport data $S(\sigma)$ were fitted with the Kang-Snyder model (Fig. 8.15).

The plot presents two models fitted to the room-temperature data of the hybrids listed in Tab. 8.3. For s=1, $\sigma_{E0}$ takes the value of $41.90\,\Omega^{-1}\,cm^{-1}$ and for $s = 3$, $\sigma_{E0} = 0.73\,\Omega^{-1}\,cm^{-1}$. At first glance both models seem to be compatible with the data. The fit covariance reveals that $s = 3$ describes the data significantly better. The question is whether there are additional arguments that favor $s = 3$ over $s = 1$.

First, Kang and Snyder show in [183] that Eq. 8.12 and 8.18 describe the conductivity-Seebeck relation in P3HT very well with $s = 3$. Second, in inorganic materials $s = 3$ can be observed, when charge carriers are scattered on

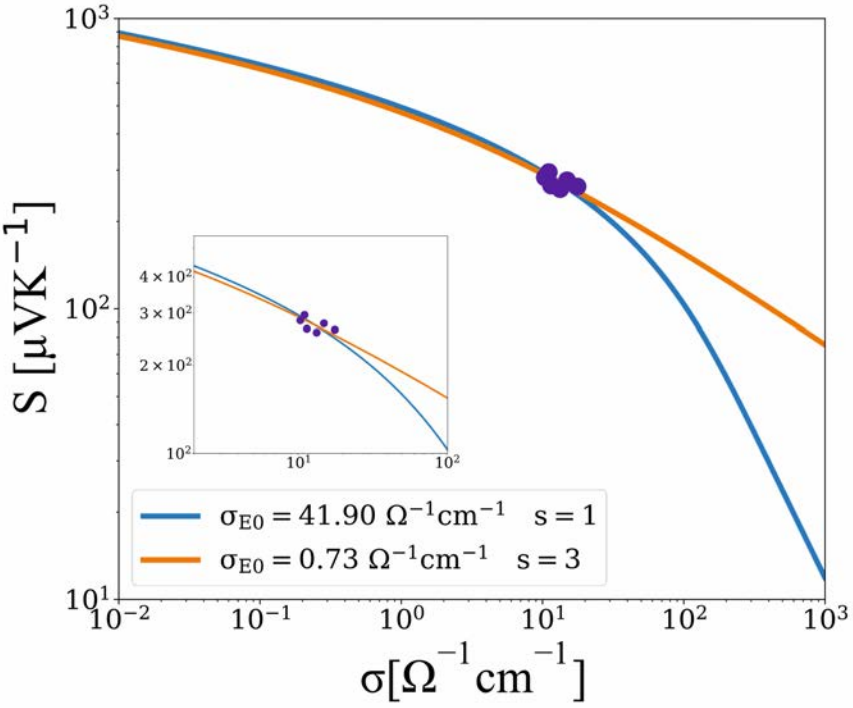


**Figure 8.15:** $S$ versus $\sigma$ plots for hybrids at room temperature. The inset shows a close-up of the data points.

ionized impurities. In disordered, doped P3HT-pSi systems one could argue that ionized impurities dominate carrier scattering, which favors the model with a $s = 3$ power law.

Fig. 8.16 shows data of the hybrid samples at 330 K and 350 K. At 330 K $\sigma_{E0}$ changes to $36.66\,\Omega^{-1}\,\mathrm{cm}^{-1}$ for $s = 1$ and $0.65\,\Omega^{-1}\,\mathrm{cm}^{-1}$ for $s = 3$. At $T = 350$ K $\sigma_{E0}$ is further lowered to $32.36\,\Omega^{-1}\,\mathrm{cm}^{-1}$ and $0.61\,\Omega^{-1}\,\mathrm{cm}^{-1}$ for $s = 1$ and $s = 3$, respectively. These values are not significantly different from those obtained at room temperature, meaning that there is no strong temperature dependence of $\sigma_{E0}$. We conclude that the $s = 3$ model is a better fit than $s = 1$ for all temperatures .

To assess whether there is a particular phase that defines the electrical transport in the P3HT-pSi system, each phase can be considered separately. In general, if the transport mechanism in the organic-inorganic system is dictated by the organic phase, one would expect the energy dependence ($s$-value) similar to that of this organic phase.

In other organic-inorganic hybrid studies, Kumar et al. [153] observed an unchanged transport behavior ($s = 1$) comparing pure PEDOT:PSS and PEDOT:PSS-Te($Cu_x$) hybrid. They also applied the Kang-Snyder model to the literature data of P3HT combined with carbon nanotubes [96] and with $Bi_2Te_3$ [193]. The evaluation showed that these organic-inorganic systems lie on the $s = 3$ curve just like the pure polymer system. They also show very similar $\sigma_{E0}$ values for both the polymer and the hybrid ($0.001 - 0.003\,\Omega^{-1}\,\mathrm{cm}^{-1}$). The energy dependent scattering in hybrid materials is similar to the scattering in pristine polymers and the enhancement of $\sigma_{E0}$ is the key to high performance TE materials [183].

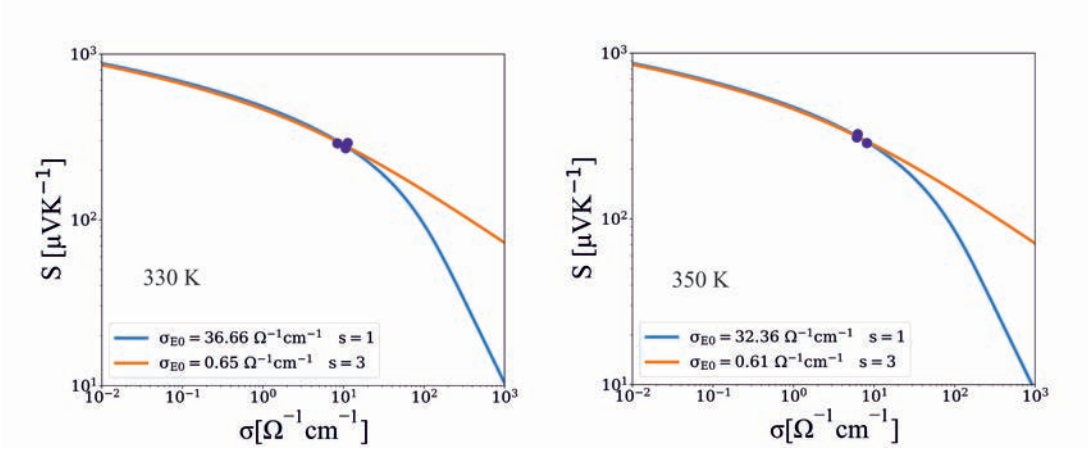


**Figure 8.16:** $S$ versus $\sigma$ plots for hybrids at $T = 330\,\mathrm{K}$ and $T = 350\,\mathrm{K}$.

It is important to note, that in these described composite systems, the organic phase was the main matrix for embedded inorganic "particles".
The energy dependence $\left(\frac{E-E_t}{kT}\right)^s$ on electrical conductivity of P3HT-pSi hybrids and P3HT [183] show the same power law of $s = 3$. To further investigate the transport mechanisms in P3HT-pSi hybrids, the Kang-Snyder model is also used to fit the data of porous silicon. Fig. 8.17 presents fits to the pSi data measured at 523 K. Below this temperature, $\sigma$ values reached the SBA sensitivity limit.

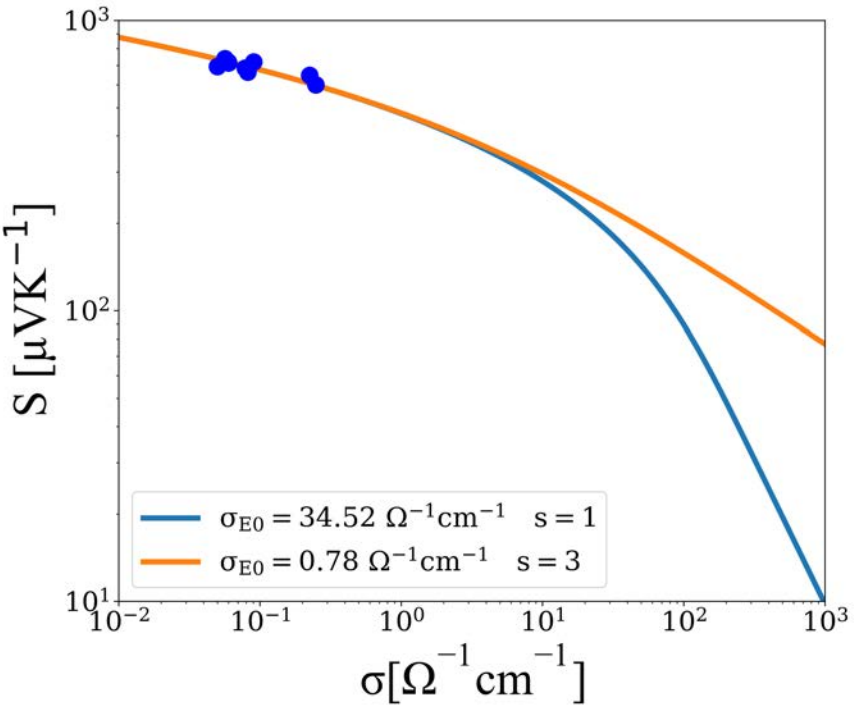


**Figure 8.17:** $S$ versus $\sigma$ plot for pSi samples measured at 523 $K$.

The data show good agreement with both $s = 1$ and $s = 3$ models and it is alike for all temperatures. $\sigma_{E0}$ displays a temperature dependence in the measured T-range. Fig. 8.18 shows the values for the $s = 1$ model between

$28\,\Omega^{-1}\,\mathrm{cm}^{-1}$ - $65\,\Omega^{-1}\,\mathrm{cm}^{-1}$ and $0.6\,\Omega^{-1}\,\mathrm{cm}^{-1}$ - $1.5\,\Omega^{-1}\,\mathrm{cm}^{-1}$ for $s = 3$. Additionally, there is a striking similarity between the $\sigma_{E0}$ values of the hybrids and of the pSi membranes, especially for the P3HT-pSi hybrid and pSi measured at $T = 520\,\mathrm{K}$ as seen in Tab. 8.4.

**Table 8.4:** $\sigma_{E0}$ values for the P3HT-pSi hybrids, the pSi samples and the P3HT [183] for different $s$-values.

| Material | $\sigma_{E0}[\Omega^{-1}\,\mathrm{cm}^{-1}]$ $s = 1$ | $\sigma_{E0}[\Omega^{-1}\,\mathrm{cm}^{-1}]$ $s = 3$ |
|---|---|---|
| P3HT-pSi | 41.90 | 0.73 |
| pSi (at 520 K) | 34.52 | 0.78 |
| $FeCl_3$-doped P3HT [183] | | 0.003 |

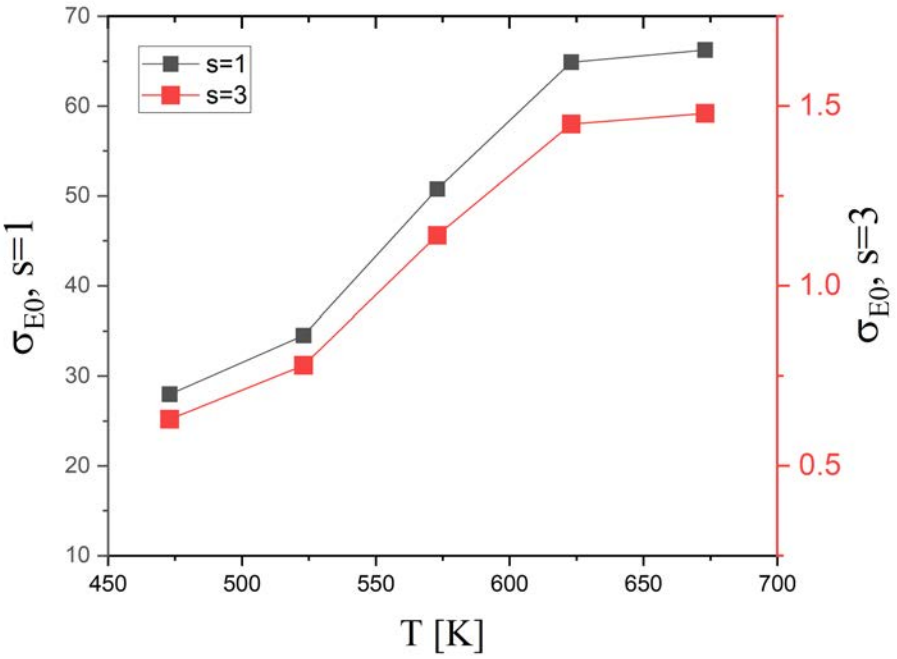


**Figure 8.18:** Temperature dependence of $\sigma_{E0}$ for pSi samples.

The similarity of the $\sigma_{E0}$ of porous silicon and those of the P3HT-pSi hybrids cannot be overlooked. While the $\sigma_{E0}$ values of pristine P3HT ($10^{-3}\,\Omega^{-1}\,\mathrm{cm}^{-1}$) [183] are significantly lower than in pSi ($0.7\,\Omega^{-1}\,\mathrm{cm}^{-1}$ for $s = 3$) the hybrids correspond very well to the values of porous silicon [185].
This observation and the fact that the electrical conductivities differ by five orders of magnitude suggests to view P3HT-pSi merely as a doped version of pSi. Introducing P3HT into pSi seems not to change $s$ or $\sigma_{E0}$ significantly rather it seems to increase the effective Fermi level. This is the very definition of doping. In the highly doped P3HT system, even with transport through delocalized states, the temperature dependence is still Arrhenius-like [89]. The metal-like T-dependence of $\sigma$ in the hybrids also supports the hypothesis that not the organic polymer rather the inorganic pSi phase defines the transport mechanism in the P3HT-pSi hybrids.

Porous silicon is the scaffold of the organic-inorganic system, it creates a matrix of sponge-like connected Si pillars while the P3HT polymer fills the pore space between, with 50% space occupied. In pure P3HT, transport occurs through ordered regions, mixed with amorphous regions that coexist in an inhomogeneously disordered matrix. Transport between ordered domains is limited by these amorphous domains which limits $\sigma_{E0}$ and the conductivity [194, 183]. The pore diameter in pSi is in the range from 8 nm - 10 nm, a distance that is comparable with P3HT crystallites after annealing [195]. Although no specific ordering of P3HT inside the pores was found in scattering studies (see Sec. 7.2.4), the P3HT can still form ordered regions, which can positively affect the charge transfer from polymer to the pSi.
To conclude, the electrical transport data of the P3HT-pSi hybrids show significantly enhanced electrical conductivity compared to the porous silicon. The Seebeck coefficient is lower for the hybrids compared to the pSi but higher when compared to the literature values of $FeCl_3$-doped P3HT films. The power factor of the P3HT-pSi hybrids exceeds that of the empty pSi and the P3HT polymer films (see Tab. 8.3). Analysis of P3HT-pSi hybrid data using the Kang-Snydel model suggests that porous silicon dictates the electrical transport in these organic-inorganic hybrids. Comparison of the $s$-value in energy power-law $\left(\frac{E-E_t}{kT}\right)^s$ and the $\sigma_{E0}$ values (see Tab. 8.4) between the materials, as well as the metallic-like T-dependence of $\sigma$, suggests that P3HT-pSi acts as a doped version of pSi. In this scenario, $FeCl_3$-doped P3HT provides charge carriers to the system which raises the Fermi level.

## 8.4 Thermal transport

Thermal conductivity is an integral part of the characterization of any thermoelectric material. To obtain highly efficient TE materials, thermal transport should be suppressed with ideally minimal impact on electric transport properties.

Nanostructuring techniques affect thermal transport by creating structures on the nanometer-scale that effectively scatter phonons and reduce the phonon contribution to $\kappa$. Porous silicon is an example of such a nanostructured material, in which the thermal conductivity can be reduced by orders of magnitude compared to the bulk. $\kappa$ of porous silicon highly depends on porosity and pore structure [46, 196] and values can be as low as $0.1\,\mathrm{W\,m^{-1}\,K^{-1}}$ [196]. The temperature dependence of $\kappa$ can give valuable insights into the sample's structure and morphology, such as nanostructure or grain size.

### 8.4.1 Bulk silicon

In bulk silicon, heat transport occurs mainly by phonons [46]. It is affected mostly by boundary scattering at low temperatures, impurity scattering at intermediate temperatures and Umklapp phonon-phonon scattering at higher temperatures [197]. The room temperature values of the thermal conductivity in silicon can be as high as $150\,\mathrm{W\,m^{-1}\,K^{-1}}$ [46, 197] and they depend on the doping level. Fig. 8.19 shows the thermal conductivity of $p^+$ doped bulk silicon ($\rho$ = 0.01 - $0.02\,\Omega\,\mathrm{cm}$) measured with the LFA technique in the temperature range $T$ = 300 K - 670 K. The $\kappa$ values decrease continuously from $63\,\mathrm{W\,m^{-1}\,K^{-1}}$, reaching $34\,\mathrm{W\,m^{-1}\,K^{-1}}$ at high temperatures.

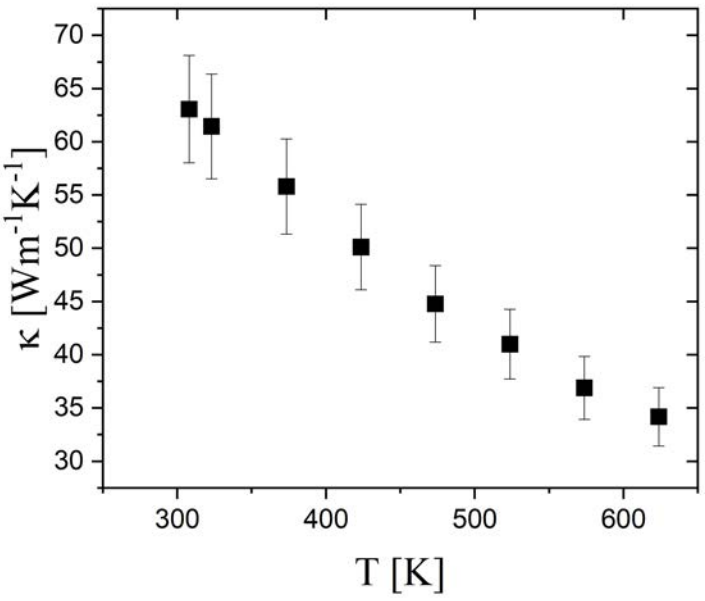


**Figure 8.19:** Temperature-dependent thermal conductivity of $p^+$ silicon.

### 8.4.2 Porous silicon

The data for porous silicon shows a significantly reduced thermal conductivity over the same T-range. Fig. 8.20 and 8.21 present data for several porous silicon samples with similar porosities in the range of 51 % - 65 %. The reduction of $\kappa$ by about two orders of magnitude can be observed for all samples.
The porosification, or more precisely the nanostructuring in pSi, impairs its thermal conductivity. It is apparent that in mesoporous silicon the mean free path of the phonons is in the range of nanostructure size, which for porous silicon is the pore wall thickness. In bulk silicon at near-room temperature, the mean free path is in the micrometer range $\Lambda = 0.3 - 8\,\mu m$ [198, 197] and its thermal conductivity is much higher than in pSi. Phonons with $\Lambda > 1\,\mu m$ contribute to about 40 % of the thermal conductivity [198]. The $\kappa$ reduction in pSi due to a modified phonon dispersion can be ruled out by neutron scattering studies [161]. The elastic properties and therefore phonon group velocity of pSi remain unchained compared to the bulk silicon, so the reduction in thermal conductivity in pSi most likely comes from the reduced phonon mean free path (P.3).

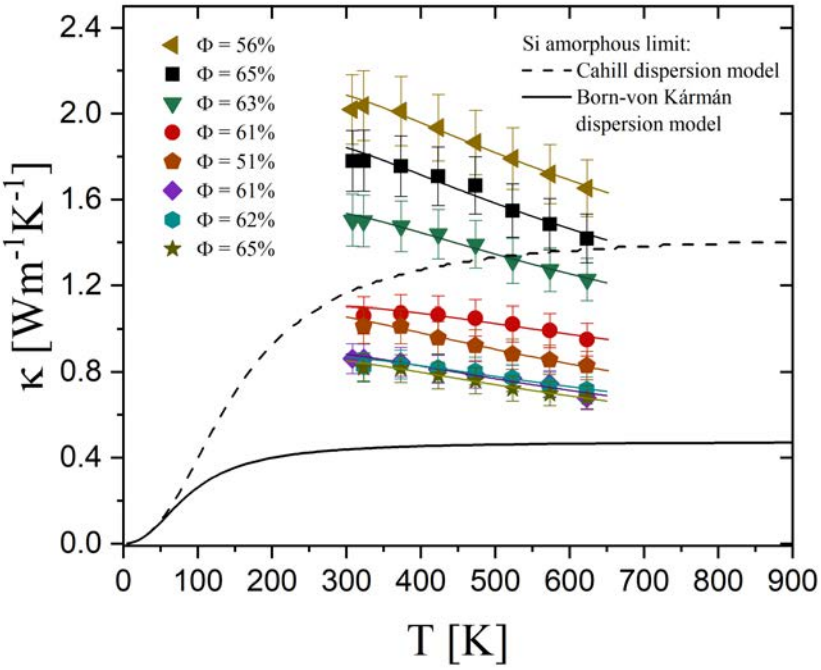


**Figure 8.20:** Thermal conductivity data of the first set of pSi samples. Porosities are displayed in the legend. The amorphous limit for silicon is plotted for comparison. The fits to the Landauer/Lundstrom model are displayed together with the corresponding pSi data.

Together with the measured values for mesoporous silicon, two models for the amorphous limit in silicon are presented. These are the Cahill model and the Born-von Kármán model. The amorphous limit predicts the minimum thermal conductivity for materials. The prediction of the amorphous limit rests on the assumption that the mean free path of a phonon does not exceed half of its wavelength [199]. The Born-von Kármán dispersion model and the Cahill model

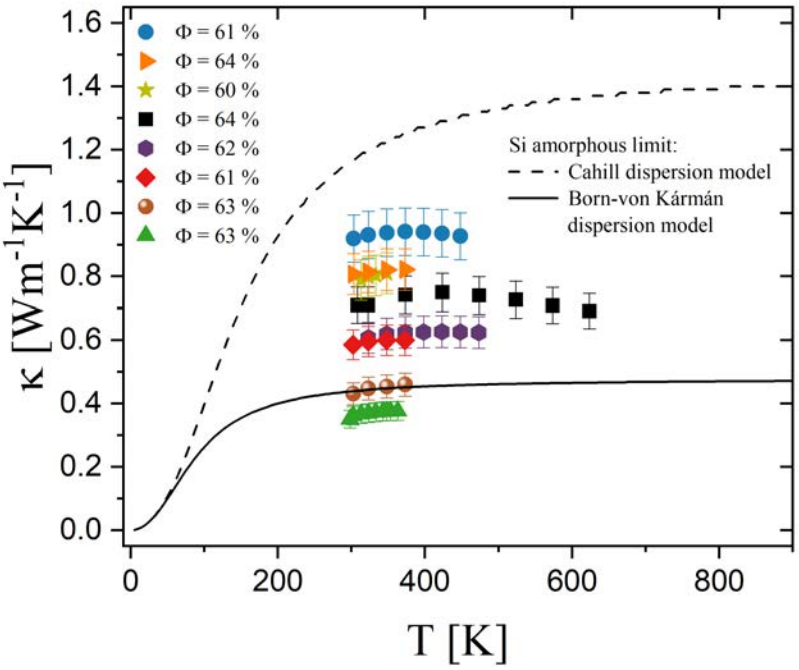


**Figure 8.21:** Thermal conductivity data of the second set of pSi samples. Porosities are displayed in the legend. The amorphous limits for silicon are plotted for comparison.

differ in the approximation of phonon dispersion. Cahill uses the linear Debye dispersion and the Born-von Kármán model uses a sinusoidal dispersion.

The Born-von Kármán model predicts a lower $\kappa_{min}$, as it accounts for an almost vanishing group velocity of phonons near the Brillouin zone boundary, which do not contribute significantly to the thermal conductivity [199].

The variation in $\kappa$ is observed in both data sets. All samples are anodized under the same conditions and show some natural variation in pore size and porosity $\Phi$. The data evidence that this variation does not depend heavily on the $\Phi$ but individual microstructure (mean free path) may result in differences in $\kappa$.

In the following paragraphs, we will discuss a model-based analysis of the data. It will also become clear why the data is grouped in two distinguished plots.

### Modified Landauer/Lundstrom model

To decouple the effects of porosity and mean free path on thermal transport in porous silicon, a modified Landauer/Lundstrom model is applied (P.3). As introduced in Sec. 4.5.1, this model separates the contributions to $\kappa_{eff}$ due to porosity ($\kappa_r$) and phonon scattering ($\kappa_0$).

$$\kappa_{eff} = \kappa_r \kappa_0 = \kappa_r \frac{k_B^2 T_L \pi}{6} \int_0^\infty \frac{4}{3} \Lambda(\omega) M_{ph}(\omega) W_{ph}(\omega) d(\omega) \tag{8.22}$$

The window function $W_{ph}$ in Eq. 8.22 is defined as

$$W_{ph}(\omega) = \frac{3}{\pi^2 k_B T}\left(\frac{\hbar\omega}{k_B T_L}\right)^2 \left(e^{\frac{\hbar\omega}{k_B T_L}} - 1\right)^{-2} e^{\frac{\hbar\omega}{k_B T_L}}. \tag{8.23}$$

The number of modes (conducting channels) is calculated from the phonon density-of-states DOS

$$M_{ph}(\omega) = \frac{\pi}{2} DOS(\omega) v_g(\omega) \tag{8.24}$$

with the phonon group velocity $v_g(\omega)$. The density-of-states is determined with an isotropic sinusoidal dispersion relation

$$\omega = \omega_0 sin\left(\frac{\pi}{2}\frac{q}{q_D}\right). \tag{8.25}$$

$q_D$ is the Debye vector $q_D = \omega_D / v_s$. The Debye frequency $\omega_D$ is

$$\omega_D = v_s \left(6\pi^2 \frac{N}{V}\right)^{1/3} = v_s \left(6\pi^2 \frac{\rho_{Si}}{m_{Si}}\right)^{1/3}, \tag{8.26}$$

where the atomic mass ($28u$) and the density ($2.329\,\mathrm{g/cm^3}$) of silicon are used. The average speed of sound ($v_s$) is calculated with longitudinal and transverse phonon group velocities ($v_l = 8433\,\mathrm{m/s}, v_t = 5433\,\mathrm{m/s}$) of silicon as

$$v_s = \left(\frac{1}{3}\left(\frac{2}{v_t^3} + \frac{1}{v_l^3}\right)\right)^{-1/3}. \tag{8.27}$$

The group velocity is

$$v_g(\omega) = \frac{\partial\omega}{\partial q} = \frac{\pi\omega_0}{2q_D} cos\left(\frac{\pi}{2}\frac{q(\omega)}{q_D}\right), \tag{8.28}$$

where the $\omega_0 = 2v_s q_D/\pi = 2\omega_D/\pi$ is the frequency at the zone boundary, which can be determined from the long wavelength limit ($q \to 0$) in Eq. 8.25. The density of states is

$$DOS(\omega) = \left(\frac{3}{2\pi^2}\frac{q^2(\omega)}{v_g(\omega)}\right). \tag{8.29}$$

Finally, the phonon mean free path is determined ($\Lambda(\omega) = v_g(\omega)\tau_{tot}$) using the scattering times for individual scattering mechanisms and Matthiessen's rule

$$\tau = \left(\tau_{imp}^{-1} + \tau_{boundary}^{-1} + \tau_{umklapp}^{-1} + \tau_D^{-1}\right). \tag{8.30}$$

The scattering rates are defined as $\tau_{imp}^{-1} = D\omega^4$, $\tau_{boundary}^{-1} = v_g(\omega)/(Fl)$ and $\tau_{umklapp}^{-1} = B\omega^2 T_L e^{-C/T}$ [200]. A parameter $\Lambda_D = v_g(\omega)\tau_D$ describes the scattering length due to nanostructures.

The values of $B, C, D$ and $F \cdot l$ are initially fitted using reference data of silicon [201, 202]. The parameters for impurity, Umklapp and boundary scattering are determined and fixed for the analysis of pSi. The parameters are: $B = 2.12 \times 10^{-19}\,\mathrm{s/K}$, Debye temperature $C = 152\,\mathrm{K}$, $D = 1.3 \times 10^{-45}\,\mathrm{s^3}$, parameter $F \cdot l = 6.96\,\mathrm{nm}$. For pSi, $\Lambda_D$ is fitted together with $\kappa_r$.

Eight samples were modeled using the modified Landauer-Lundstrom approach. The fits of the temperature-dependent $\kappa_{eff}$ data are displayed in the Fig. 8.20.

The fit parameters are displayed in Tab. 8.5. $\kappa_r$ that accounts for porosity is below 0.2, which denotes the strong effect of porosity on $\kappa$. The modeled nanostructure sizes are in the range between 8 nm and 16 nm which is a reasonable range of pore-wall thickness in pSi with porosities of about 60%.

**Table 8.5:** Scaling factor $\kappa_r$, intrinsic thermal conductivity $\kappa_0$ at $\sim$ 300 K, nanostructure size $d$ and porosity of eight samples modeled with modified Landauer/Lundstrom model.

| Sample | $\kappa_r$ | $\kappa_0$ [$\mathrm{W\,m^{-1}\,K^{-1}}$] | $d$ [nm] | Porosity |
|---|---|---|---|---|
| 1 | $0.121 \pm 0.012$ | $14.71 \pm 0.96$ | $16.0 \pm 2.47$ | 65% |
| 3 | $0.136 \pm 0.016$ | $7.80 \pm 0.96$ | $7.2 \pm 1.14$ | 61% |
| 3 | $0.116 \pm 0.007$ | $12.96 \pm 0.64$ | $13.2 \pm 1.21$ | 63% |
| 4 | $0.064 \pm 0.008$ | $13.51 \pm 1.96$ | $14.1 \pm 2.57$ | 61% |
| 5 | $0.152 \pm 0.007$ | $5.42 \pm 0.36$ | $13.3 \pm 0.46$ | 56% |
| 6 | $0.078 \pm 0.006$ | $10.57 \pm 1.07$ | $10.6 \pm 1.21$ | 52% |
| 7 | $0.061 \pm 0.003$ | $13.36 \pm 0.91$ | $14.2 \pm 1.14$ | 65% |
| 8 | $0.069 \pm 0.004$ | $14.73 \pm 0.91$ | $16.2 \pm 1.49$ | 51% |

With a certain set of samples, there were difficulties in fitting the model with two free parameters ($\kappa_r$ and $\Lambda_D$). The modified Landauer/Lundstrom model is a comprehensive model, taking into accounts many factors, and therefore data modeling becomes demanding. For the second set of samples (Fig. 8.21), which generally exhibit lower thermal conductivity than the first set (Fig. 8.20), the nanostructure size can only be calculated when $\kappa_r$ is fixed.
To enable extraction of $\Lambda_D$, the average value of $\kappa_r$ from the first data set was used ($\kappa_r = 0.1$). The representative pSi sample is shown in Fig. 8.22 together with the average, the lowest ($\sim 0.06$) and the highest ($\sim 0.15$) $\kappa_r$ values from the first samples' fitting. From the fits it is apparent that the models with the low and the average $\kappa_r$ are not good enough and improving the value is beneficial. The highest $\kappa_r$ fits the data the best, and the corresponding fit parameters are presented in Tab. 8.6.

**Table 8.6:** Scaling factor $\kappa_r$ (fixed), intrinsic thermal conductivity $\kappa_0$ at $\sim$ 300 K, nanostructure size $d$ and porosity of the second set of samples modeled with modified Landauer/Lundstrom model.

| Sample | $\kappa_r$ | $\kappa_0$ [$\mathrm{W\,m^{-1}\,K^{-1}}$] | $d$ [nm] | Porosity |
|---|---|---|---|---|
| 9 | 0.15 | $4.73 \pm 0.06$ | $4.08 \pm 0.02$ | 64% |
| 10 | 0.15 | $4.05 \pm 0.05$ | $3.32 \pm 0.01$ | 62% |
| 11 | 0.15 | $6.21 \pm 0.07$ | $5.36 \pm 0.02$ | 61% |
| 12 | 0.15 | $5.26 \pm 0.06$ | $4.39 \pm 0.01$ | 60% |
| 13 | 0.15 | $5.38 \pm 0.07$ | $4.49 \pm 0.02$ | 64% |
| 14 | 0.15 | $2.87 \pm 0.04$ | $2.30 \pm 0.01$ | 63% |
| 15 | 0.15 | $3.91 \pm 0.05$ | $3.15 \pm 0.01$ | 61% |
| 16 | 0.15 | $2.41 \pm 0.03$ | $1.87 \pm 0.01$ | 63% |

The fitted nanostructure size $d$ is decreased compared to the data in Tab. 8.5. The two sets of samples exhibit similar porosities, but the thermal conductivity is

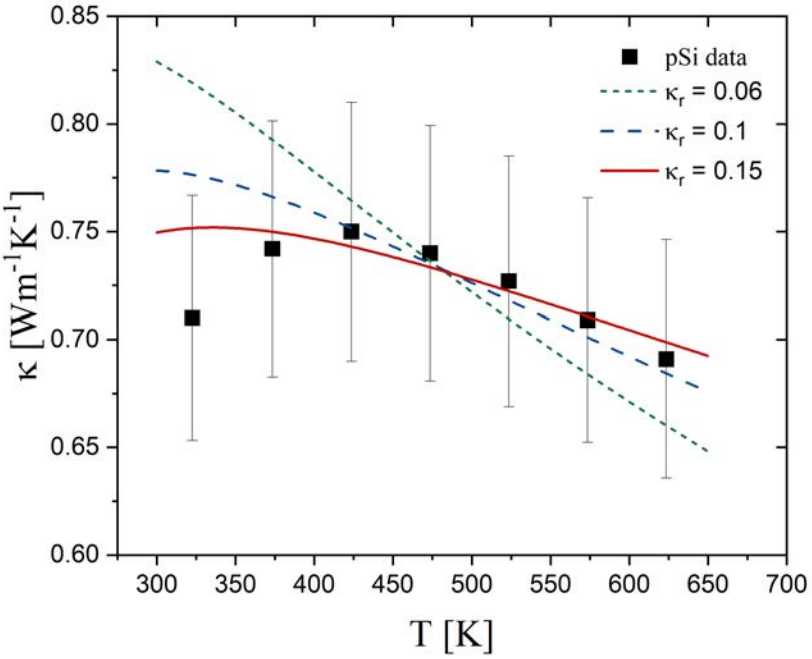


**Figure 8.22:** A representative fit of porous silicon data with the modified Landauer/Lundstrom model. Vertical lines are the data error bars.

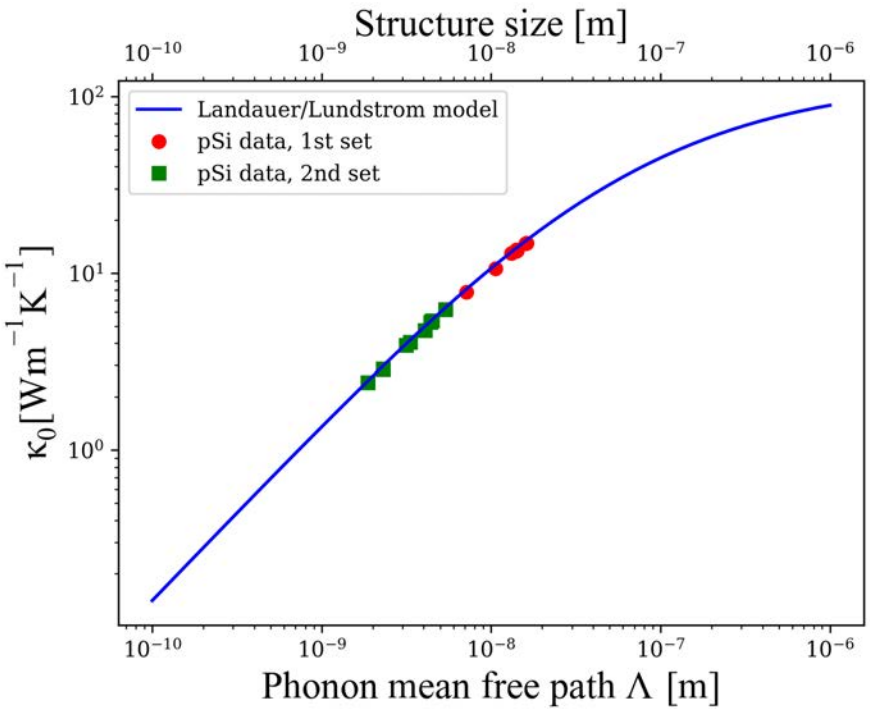


**Figure 8.23:** Landauer/Lundstrom model for intrinsic thermal conductivity $\kappa_0$ with modeled porous silicon samples at room temperature. Two sets of sample are distinguished: round symbols refer to the fully fitted samples, while square symbols refer to the fitted samples with fixed $\kappa_r$.

in general lower for the second set of samples. In this case, the lower $\kappa$ might be a result of a decreased pore-wall thickness, which scatters phonons more efficiently. The intrinsic thermal conductivity as a function of the mean free path of all samples and the modified Landauer/Lundstrom model is shown in Fig. 8.23. All samples show good agreement with the model.

### de Boor model

A simplified model describing the thermal conductivity in pSi (and bSi) was used by de Boor et al. [203]. It also employs an ansatz for the measured thermal conductivity that distinguishes between porosity effects and intrinsic thermal conductivity as defined by phonon scattering mechanisms

$$\kappa_0 = \frac{\kappa_{eff}}{(1-\Phi)}. \tag{8.31}$$

As in the Landauer/Lundstrom model, the contributions due to porosity and mean free path are decoupled, but with the simplified assumption that $\kappa_r = 1-\Phi$. The intrinsic thermal conductivity is here described by a kinetic model that ignores the spectral properties of phonons

$$\kappa_0 = \frac{1}{3} c v \Lambda. \tag{8.32}$$

Here, $c$ is the specific heat capacity, $v$ is the average phonon group velocity as discussed in Sec. 8.4.2 and $\Lambda_{bulk}$ is the phonon mean free path.
This model is directly applicable to our bulk silicon data ($\Phi = 0$) to extract $\Lambda_{bulk}(T)$. In the calculations, the heat capacity determined with differential scanning calorimetry is used, as in the LFA measurements. For porous silicon, one distinguishes between bulk-like phonon scattering $\Lambda_{bulk}$ and phonon scattering on the nanostructure $\Lambda_{nano}$. The total mean free path in pSi is $\Lambda_{pSi} = \left(\frac{1}{\Lambda_{bulk}} + \frac{1}{\Lambda_{nano}}\right)^{-1}$.
To determine $\Lambda_{nano} = \frac{3}{4}d$ one must define the structure size $d$. Assuming a simple geometrical model with round pores on a hexagonal lattice (Fig. 8.24) one writes

$$d_{calc} = l\left(1 - \sqrt{\frac{2\sqrt{3}}{\pi}\Phi}\right). \tag{8.33}$$

$d_{calc}$ is the geometrically defined sample structure size and $l$ is the pore-pore distance.
The thermal conductivity is then

$$\kappa_0(T,d) = \frac{1}{3} c(T) v \left(\frac{1}{\Lambda_{bulk}(T)} + \frac{4}{3d}\right)^{-1}. \tag{8.34}$$

Eq. 8.34 allows to predict the thermal conductivity in pSi depending on the phonon mean free path $\Lambda_{pSi}$ as illustrated by the red line in Fig. 8.25. The equation can also be used to determine the characteristic length $d_{fit}$ from the measured T-dependent $\kappa$ data (see Tab. 8.7, Fig. 8.25 and Fig. 8.27). For comparison we also provide in Tab. 8.7 the purely geometrically determined values for the characteristic size $d_{calc}$ (Eq. 8.33).

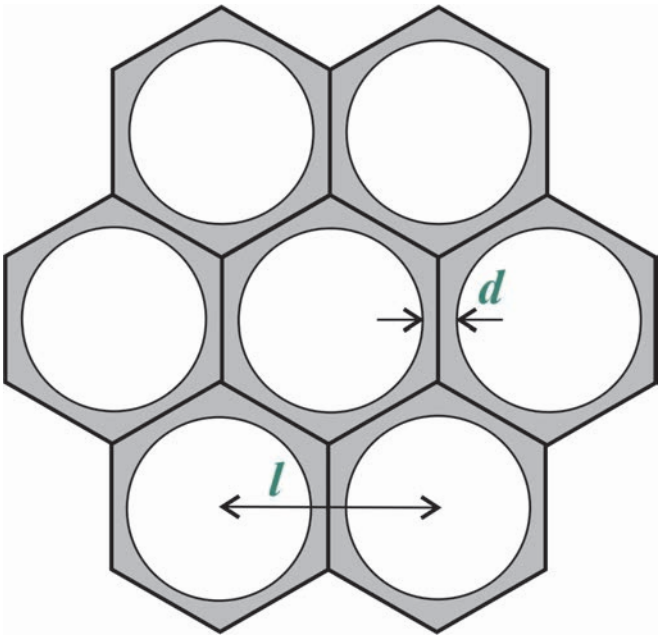


**Figure 8.24:** Honeycomb structure used to calculate the nanostructure size in porous silicon.

**Table 8.7:** Intrinsic thermal conductivity $\kappa_0$ at $\sim 300\,\mathrm{K}$, pore radius $r$, calculated and fitted nanostructure size $d$ and porosity of eight samples.

| Sample | $\kappa_0$ [$\mathrm{W\,m^{-1}\,K^{-1}}$] | $r_{isotherm}$ [$nm$] | $d_{calc}$ [$nm$] | $d_{fit}$ [$nm$] | Porosity |
|---|---|---|---|---|---|
| 1 | $5.09 \pm 0.40$ | $4.85 \pm 0.60$ | $4.32 \pm 2.47$ | 3.68 | 65% |
| 3 | $2.72 \pm 0.22$ | $3.35 \pm 0.40$ | $3.30 \pm 1.14$ | 2.03 | 61% |
| 3 | $4.06 \pm 0.33$ | $5.7 \pm 0.68$ | $5.34 \pm 1.21$ | 2.94 | 63% |
| 4 | $2.21 \pm 0.18$ | $4.03 \pm 0.48$ | $3.96 \pm 2.57$ | 1.66 | 61% |
| 5 | $4.59 \pm 0.37$ | $3.7 \pm 0.44$ | $4.12 \pm 0.46$ | 3.35 | 56% |
| 6 | $2.17 \pm 0.17$ | $4.45 \pm 0.53$ | $4.27 \pm 1.21$ | 1.59 | 52% |
| 7 | $2.34 \pm 0.19$ | $4.5 \pm 0.54$ | $4.01 \pm 1.14$ | 1.65 | 65% |
| 8 | $2.07 \pm 0.17$ | $3.7 \pm 0.44$ | $4.68 \pm 1.49$ | 1.44 | 51% |
| 9 | $1.97 \pm 0.15$ | $4.5 \pm 0.54$ | $4.11 \pm 0.30$ | 1.74 | 64% |
| 10 | $1.6 \pm 0.12$ | $5.05 \pm 0.60$ | $4.84 \pm 0.33$ | 1.50 | 62% |
| 11 | $2.38 \pm 0.19$ | $4.25 \pm 0.51$ | $4.18 \pm 0.28$ | 2.24 | 61% |
| 12 | $1.97 \pm 0.15$ | $4.05 \pm 0.48$ | $4.08 \pm 0.27$ | 1.96 | 60% |
| 13 | $2.24 \pm 0.17$ | $5.05 \pm 0.60$ | $4.61 \pm 0.34$ | 2.20 | 64% |
| 14 | $1.16 \pm 0.09$ | $4.45 \pm 0.53$ | $4.16 \pm 0.29$ | 1.17 | 63% |
| 15 | $1.50 \pm 0.12$ | $3.4 \pm 0.41$ | $3.34 \pm 0.24$ | 1.48 | 61% |
| 16 | $0.97 \pm 0.08$ | $4.45 \pm 0.53$ | $4.16 \pm 0.29$ | 0.97 | 63% |

The parameters in Tab. 8.7 show the calculated and fitted values of the nanostructure size ($d$). The fitted values are systematically lower than the calculated ones and also significantly lower than the values obtained from the more advanced, modified Landauer/Lundstrom model. In case of the nanostructure size $d_{calc}$ calculated using the methodology by de Boor et al. [203], the sizes do not vary significantly and are in the range of the sizes of the pore walls calculated using the UV-Vis data ($\sim 4\,\mathrm{nm}$, see Tab. 8.2). The fitted nanostructure size val-

ues $d_{fit}$ are between 1 nm and 2 nm, which seems to be an underestimation. The calculated nanostructure sizes $d_{calc}$ show no major sample to sample variation, even though they present a range of thermal conductivity. The porosity also does not vary significantly ($\sim 60\%$). The intrinsic thermal conductivity as a function of the phonon mean free path (Fig. 8.25) show that the samples modeled with $d_{calc}$ scatter heavily. The second set of samples, modeled with $d_{fit}$ seems to agree with the de Boor model, while the first set diverges from it.

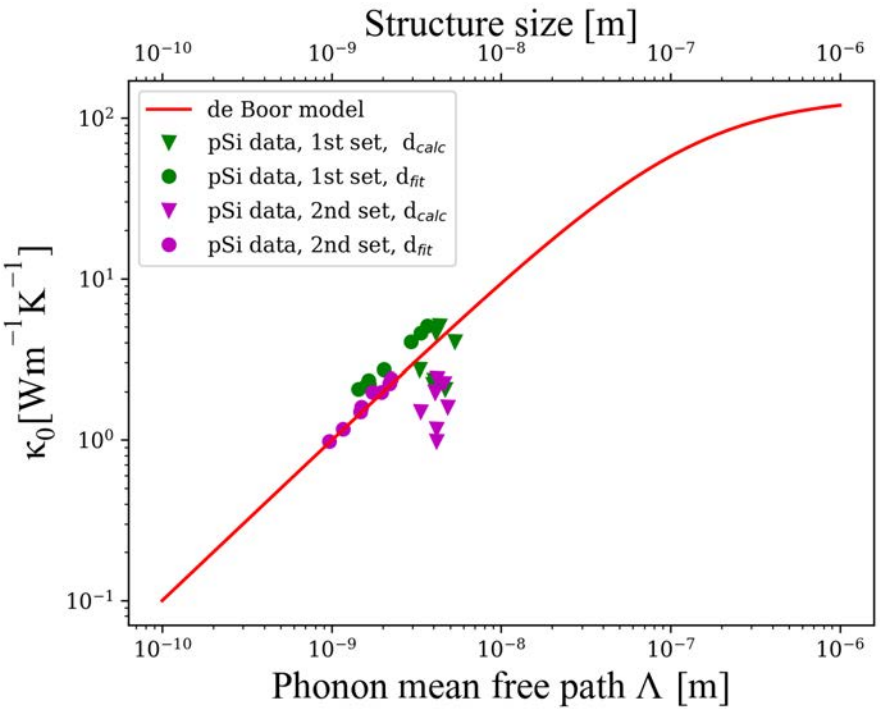


**Figure 8.25:** de Boor model for intrinsic thermal conductivity $\kappa_0$ with modeled porous silicon samples at room temperature. All data have been modeled with $d_{calc}$ (triangle symbols) and $d_{fit}$ (round symbols).

While the first set of samples fit the de Boor model at first glance, the closer look into the data shows the differences between the data and the models. Fig. 8.26 shows the pSi data of a representative sample from the first set together with the modified Landauer/Lundstrom model fit and the de Boor model fit. The first model appears to be consistent with the data and the temperature-dependence while the de Boor model shows the opposite temperature-dependence in this temperature range.

The results of the de Boor model for the second set of samples are shown on Fig. 8.27. The model with the fitted value of $d_{fit}$ seems to fits better the samples that show low thermal conductivities. The inset shows a comparison between the models with two different $d$ values. The model using the geometrically calculated values of $d_{calc}$ (dashed line) does not fit the data at all, however, the nanostructure size corresponds better to the values extracted from the modified Landauer/Lundstrom model and the UV-Vis data (Tab. 8.2).

It is important to note that de Boor uses the gray medium approximation [23], which does not account for phonon spectral properties which may have an important effect on the thermal conductivity. Fitted $d_{fit}$ values are lower than

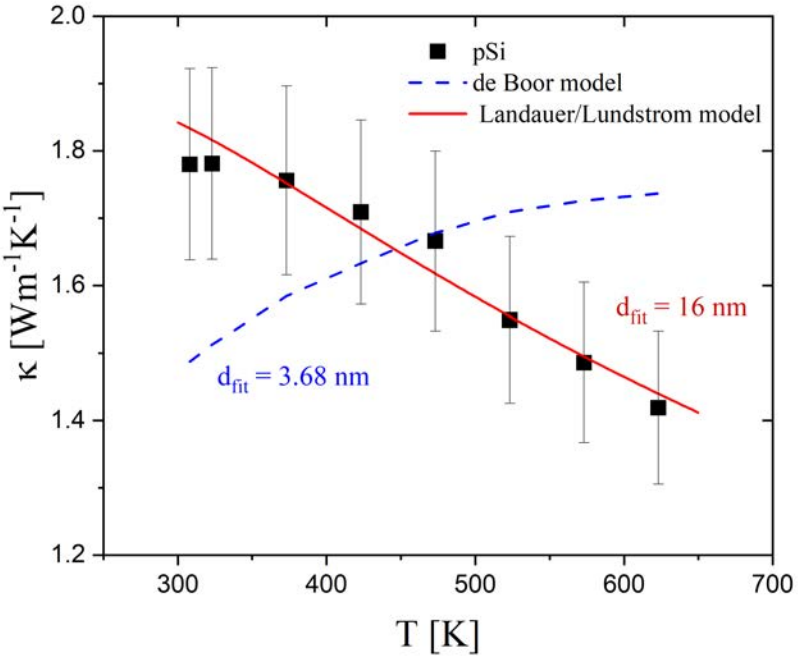


**Figure 8.26:** A representative sample of the 1st set plotted together with the modified Landauer/Lundstrom model and the de Boor model. The modified Landauer/Lundstrom model fith the data incomparably better to the simplified de Boor model.

calculated ones $d_{calc}$ and also an order of magnitude lower that the nanostructure size obtained with the modified Landauer/Lundstrom model. Pore-wall size in the range of 1-2 nm seems unreasonable for our pSi samples.
The de Boor model for thermal conductivity is an interesting, but too simplistic method to model the $\kappa$, especially for nanostructured materials. The influence of the nanostructure on $\kappa$ plays an important role in data evaluation and fitting. Porosity correction used here $(1-\Phi)$ is the simplest approach that does not take into account any nanostructure. The scaling factors $(1-\Phi)$ are in the range of $0.3-0.4$, which is greatly overestimated. This leads to an underestimation of the nanostructure size $d_{fit}$. The modified Landauer/Lundstrom model allows to describe all data meaningfully, while the de Boor model does not provide a general approach to treating the $\kappa$. In the next section, the data obtained with the modified Landauer/Lundstrom model are used for a more detailed analysis of the effect of porosity on $\kappa_{eff}$.

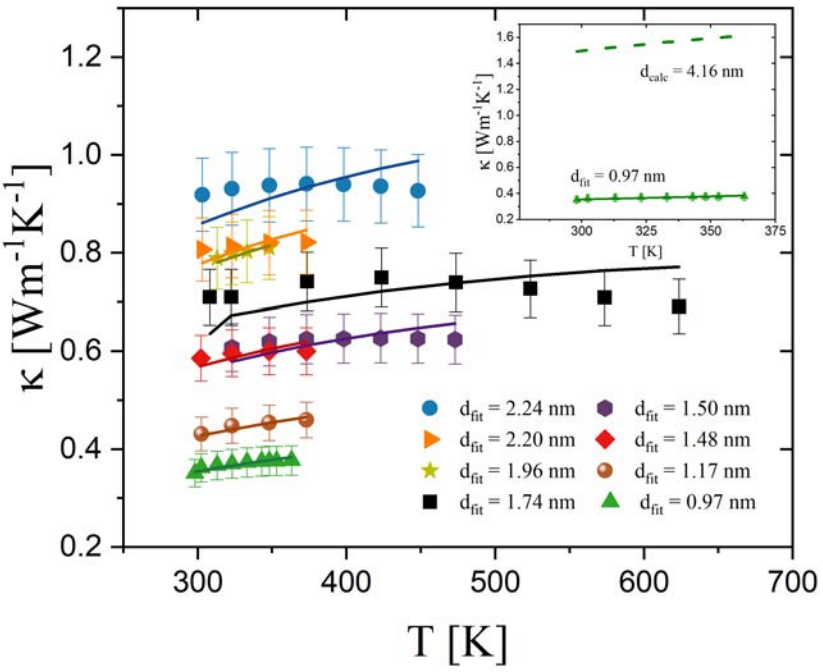


**Figure 8.27:** The thermal conductivity of porous silicon samples versus temperature. The fits to the de Boor model (Eq. 8.34) are displayed together with the corresponding pSi data. The inset shows the models using the $d_{fit}$ (solid line) and the $d_{calc}$ (dashed line). The de Boor model using the $d_{calc}$ values overestimates the $\kappa$ of pSi.

**Models for effective thermal conductivity in composite materials**

The problem of thermal and electrical transport in materials that consist of two phases has been discussed intensively. The first attempts to model conduction in composite materials are from Maxwell [204] and Rayleigh [205]. The models that predict the properties of composites using volume fractions and properties of the constituents are known as effective medium theories. These early models do not take into account the interfacial thermal resistance between the phases. Only recent models take percolation phenomena into account. A few of the most common approaches are compared below to understand the $\kappa_r$ values as obtained from the Landauer/Lundstrom fits of the data.

Maxwell's approach [204] to the effective thermal conductivity of composite materials considers the problem of dispersed spherical particles in a continuous matrix. Maxwell's expression for the effective thermal conductivity is [206, 207]

$$\frac{\kappa_{eff}}{\kappa_m} = 1 + \frac{3\Phi}{\left(\frac{\kappa_1+2\kappa_m}{\kappa_1-\kappa_m}\right) - \Phi} (= \kappa_r), \tag{8.35}$$

where $\kappa_m$ is the conductivity of the continuous matrix, $\kappa_1$ is the conductivity of the filler and $\Phi$ is the volume fraction of the filler. The model ignores the thermal interaction between different dispersed spheres, and is valid only for low porosity ($\Phi < 25\%$).

The Rayleigh model [205] considers a continuous matrix and a filler phase that is arranged on a cubic array. It includes the thermal interactions and could also be used to express $\kappa$ for a composite with a filler phase in the form of cylindrical pores. The expression is

$$\frac{\kappa_{eff}}{\kappa_m} = 1 + \frac{3\Phi}{\left(\frac{\kappa_1+2\kappa_m}{\kappa_1-\kappa_m}\right) - \Phi + 1.569\left(\frac{\kappa_1+\kappa_m}{3\kappa_1-4\kappa_m}\right)\Phi^{10/3} + ...}, \tag{8.36}$$

where the higher-order terms in the denominator are usually ignored.

The Bruggeman model is a form of a differential effective medium theory. The differential form of the equations are a result of integration embedding principle [208]. The initially low concentration of the filler phase is gradually increased by infinitesimal additions. As the filling phase fraction is increased, the property of the continuous medium changes from $\kappa_m$ to $\kappa_{eff}$. The Bruggeman formula is [209, 210]

$$(1-\Phi)^3 = \left(\frac{\kappa_m}{\kappa_{eff}}\right)^{(1+2\alpha)/(1-\alpha)} \left(\frac{\kappa_{eff} - \kappa_1(1-\alpha)}{\kappa_m - \kappa_1(1-\alpha)}\right)^{3/(1-\alpha)}. \tag{8.37}$$

It introduces a dimensionless parameter $\alpha$ that depends on the interfacial thermal resistance between the phases. It is defined as $\alpha = r/r_k$ where $r$ is the radius of the filler particles and $r_k$ is the Kapitza radius ($r_k = R_{int}\kappa_m$) and $R_{int}$ its interfacial thermal resistance.

Kirkpatrick developed a self-consistent effective-medium approximation (SCEMA) which includes a percolation threshold [211]. The self-consistent theory assumes that each grain (inclusion) is symmetrically embedded into an effective medium with $\kappa_{eff}$. Including the percolation threshold $\Phi_c$ one obtains [208]

$$0 = (1-\Phi)\frac{\kappa_m - \kappa_{eff}}{\kappa_m + (1/\Phi_c - 1)\kappa_{eff}} + \Phi\frac{\kappa_1 - \kappa_{eff}}{\kappa_1 + (1/\Phi_c - 1)\kappa_{eff}} \tag{8.38}$$

For porous silicon one assumes $\kappa_1 = 0$. Eq. 8.38 becomes

$$\kappa_{eff} = \kappa_m \left(1 - \frac{\Phi}{\Phi_c}\right). \tag{8.39}$$

Above $\Phi_c$ there is no conduction because one has no continuous path for thermal transport.

The Lewis-Nielsen model is a simple concept that accounts for the shape and patterns of the filler phase embedded in a continuous matrix. It does not include interfacial thermal resistance. The effective thermal conductivity is [207]

$$\kappa_{eff} = \frac{1 + AB(1-\Phi)}{1 - B\Psi(1-\Phi)} \tag{8.40}$$

where

$$B = \left(\frac{\kappa_1/\kappa_m - 1}{\kappa_1/\kappa_m + A}\right) \tag{8.41}$$

$$\Psi = 1 + \left(\frac{1-\Phi_m}{\Phi_m^2}\right)(1-\Phi) \tag{8.42}$$

where again $\kappa_m$ is the matrix thermal conductivity, $\kappa_1$ is the filler thermal conductivity, $\Phi$ is the porosity of pSi ($1-\Phi$ is the filler volume fraction). The factors $\Phi_m$ and $A$ are the maximum filler volume fraction and filler shape coefficient. For porous silicon data, with $A = 1.5$ that corresponds to a sphere-like shape of the filler component, the value $\Phi_m = 0.212 \pm 0.021$ was fitted.

The presented models were used to describe the relative thermal conductivity $\kappa_r$, extracted from modified Landauer/Lundstrom approach, as a function of porosity and plotted in Fig. 8.28. The models were plotted together with the data points of the fully fitted pSi samples.

Data points corresponding to the pSi samples lie in the vicinity of the Lewis-Nielsen and Kirkpatrick curves. The application of the Lewis-Nielsen is questionable since the maximum packing fraction of the second phase (pores) is around $\Phi_m = 21\%$ and is way below the values of porosity for pSi samples. Most of the data agree well with the Kirkpatrick model, with percolation threshold of $\Phi_c = 68\%$ Comparison of different approaches to the scaling factor from different models shows that the de Boor approach significantly overestimates the effective medium model.

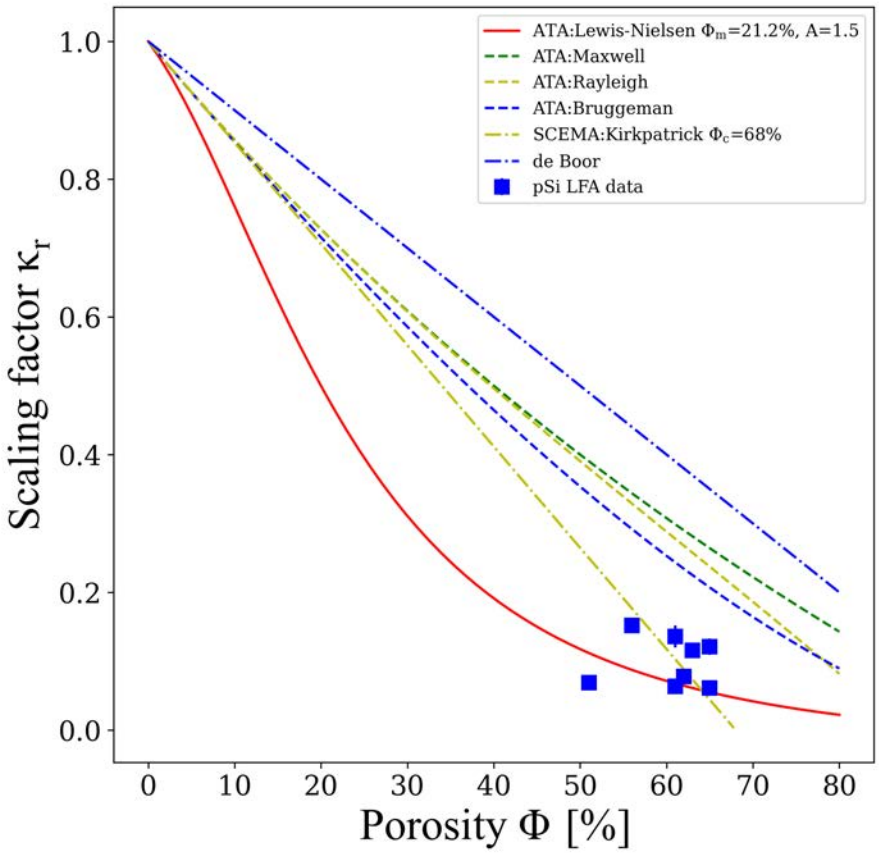


**Figure 8.28:** Relative thermal conductivity $\kappa_r$ as a function of porosity $\Phi$ compared with various effective medium models.

## 8.5 Thermal conductivity of P3HT-pSi hybrids

The thermal conductivity of hybrids was measured from room temperature to 365 K. $\kappa$ is constant over this temperature range. The tested hybrids were synthesized using a pSi membrane with low thermal conductivity ($0.35\,\mathrm{W\,m^{-1}\,K^{-1}}$). The room temperature $\kappa$ of P3HT-pSi hybrids are in the range of $1\,\mathrm{W\,m^{-1}\,K^{-1}}$, which is about a factor of three higher than for the empty membrane. $\kappa$ increases upon polymer infiltration into the pSi matrix. The components' conductivity is low, but the polymer still has a higher thermal conductivity than air or helium [212]. The polymer medium connects the pore walls, filling about 50% of the pore space and enhances the thermal contact between silicon pore walls.
Filled samples show higher thermal conductivity than pSi membranes. Doping the hybrid with $FeCl_3$ further lowers the thermal conductivity by introducing additional scattering centres.
A three-medium approach to thermal conductivity [208] is used to model the behavior of thermal conductivity of the hybrids with respect to the pore filling. For the three-medium thermal conductivity one uses the equation [208]

$$\frac{\kappa_{hyb} - \kappa_0}{\kappa_{hyb} + 2\kappa_0} = \Sigma\nu_i \frac{\kappa_i - \kappa_0}{\kappa_i + 2\kappa_0} \tag{8.43}$$

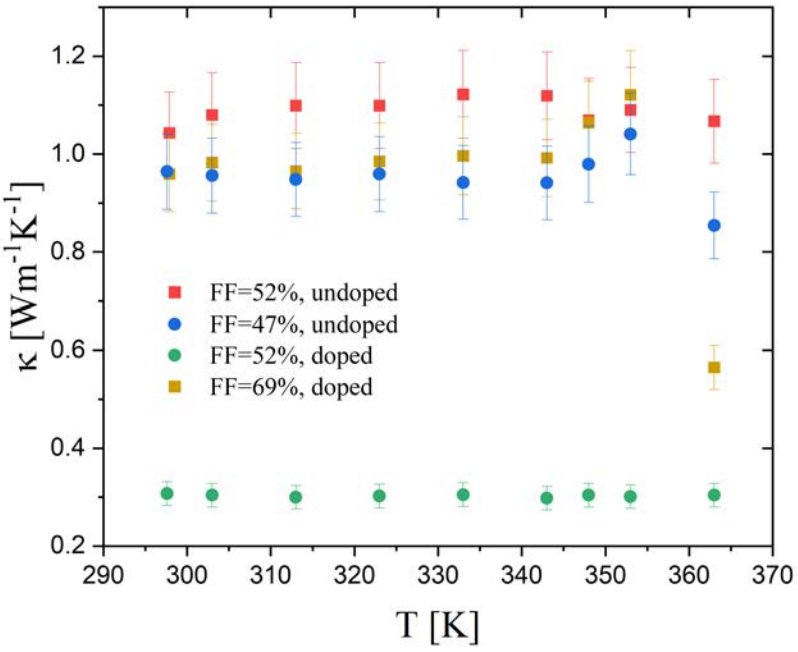


**Figure 8.29:** Thermal conductivity of hybrids. The filling factor is shown.

where $\nu_i$ is the component fraction and $\kappa_i$ is the component thermal conductivity. In this model, the thermal conductivity of silicon host ($\kappa_0$), pores ($\kappa_{air} = 0$) and P3HT ($\kappa_{P3HT}$) are taken into account. First, the $\kappa_0$ is extracted taking into account only two medium (silicon and air), using the porous silicon experimental data ($\kappa_{pSi}$)

$$\kappa_0 = \kappa_{pSi} \frac{1 + \frac{1}{2}\nu_{pores}}{1 - \nu_{pores}}. \tag{8.44}$$

Here, $\nu_{pores}$ corresponds to the porosity of the pSi membrane used to synthesize the hybrid (in this case $\Phi = \nu_{pores} = 63\%$).
The equation to get the effective thermal conductivity of the hybrids is

$$\frac{\kappa_{hyb} - \kappa_0}{\kappa_{hyb} + 2\kappa_0} = \nu_{P3HT} \frac{\kappa_{P3HT} - \kappa_0}{\kappa_{P3HT} + 2\kappa_0} - \frac{1}{2}\nu_{pores}. \tag{8.45}$$

The main medium is the silicon and the filing phases are air (pores) and the polymer. With the increase of the polymer filling fraction, the share of the air decreases accordingly.
This model was used to predict the thermal conductivity of hybrids depending on the P3HT filling fraction. For the samples based on the membrane with $\sim 0.35\,\mathrm{W\,m^{-1}\,K^{-1}}$, the corresponding data is plotted in Fig. 8.30. Without the polymer filling, the thermal conductivity of the system corresponds to the $\kappa$ of porous silicon.
Since the $\kappa_{P3HT}$ of the P3HT confined in pSi is not known, an assumption was made based on literature data. P3HT structures with different shapes, morphology and preparation techniques present a variety of thermal conductivity. The models shown in Fig. 8.30 are modeled with $\kappa_{P3HT}$ values of the P3HT

films [213, 214], nanowires [215] and nanofiber [216].

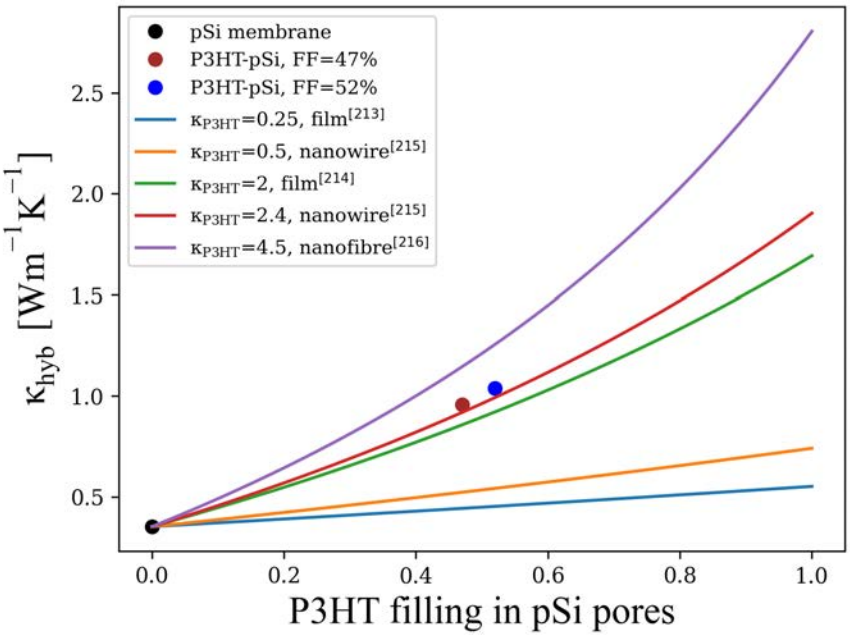


**Figure 8.30:** Three-medium model for thermal conductivity in hybrid materials. The hybrid's $\kappa$ as a function of polymer filling in 63% porous membrane. The conductivity raises with increasing polymer fraction. The models with different $\kappa_{P3HT}$ values are displayed on the plot.

Compared to the empty porous silicon, the undoped hybrid exhibits larger $\kappa$ while in the doped hybrids the lower thermal conductivity is observed due to enhanced scattering. The hybrid data $\kappa_{hyb}$ corresponds well with the model using the $\kappa_{P3HT}$ value of $2.4\,\mathrm{W\,m^{-1}\,K^{-1}}$. Structural confinement of P3HT in the pores might influence the thermal transport of the polymer phase. The lowest literature values of $\kappa_{P3HT}$, desired for the envisioned thermoelectric applications, used for fit are of the polymer film [213].
The obtained $\kappa_{hyb}$ values of P3HT-pSi hybrids combined with the power factor values results in the thermoelectric figure of merit ZT between 0.024 and 0.037 at room temperature. These values heavily surpass the ZT of pSi ($ZT = 2 \times 10^{-6}$). To estimate the ZT of P3HT films for comparison, we take the highest power factor of $FeCl_3$-doped P3HT film from Tab. 8.3 ($40\,\mu\mathrm{W\,m^{-1}\,K^{-2}}$) and the lowest ($0.25\,\mathrm{W\,m^{-1}\,K^{-1}}$ [213]) and the highest ($2\,\mathrm{W\,m^{-1}\,K^{-1}}$ [214]) $\kappa_{P3HT}$ of the P3HT films used in the modeling of $\kappa_{hyb}$. These values results in ZT between 0.006 and 0.048. The ZT values of the P3HT-pSi hybrids are higher or comparable to those of the P3HT films, highlighting the fulfillment of the objectives of this work.

# Chapter 9

# Summary

This thesis presents comprehensive studies on the synthesis, structure and transport properties of organic-inorganic hybrids based on the conductive polymer P3HT and mesoporous silicon. This work successfully investigates hybrid thermoelectric materials based on mesoporous silicon and confirms that the poor thermoelectric properties of pSi can be improved by embedding a conductive polymer in the pore space. The broad approach to design, synthesize and characterize the hybrid system was part of the project funded by the Deutsche Forschungsgemeinschaft under number 402553194.

The synthesis approach followed here consists of two steps: electrochemical anodization of the silicon wafer in an HF-based electrolyte and filling pSi with P3HT by melt infiltration. Porous silicon membranes are synthesized by means of electrochemical anodization of silicon and are the base material of the work. The etching cell designed and built at Helmholtz-Zentrum Berlin during this PhD work is thoroughly discussed. The double-wall container and peristaltic pumping system ensure the safety of the experimentalist during the electrochemical anodization process. The cell comes with the software that allows to create custom etching profiles.

The structural characterization of pSi includes measurements of sorption isotherm that reveal 60% porosity of pSi with the average pore radius of $\sim 4.5\,\mathrm{nm}$. The challenge of embedding P3HT into the 9 nm wide pores of pSi was successfully tackled by the melt infiltration method in the glove box environment. The synthesis of the organic-inorganic hybrid was completed by doping by immersion in a solution of $FeCl_3$ in chloroform. Successful infiltration and diffusion doping are confirmed by EDX mapping, gravimetry and sorption isotherms which show that the polymer occupies about 50% of the pore space. Synchrotron diffraction experiments do not reveal a specific ordering of the polymer inside the pores, but further confirm the incorporation of the dopant into the polymer, revealing an increased lattice constant in the doped hybrids.

A deep understanding of the transport mechanisms in pSi is essential for understanding the hybrids' performance. Thermoelectric characterization includes determination of electrical conductivity, Seebeck coefficient and thermal conductivity for mesoporous silicon and P3HT-pSi hybrids. First, the heat capacity of porous silicon is modeled using a modified Debye-Einstein model that takes into account surface effects in the sample. The excess heat capacity in pSi is attributed to the surface states that are significant in nanostructured materials. The boson peak associated with the complex pore structure and the silicon oxide layer covering pSi is also discussed.

The UV-Vis absorption spectra show an increased optical band-gap in pSi compared to bSi, which is due to the quantum confinement effect in pSi. The electrical conductivity in pSi decreases by five orders of magnitude upon porosification. Analysis of $\sigma$ and its activation energy reveals the Meyer-Neldel compensation rule. The Meyer-Neldel energy in pSi $E_{MN} = 54\,\mathrm{meV}$ is close to the maximum of the phonon density of states in silicon, which may indicate multiphonon assisted charge carrier hopping. Analysis of the Seebeck coefficient and its activation energy further suggests that the transport mechanism in pSi can be related to transport in localized states accompanied by multiphonon absorption.
Electric transport in hybrids has been shown to improve by five orders of magnitude compared to an empty membrane ($13\,\Omega^{-1}\,\mathrm{cm}^{-1}$ vs. $10^{-4}\,\Omega^{-1}\,\mathrm{cm}^{-1}$). The transport data is analyzed using the Kang-Snyder model, which postulates a power law for $\sigma_E(E,T)$, a transport function that describes conductivity at energy E and temperature T. The Boltzmann transport equation, which is the basis of the Kang-Snyder model, helps to identify the dominant scattering mechanism affecting charge transport in semiconductors. The power law proposed by Kang and Snyder is mainly used to describe transport in conductive polymers. The power law exponent $s$ is typically equal to 3 in the P3HT polymer that conducts the carriers by hopping. The modeled P3HT-pSi hybrids also show the power law $s = 3$, but the hybrids show different temperature dependence of $\sigma$ than P3HT. The pSi electric transport data is also modeled using the Kang-Snyder approach. The same relationship $s = 3$ occurs with $\sigma_{E0}$ values in the same order of magnitude as in hybrids (compared to three orders of magnitude lower for P3HT), indicating that the porous silicon matrix is the main conductive phase in the hybrid. Based on the results, a transport mechanism in hybrids was proposed in which a doped polymer mainly provides charge carriers to the system, similar to the behavior of a doped semiconductor.
The thermoelectric characterization is concluded with an analysis of thermal transport. Porous silicon samples show drastically reduced $\kappa$ ($0.3-2\,\mathrm{W\,m^{-1}\,K^{-1}}$) compared to bulk silicon ($63\,\mathrm{W\,m^{-1}\,K^{-1}}$) due to nanostructuring and high porosity. The data are fitted using a modified Landauer/Lundstrom model that takes into account the size of the system's nanostructure. The results are then treated with the effective medium models, which shows that the pSi samples agree well with the Kirkpatrick model with a 68% percolation threshold. Hybrid's $\kappa$ values show an increase in thermal conductivity compared to empty membranes ($1\,\mathrm{W\,m^{-1}\,K^{-1}}$ vs. $0.3\,\mathrm{W\,m^{-1}\,K^{-1}}$ for the same base pSi membrane). After doping, the thermal conductivity is slightly reduced, which is the result of increased ionized impurity scattering.
The power factor values PF= $\sigma S^2$ obtained for hybrids range from $81\,\mu\mathrm{W\,m^{-1}\,K^{-2}}$ to $122\,\mu\mathrm{W\,m^{-1}\,K^{-2}}$ and are the first reported values for P3HT-pSi systems. In the measured T range, the highest PF was obtained at room temperature and the values are comparable to other organic-inorganic hybrids using P3HT as the organic phase [96]. Combined with the thermal conductivity data for the hybrids, the resulting ZT at room temperature is between 0.024 and 0.037, which is higher than the measured thermoelectric performance of bSi at 330 K ($ZT = 0.0034$) and pSi at 300 K ($ZT = 2 \times 10^{-6}$). The figure of merit of the P3HT-pSi hybrids exceeds also the values of boron-doped pSi $ZT < 0.025$ [23]. Comparison to the estimated ZT values of $FeCl_3$-doped P3HT films (0.006 and 0.048) shows that our

organic-inorganic hybrids are comparable in some cases, but mostly outperform the thermoelectric performance of their constituents.
To conclude, the incorporation of the P3HT organic phase into the pore space of nanostructured mesoporous silicon improves its overall thermoelectric performance. The combination of both phases changes the Fermi energy level in the pSi membrane, improving its electrical transport. Further optimization of the synthesis method and post-treatment could improve the filling factor of the hybrids and the ordering of P3HT inside the pores, which may be beneficial for faster charge transport.

# Bibliography


[1] T. Seebeck, *Ann. Phys.*, 1826, **82**, 133–160.

[2] J. Peltier, *Ann. Chim*, 1834, **56**, 371–386.

[3] E. Commission, European Union, [Accessed: 2023], `https://climate.ec.europa.eu/eu-action/climate-strategies-targets/2050-long-term-strategy_en`.

[4] D. Rowe, *Thermoelectric Handbook. Macro to Nano*, Taylor and Francis Group, 2006.

[5] M. Bharti, A. Singh, S. Samanta and D. K. Aswal, *Progress in Material Science*, 2018, **93**, 270–310.

[6] B. Russ, A. Glaudell, J. Urban, C. M. L. and R. A. Segalman, *Nature Reviews Materials*, 2016, **1**, 1–14.

[7] H. Yao, Z. Fan, H. Cheng, X. Guan, C. Wang, K. Sun and J. Ouyang, *Journal of Physics: Condensed Matter*, 2018, **39**, 1700727.

[8] G. Kim, L. Shao, K. Zhang and K. P. Pipe, *Nature Materials*, 2013, **12**, 719–723.

[9] J. A. Rivera, A. C. Castillo and M. D. L. L. M. Gonzalez, *Organic Semiconductors. In Semiconductors*, Springer Nature Switzerland, 2019.

[10] H. Bin, L. Gao, Z.-G. Zhang, Y. Yang, Y. Zhang, C. Zhang, S. Chen, L. Xue, C. Yang, M. Xiao and Y. Li, *Nature Communications*, 2016, **7**, 1–11.

[11] U.-Y. Cheng, S.-H. Yang and C.-S. Hsu, *Chem. Rev.*, 2009, **109**, 5868–5923.

[12] P. C. Y. Chow and T. Someya, *Advanced Materials*, 2020, **32**, 1–26.

[13] A. Uhlir, *Bell System Technical Journal*, 1956, **35**, 333–347.

[14] L. Canham, *Applied Physics Letters*, 1990, **57**, 1046.

[15] L. Canham, *Journal of Applied Physics*, 1997, **82**, 909.

[16] M. Ashuri, Q. He and L. L. Shaw, *Nanoscale*, 2016, **8**, 74–103.

[17] P. Huber, *Journal of Physics: Condensed Matter*, 2015, **27**, 103102.

[18] M. J. Sailor, *Porous Silicon in Practice: Preparation, Characterization and Applications*, Wiley, 2012.

[19] S. H. C. Anderson, H. Elliott, D. J. Wallis, L. T. Canham and J. J. Powell, *physica status solidi (a)*, 2003, **197**, 331–335.

[20] J. de Jong, R. Lammertink and M. Wessling, *Lab on a chip*, 2006, **6**, 1125–1139.

[21] M. Ge, J. Rong, R. Fang and C. Zhou, *Nano Letters*, 2012, **12**, 2318–2323.

[22] P. Menna, D. F. G.D. and V. La Ferrara, *Solar Energy Materials and Solar Cells*, 1995, **37**, 13–24.

[23] J. de Boor, D. S. Kim, X. Ao, M. Becker, N. F. Hinsche, I. Mertig, P. Zahn and V. Schmidt, *Applied Physics A*, 2012, **107**, 789–794.

[24] G. Schierning, *Applied Physics A*, 2014, **211**, 1235–12494.

[25] C. R. Ocier, N. A. Krueger, W. Zhou and P. V. Braun, *ACS Photonics*, 2017, **4**, 909–914.

[26] V. Robbiano, G. M. Paternò, A. A. La Mattina, S. G. Motti, G. Lanzani, F. Scotognella and G. Barillaro, *ACS Nano*, 2018, **12**, 4536–4544.

[27] S. Mariani, V. Robbiano, L. Strambini, A. Debrassi, G. Egri, L. Dähne and G. Barillaro, *Nature Communications*, 2018, **9**, 5256.

[28] C. Hong, J. Lee, H. Zheng, S. Hong and C. Lee, *Nanoscale Research Letters*, 2011, **6**, 5256.

[29] A. Ressine, I. Corin, K. Järås, G. Guanti, C. Simone, G. Marko-Varga and T. Laurell, *Electrophoresis*, 2007, **28**, 4407–4415.

[30] H. Alhmoud, B. Delalat, R. Elnathan, A. Cifuentes-Rius, A. Chaix, M.-L. Rogers, J.-O. Durand and N. Voelcker, *Advanced Functional Materials*, 2014, **25**, 1–6.

[31] R. Elnathan, A. Holle, J. Young, M. George, O. Heifler, A. Goychuk, E. Frey, R. Kemkemer, J. Spatz, A. Kosloff, F. Patolsky and N. Voelcker, *Journal of Nanobiotechnology*, 2021, **19**, 1–6.

[32] E. Vasani, R.B. Szili, G. Rajeev and N. Voelcker, *Chem. Asian J.*, 2017, **12**, 1605–1614.

[33] T. Tieu, M. Alba, R. Elnathan, A. Cifuentes-Rius and N. Voelcker, *Advanced Therapeutics*, 2019, **2**, 1800095.

[34] S. Micera and E. Redolfi Riva, *Nature Materials*, 2022, **21**, 614–616.

[35] A. Prominski, J. Shi, J. Li, P.and Yue, Y. Lin, J. Park, TianB. and M. Y. Rotenberg, *Nature Materials*, 2022, **21**, 647–655.

[36] M. Jeong, Y. Jung, J. Yoon, J. Kang, W. Lee, S.H. Back, H. Kim, M. Sailor, D. Kim and J.-H. Park, *ACS Nano*, 2022.

[37] A. Dahiya, F. Morini, S. Boubenia, K. Nadaud, D. Alquier and G. Poulin-Vittrant, *Advanced Materials Technologies*, 2018, **3**, 1700249.

[38] C. Xin, Z. Hu, Z. Fang, M. Chaudhary, H. Xiang, X. Xu, L. Aigouy and Z. Chen, *Materials Today Energy*, 2021, **22**, 100859.

[39] A. Stranz, J. Kahler, A. Waag and E. Peiner, *Journal of Electronic Materials*, 2013, **42**, 2381–2387.

[40] P. Rodgers, *Nature Nanotechnology*, 2008, **3**, 76.

[41] J.-H. Lee, J. C. Grossman, J. Reed and G. Galli, *Appl. Phys. Lett.*, 2007, **91**, 223110.

[42] A. Drost, P. Steiner, H. Moser and W. Lang, *Sensors and Materials*, 1995, **7**, 111–120.

[43] R. Anderson, R. Muller and C. Tobias, *J. Electrochem. Soc*, 1991, **138**, 3406–3411.

[44] V. Aroutiounian and M. Ghulinyan, *Phys Stat Sol (a)*, 2003, **197**, 462–466.

[45] R. Martín-Palma, H. Cabrera, B. Martín-Adrados, D. Korte, E. Pérez-Cappe, Y. Mosqueda, M. A. Frutis and E. Danguillecourt, *Materials Research Express*, 2018, **5**, 015004.

[46] J. Tang, H.-T. Wang, H.-T. Lee, M. Fardy, Z. Huo, T. Russell and P. Yang, *Nano Letters*, 2010, **10**, 4279–4283.

[47] L. Yang, D. Huh, R. Ning, V. Rapp, Y. Zeng, Y. Liu, J. S., Y. Tao, Y. Jiang, J. Beak, S. Kaur, H. Lee, X. Zheng and R. S. Prasher, *Nature Communication*, 2010, **10**, 4279–4283.

[48] R. Herino, G. Bomchil, K. Barla, C. Bertrand and J. Ginoux, *J. Electrochem. Soc.*, 1987, **134**, 1994–2000.

[49] H. Foll, M. Christophersen, J. Carstensen and G. Hasse, *Materials Science and Engineering R*, 2002, **39**, 93–141.

[50] X. Zhang, *Journal of The Electrochemical Society*, 2004, **151**, C69–C80.

[51] A. Lehmann and U. Gosele, *Adv. Mater. (Weinheim, Ger.)*, 1992, **4**, 114–116.

[52] X. Zhang and S. C. Bayliss, *Journal of Applied Physics*, 1996, **79**, 1351.

[53] P. Pump, [Accessed: 2023], `https://sg.vwr.com/store/product/17880316/peristaltic-pumps-pp-10-andpp-20`.

[54] K. Goetz, D. Vermeulen, M. Payne, C. Kloc, L. McNeilb and O. Jurchescu, *Journal of Materials Chemistry C*, 2014, **2**, 3065–3076.

[55] H. Shirakawa, E. J. Louis, A. G. MacDiarmid, C. C. K. and A. J. Heeger, *J. Chem. Soc., Chem. Commun.*, 1977, 578–580.

[56] N. Hall, *Chem. Commun.*, 2003, 1–4.

[57] I. Piquero-Zulaica, A. Garcia-Lekue, L. Colazzo, C. K. Krug, M. S. G. Mohammed, Z. M. Abd El-Fattah, J. M. Gottfried, D. G. De Oteyza, J. E. Ortega and J. Lobo-Checa, *ACS Nano*, 2018, **12**, 10537–10544.

[58] H. Masai and J. Terao, *Polymer Journal*, 2017, **49**, 805–814.

[59] T. Blythe and D. Bloor, *Electrical properties of polymers*, Cambridge University Press, 2005.

[60] T. Stott and M. Wolf, *Coordination Chemistry Reviews*, 2003, **246**, 89–101.

[61] B. Muktha, G. Madras, T. N. Guru Row, U. Scherf and S. Patil, *J. Phys. Chem. B*, 2007, **111**, 7994–7998.

[62] M. Zhanga and X. Wang, *Energy Environ. Sci.*, 2014, **7**, 1902–1906.

[63] C. R. McNeill and N. C. Greenham, *Advanced Materials*, 2009, **21**, 3840–3850.

[64] K. Gu and Y.-L. Loo, *Journal of Polymer Science Part B*, 2019, **57**, 1559–1571.

[65] T. Skotheim, J. Reynolds and R. Elsenbame, *Handbook of Conducting Polymers*, Marcel Dekke, 2nd ed., 1998.

[66] V. Guarino, M. L. Focarete and D. Pisignano, *Advances in Nanostructured Materials and Nanopatterning Technologies*, Elsevier, 2020.

[67] T. Kaloni, P. Giesbrecht, G. Schreckenbach and M. Freund, *Chem. Mater.*, 2017, **29**, 10248–10283.

[68] S. Rittmeyer and A. Groß, *Beilstein J. Nanotechnol.*, 2012, **3**, 909–919.

[69] M. Ansari, S. Mohiuddin, F. Kandemirli and M. Malik, *Journal of Chemistry A*, 2018, **8**, 8319.

[70] H. Sirringhaus, P. Brown, R. Friend, M. M. Nielsen, K. Bechgaard, B. M. W. Langeveld-Voss, A. J. H. Spiering, R. A. J. Janssen, E. W. Meijer, P. Herwig and D. M. de Leeuw, *Nature*, 1999, **401**, 686–688.

[71] K. M. Coakley, B. S. Srinivasan, J. M. Ziebarth, C. Goh, Y. Liu and M. D. McGehee, *Advanced Functional Materials*, 2005, **15**, 1927–1932.

[72] S. Hugger, R. Thomann, T. Heinzel and T. Thurn-Albrecht, *Colloid Polym Sci*, 2004, **282**, 932–938.

[73] R. S. Loewe, P. C. Ewbank, J. Liu, L. Zhai and R. D. McCullough, *Macromolecules*, 2001, **34**, 4324–4333.

[74] D. Dudenko, A. Kiersnowski, J. Shu, D. Pisula, W. Sebastiani, H. Spiess and M. Hansen, *Angew. Chem. Int. Ed*, 2012, **51**, 11068 –11072.

[75] M. Roesing, J. Howell and D. Boucher, *Journal of Polymer Science Part B: Polymer Physics*, 2017, **55**, 1075–1087.

[76] J. Martín, A. Nogales and M. Martín-González, *Macromolecules*, 2013, **46**, 1477–1483.

[77] D. Kim, M.-G. Jeong, H. Seo and Y. Kim, *Phys. Chem. Chem. Phys.*, 2015, **17**, 599.

[78] I. E. Jacobs, E. W. Aasen, J. L. Oliveira, T. N. Fonseca, J. D. Roehling, J. Li, G. Zhang, M. P. Augustine, M. Mascal and A. J. Moule, *J. Mater. Chem. C*, 2015, **4**, 3454–3466.

[79] Z. Liang, Y. Zhang, M. Souri, X. Luo, A. M. Boehm, R. Li, Y. Zhang, T. Wang, D.-Y. Kim, D. Mei, S. R. Marderb and K. R. Graham, *Journal of Chemistry A*, 2018, **6**, 16495–16505.

[80] S. Erker and O. Hofmann, *J. Phys. Chem. Lett.*, 2016, **10**, 848–854.

[81] M. Cui, H. Rui, X. Wu, Z. Sun, W. Qu, W. Qin and S. Yin, *J. Phys. Chem. Lett.*, 2021, **12**, 8533–8540.

[82] I. Salzmann, G. Heimel, M. Oehzelt, S. Winkler and N. Koch, *Acc. Chem. Res.*, 2016, **49**, 370-378.

[83] D. Stanfield, Y. Wu, S. Tolbert and B. Schwartz, *Chem. Mater.*, 2021, **33**, 2343–2356.

[84] H. Hase, M. Berteau-Rainville, S. Charoughchi, E. Orgiu and I. Salzmann, *Appl. Phys. Lett.*, 2021, **118**, 203301.

[85] R. Singh, J. Kumar, R. Singh, R. Kant, R. Rastogi, S. Chand and V. Kumar, *New J. Phys.*, 2006, **8**, 112.

[86] J. Lenz and R. Weitz, *APL Materials*, 2021, **9**, 110902.

[87] J. Bombile, M. Janik and S. Milner, *Phys. Chem. Chem. Phys.*, 2018, **20**, 317–331.

[88] K. Väkiparta, M. Reghu, M. Andersson and T. Moulton, J.and Taka, *Solid State Communications*, 1993, **87**, 619–622.

[89] S. Gregory, R. Hanus, A. Atassi, J. Rinehart, J. Wooding, A. Menon, M. Losego, G. Snyder and S. Yee, *Nature Materials*, 2021, **20**, 1414–1421.

[90] C. Hong, Y. Yoo, Y. Kang, J. Ryu, S. Cho and K.-S. Jang, *RSC Adv.*, 2015, **5**, 11385–11391.

[91] K. Väkiparta, M. Reghu, M. Andersson and T. Moulton, J.and Taka, *ACS Appl. Electron. Mater.*, 2021, **3**, 1252–1259.

[92] Q. Zhang, Y. Sun, W. Xu and D. Zhu, *Energy Environ. Sci.*, 2014, **5**, 9639.

[93] E. Lim, K. Peterson, G. Su and M. Chabinyc, *Chem. Mater.*, 2018, **30**, 998–1010.

[94] V. Untilova, T. Biskup, L. Biniek, V. Vijayakumar and M. Brinkmann, *Macromolecules*, 2020, **53**, 2441–2453.

[95] S. Qu, Q. Yao, L. Wang, Z. Chen, K. Xu, H. Zeng, W. Shi, T. Zhang, C. Uher and L. Chen, *NPG Asia Materials*, 2016, **8**, e292.

[96] C. Bounioux, P. Dıaz-Chao, M. Campoy-Quiles, M. Martın-Gonzalez, A. Goni, C. Yerushalmi-Rozen and C. Muller, *Energy Environ. Sci.*, 2013, **6**, 918.

[97] C. Hong, W. Lee, Y. Kang, Y. Yoo, J. Ryu, S. Cho and K.-S. Jang, *J. Mater. Chem. A,*, 2015, **3**, 12314–12319.

[98] C. Hong, Y. Kang, J. Ryu, S. Cho and K.-S. Jang, *J. Mater. Chem. A,*, 2015, **3**, 21428–21433.

[99] J. Choi, J. Lee, S.-S. Lee, C. Park and H. Kim, *Advanced Energy Materials*, 2016, **6**, 1–8.

[100] L. Wang, Z. Zhang, Y. Liu, B. Wang, L. Fang, J. Qiu, K. Zhang and S. Wang, *Nature Communications*, 2018, **9**, 1–8.

[101] M. C. Gélvez-Rueda, M. B. Fridriksson, R. K. Dubey, W. F. Jager, W. van der Stam and F. Grozema, *Nature Communications*, 2020, **11**, 1–9.

[102] M. Sofos, J. Goldberger, D. A. Stone, J. E. Allen, Q. Ma, D. J. Herman, L. J. Tsa2, W-W. Lauhon and S. I. Samuel I. Stupp, *Nature Materials*, 2009, **8**, 68–75.

[103] O. Gang, P. Huber, A. Karim, I. Zvonkina, S.-W. Lee, J.-W. Kim, D. K. Roper and W. J. Li, *Soft Matter and Biomaterials on the Nanoscale*, World Scientific, 2020, vol. 1.

[104] F. Montilla, M. A. Cotarelo and E. Morallon, *Journal of Materials Chemistry*, 2009, **19**, 305–310.

[105] I. B. Martini, I. M. Craig, W. C. Molenkamp, H. Miyata, S. H. Tolbert and B. J. Schwartz, *Nature Nanotechnology*, 2007, **2**, 647–652.

[106] M. Aryal, K. Trivedi and W. Hu, *ACS Nano*, 2009, **3**, 3085–3090.

[107] H. Peng, X. Sun, W. Weng and X. Fang, *Polymer Materials for Energy and Electronic Applications*, Elsevier, 2017.

[108] P. E. De Jongh and T. M. Eggenhuisen, *Advanced Materials*, 2013, **25**, 6672–6690.

[109] G. Heffner and D. Pearson, *Macromolecules*, 1991, **24**, 6295–6299.

[110] L. G. Cencha, G. Dittrich, P. Huber, C. L. A. Berli and R. Urteaga, *Physical Review Letters*, 2020, **125**, 234502.

[111] F. Vazquez Luna, M. Gerstenberger, G. Dittrich, J. Martins de Souza e Silva, P. Huber, R. Wehrspohn and M. Steinhart, *The Journal of Physical Chemistry C*, 2021, **125**, 26731–26743.

[112] K. M. Coakley and M. D. McGeheea, *Applied Physics Letters*, 2003, **83**, 3380–3382.

[113] N. Jaziri, A. Boughamour, J. Müller, F. Mezghani, B. Tounsi and M. Ismail, *Energy Reports*, 2020, **6**, 264–287.

[114] NASA, [Accessed: 2023], `https://voyager.jpl.nasa.gov/mission/spacecraft/instruments/rtg/`.

[115] J. Webster and D. Emin, *Seebeck Effect in Wiley Encyclopedia of Electrical and Electronics Engineering*, Wiley, 1999.

[116] J. Sousa, J. Ventura and A. Pereira, *Transport Phenomena in Micro- and Nanoscale Functional Materials and Devices*, Elsevier, 1st edn, 2021.

[117] C. Goupil, W. Seifert, K. Zabrocki, E. Muller and G. Snyder, *Entropy*, 2011, **13**, 1481–1517.

[118] L. Onsager, *Phys. Rev.*, 1931, **37**, 405.

[119] R. Gross and A. Marx, *Festkörperphysik*, De Gruyter Studium, 2012.

[120] H. Ibach and H. Lüth, *Solid-State Physics*, Wiley, 4th edn, 2009.

[121] C. Jeong, S. Datta and M. Lundstrom, *Journal of Applied Physics*, 2011, **109**, 073718.

[122] C. Jeong, S. Datta and M. Lundstrom, *Journal of Applied Physics*, 2012, **111**, 093708.

[123] M. Thommes, K. Kaneko, A. Neimark, J. Olivier, F. Rodriguez-Reinoso, J. Rouquerol and K. Sing, *Pure and Applied Chemistry*, 2015, **87**, 1051–1069.

[124] S. Brunauer, P. H. Emmett and E. Teller, *Journal of the American Chemical Society*, 1938, **60**, 309–319.

[125] Q. Instruments, 2015, 349–360.

[126] G. Mason, *Proc. R. Soc. Lond. A*, 1983, **390**, 47–72.

[127] M. Hosokawa, K. Nogi, M. Naito and T. Yokoyama, *Nanoparticle Technology Handbook*, Elsevier Science, 2008.

[128] Y. Yortsos, *Methods in the Physics of Porous Media*, Academic Press, 1999.

[129] D. Schroeder, *An Introduction to Thermal Physics*, Oxford University Press, 2021.

[130] K. Galvin, *Chemical Engineering Science*, 2005, **60**, 4659 – 4660.

[131] E. P. Barrett, L. G. Joyner and P. P. Halenda, *Journal of the American Chemical Society*, 1951, **73**, 373–380.

[132] W. Rontgen, *Nature*, 1896, **53**, 274.

[133] CERN, [Accessed: 2023], `https://home.cern/science/accelerators/super-proton-synchrotron`.

[134] DESY, [Accessed: 2023], `https://photon-science.desy.de/facilities/petra_iii/facility_information/index_eng.html`.

[135] J. Als-Nielsen and D. McMorrow, *Elements of Modern X-ray Physics, Second Edition*, Wiley, 2001.

[136] P. Makuła, M. Pacia and W. Macyk, *J. Phys. Chem. Lett.*, 2018, **9**, 6814–6817.

[137] J. Pankove, *Optical Processes in Semiconductors*, Dover Publications, 1971.

[138] J. Tauc, R. Grigorovici and A. Vancu, *Physica Status Solidi b*, 1966, **15**, 627–637.

[139] C.-Y. Tsai., *Journal of Applied Physics*, 2018, **123**, 183103.

[140] L. de Broglie, *On the Theory of Quanta*, Ph.D. Thesis, Paris, 1924.

[141] W. Zhou, R. Apkarian, Z. Wang and D. Joy, *Fundamentals of Scanning Electron Microscopy*, Springer, 2007, vol. 1.

[142] L. Reimer, *Scanning Electron Microscopy*, Springer, 1998.

[143] E. Ruska, *Bioscience Reports*, 1987, **7**, 607–629.

[144] Netzsch, Simultaneous Determination of the Seebeck Coefficient and Electrical Conductivity SBA 458 Nemesis, [Accessed: 2023] `https://analyzing-testing.netzsch.com/pl/produkty/seebeck-analyzer-sba/sba-458-nemesis`.

[145] W. Parker, R. Jenkins, C. Butler and G. Abbott, *Journal of Applied Physics*, 1961, **32**, 1679.

[146] J. Cape and G. Lehman, *Journal of Applied Physics*, 1963, **34**, 1909.

[147] R. Cowan, *Journal of Applied Physics*, 1963, **34**, 926.

[148] Quantum-Design, *Physical Property Measurement System, Thermal Transport Option User's Manual*, 2002.

[149] S. L. Lim, Y. Liu, G. Liu, S. Y. Xu, H. Y. Pan, E.-T. Kang and C. K. Ong, *Physica Status Solidi (a)*, 2011, **208**, 658–663.

[150] J. Fanous, M. Schweizer, D. Schawaller and M. Buchmeiser, *Macromolecular Materials and Engineering*, 2012, **297**, 123–127.

[151] S. Cook, A. Furubea and R. Katoh, *Journal of Materials Chemistry*, 2012, **22**, 4282–4289.

[152] P. Kar, *Doping in Conjugated Polymers*, Wiley, 2013.

[153] P. Kumar, T. Hofmann, K. Knorr and P. Huber, *Journal of Applied Physics*, 2007, **103**, 024303.

[154] Quantum-Design, *Physical Property Measurement System, Heat Capacity Option User's Manual*, 2004.

[155] A. Einstein, *Annalen der Physik*, 1907, **327**, 180–190.

[156] C. Kittel, *Introduction to Solid State Physics*, John Wiley and Sons, 8th edn, 2004.

[157] T. Claudio, G. Schierning, R. Theissmann, H. Wiggers, H. Schober, M. Koza and R. Hermann, *J Mater Sci*, 2013, **48**, 2836–2845.

[158] M. Mertig, G. Pompe and E. Hegenbarth, *J Mater Sci*, 1984, **49**, 369.

[159] M. Michailov and I. Avramov, *Journal of Physics: Conference Series*, 2012, **398**, 012008.

[160] L. Wang, Z. Tan, S. Meng, D. Liang and G. Li, *Journal of Nanoparticle Research*, 2001, **3**, 483–487.

[161] T. Hofmann, D. Kojda, H. Haseeb, D. Wallacher, O. Sobolev and K. Habicht, *Microporous and Mesoporous Materials*, 2021, **312**, 110814/1–7.

[162] T. Zhu and E. Ertekin, *Physical Rewiev B*, 2021, **93**, 155414.

[163] Y. Hu and H. Tanaka, *Nature Physics*, 2022, **18**, 669–677.

[164] P. Benassi, M. Krisch, C. Masciovecchio, V. Mazzacurati, G. Monaco, G. Ruocco, F. Sette and R. Verbeni, *Phys. Rev. Lett.*, 1996, **77**, 3835.

[165] R. Vacher, J. Pelous and E. Courtens, *Phys. Rev. B*, 1997, **56**, R481(R).

[166] M. Baggioli and A. Zaccone, *Phys. Rev. Lett.*, 2019, **122**, 145501.

[167] T. Nakayama, *Rep. Prog. Phys.*, 2002, **65**, 1195–1242.

[168] N. Richet, *Physica B*, 2009, **404**, 3799–3806.

[169] K. Valalaki and A. Nassiopoulou, *Nanoscale Research Letters*, 2014, **9**, 2726–2734.

[170] S. Alexander, O. Entin-Wohlman and R. Orbach, *Phys Rev B*, 1986, **34**, 2726–2734.

[171] W. H. Lee, C. Lee and J. Jang, *Journal of Non-Crystalline Solids*, 1996, **198-200**, 911–914.

[172] H. Barber, *Solid-State Electronics*, 1967, **11**, 1039–1051.

[173] W. Meyer and H. Neldel, *Z. tech. Phys.*, 1937, **12**, 588.

[174] Y. Lubianiker and I. Balberg, *Journal of Non-Crystalline Solids*, 1998, **227-230**, 180–184.

[175] M. Kondo, Y. Chida and A. Matsuda, *Journal of Non-Crystalline Solids*, 1996, **198-200**, 178–181.

[176] Y. Lubianiker and I. Balberg, *Physical Review Letters*, 1997, **78**, 2433.

[177] A. Yelon, B. Movaghar and R. S. Crandall, *Reports on Progress in Physics*, 2006, **69**, 1145–1194.

[178] A. Yelon, B. Movaghar and H. Branz, *Phys. Rev. B*, 2006, **46**, 12244.

[179] D. Emin, *Advances in Physics*, 1975, **24**, 305–348.

[180] N. Mott and E. Davis, *Electronic Processes in Non-Crystalline Materials*, Oxford, 2001.

[181] H. Dyalsingh and J. Kakalios, *Phys. Rev. B*, 1996, **54**, 7630.

[182] M. Cutler and N. Mott, *Phys. Rev.*, 1969, **181**, 1336.

[183] S. Kang and G. Snyder, *Nature Materials*, 2017, **16**, 252–257.

[184] S. Kang and G. Snyder, *Nature Materials*, 2017, **16**, 252–257.

[185] P. Kumar, E. Zaia, E. Yildirim and a. et, *Nat Commun*, 2018, **9**, 5347.

[186] Y. Lee, J. Park, J. Son, H. Woo and J. Kwak, *Adv. Funct. Mater.*, 2021, **31**, 2006900.

[187] J. Bombile, S. Shetty, M. Janik and S. Milner, *Phys. Chem. Chem. Phys.*, 2020, **22**, 4032–4042.

[188] A. Salleo, T. W. Chen and A. R. Volkel, *Phys. Rev. B.*, 2004, **70**, 115–311.

[189] K. Valalaki, P. Benech and A. Nassiopoulou, *Journal of Applied Physics*, 2016, **11**, 201.

[190] Q. Zhang, Y. Sun, W. Xu and D. Zhu, *Macromolecules*, 2014, **477**, 609–615.

[191] X. Li, Z. Zhu, T. Wang, J. Xu, C. Liu, Q. Jiang, F. Jiang and P. Liu, *Composites Communications*, 2019, **12**, 128–132.

[192] S. Qu, M. Wang, Y. Chen, Q. Yao and L. Chen, *RSC Adv.*, 2018, **8**, 33855–33863.

[193] M. He, J. Ge, Z. Lin, X. Feng, X. Wang, H. Lu, Y. Yanga and F. Qiu, *Energy Environ. Sci.*, 2012, **5**, 8351.

[194] R. Noriega and a. et, *Nat. Mater.*, 2013, **12**, 1038–1044.

[195] A. Parnell, A. Cadby, O. Mykhaylyk, A. Dunbar, P. Hopkinson, A. Donald and R. Jones, *Macromolecules*, 2011, **44**, 6503–6508.

[196] G. Gesele, J. Linsmeier, V. Drach, J. Fricke and R. Arens-Fischer, *J. Phys. D: Appl. Phys.*, 1991, **30**, 2911.

[197] L. Weber and E. Gmelin, *Applied Physics A*, 1991, **53**, 136–140.

[198] K. Regner, D. Sellan, Z. Su and et al., *Nature Communication*, 2013, **4**, 1640.

[199] D. G. Cahill, H. E. Fisher, T. Klitsner and E. Swartz, *J. Vac. Sci. Technol. A*, 1989, **7**, 1259.

[200] J. C., S. Datta and M. Lundstrom, *Journal of Applied Physics*, 2012, **111**, 093708.

[201] D. Kojda, T. Hofmann, N. Gostkowska-Lekner and K. Habicht, *Nano Research*, 2022, **15**, 5663–5670.

[202] M. Holland, *Phys. Rev.*, 1963, **132**, 2461–2471.

[203] J. de Boor, D. S. Kim, X. Ao, D. Hagen, A. Cojocaru, H. Föll and V. Schmidt, *Europhys. Lett.*, 2011, **96**, 16001.

[204] J. Maxwell, *A treatise on electricity and magnetism*, Oxford University Press, 1904.

[205] J. Strutt, *Phil. Mag.*, 1892, **34**, 481.

[206] R. Bird, W. Stewart and E. Lightfoot, *Transport phenomena*, John Wiley and Sons, 2007.

[207] K. Pietrzak and T. Wiśniewski, *Journal of Power Technologies*, 2015, **95**, 14–24.

[208] C.-W. Nan, *Progress in Materials Science*, 1993, **37**, 1–116.

[209] D. Bruggeman, *Ann. Phys.*, 1935, **24**, 636.

[210] R. Landauer, *J. Appl. Phys.*, 1952, **23**, 779.

[211] S. Kirkpatrick, *Rev. Mod. Phys.*, 1973, **45**, 574.

[212] N. B. Vargaftik, *Handbook of Thermal Conductivity of Liquids and Gases.*, CRC Press, 1993.

[213] K. Herrmann, S. Freund, F. Eller, T. Rößler, G. Papastavrou, E. Herzig and M. Retsch, *Materials*, 2022, **15**, 7700.

[214] Y. Xu, X. Wang, J. Zhou, B. Song, Z. Jiang, E. M. Y. Lee, S. Huberman, K. K. Gleason and G. Chen, *Science Advances*, 2018, **3**, eaar3031.

[215] M. Rojo, J. Martın, S. Grauby, T. Borca-Tasciuc, S. Dilhaire and M. Martin-Gonzalez, *Nanoscale*, 2014, **6**, 7858.

[216] M. K. Smith, T. L. Bougher, K. Kalaitzidou and B. A. Cola, *MRS Advances*, 2017, **2**, 3619–3626.

# List of Tables

# List of Figures

# Acknowledgments

I would like to express my very great appreciation to PD Dr. Klaus Habicht for supervising this work. Thank you for the interesting discussions and suggestions, which have contributed greatly to the success of this work. I'm extremely grateful that together with Dr. Tommy Hofmann, you gave me a life changing opportunity to work as a doctoral researcher at Helmholtz-Zentrum Berlin.
I would like to express my deepest appreciation to my mentor Dr. Tommy Hofmann for his invaluable patience and feedback. Your excellent support, concepts, supervision and support in interpreting the measurement data and results has been very much appreciated. Thank you for involving me in the exciting research opportunities and introducing me to the world of large-scale facilities.
Additionally, this endeavor would not have been possible without the generous support from the Deutsche Forschungsgemeinschaft, who funded the project "Hybrid Thermoelectric Materials Based on Porous Silicon: Linking Macroscopic Transport Phenomena to Microscopic Structure and Elementary Excitations" under the number 402553194.
I would like to offer my special thanks to Dr. Dirk Wallacher for allowing me to work in his etching lab and creating an extra safe environment for working with HF. Your help and expertise has been invaluable.
My grateful thanks are also extended to Dr. Danny Kojda for his help with the measurements and thermal transport modeling, and to Jan Hoffmann for his irreplaceable technical assistance and SEM sessions.
I am also thankful for everybody in my group Dynamics and Transport in Quantum Materials at Helmholtz-Zentrum Berlin for their expertise, experimental help and moral support.
Lastly, I would like to mention my family, especially my parents, sisters, and grandparents. Their belief in me has kept my spirits and motivation high during this process. The final thanks goes to my dearest husband. You are always at my side with the greatest support and programming advice. This would not have been possible without you.